Materials Advances

ROYAL SOCIETY OF CHEMISTRY

REVIEW

View Article Online
View Journal | View Issue

Cite this: *Mater. Adv.*, 2024, 5, 920

Recent advances in hydrothermally and solvothermally grown Co_3O_4 nanostructures for electrochemical energy storage (EES) applications: a brief review

Radhika S. Desai, [a] Vinayak S Jadhav, [a] Pramod S. Patil *[b] and Dhanaji S. Dalavi *[a]

The increasingly intimate connection between energy generation, energy storage difficulties, and the growing human energy demands necessitates the invention and development of energy storage electrodes/devices. In recent years, spinal structured Co_3O_4, coupled with several fascinating features such as high redox activity, different oxidation states, and high theoretical capacitance, has found widespread use as a promising material for electrochemical energy storage (EES) applications. This review outlines the progress of pristine Co_3O_4 electrodes under high-pressure conditions (hydrothermal and solvothermal) over the last three decades for EES applications. Nowadays, developing hybrid nanostructures, doping, and tailoring nanostructure morphology are the most widely used strategies to fabricate highly efficient EES devices. However, so far pristine Co_3O_4 as an active electrode material with different dimensionalities for EES applications has been prepared using several strategies (such as using surfactants, templates, and various agents or changing the reaction conditions), *via* hydrothermal/solvothermal techniques, and specific strategies have been substantiated to be highly effective in enhancing its overall performance. Hence, it is essential to analyze it systematically to be beneficial for future studies. Furthermore, this review provides an overview of symmetric and asymmetric energy storage devices based on synthesized Co_3O_4 electrodes. This report provides statistical data on EES performance metrics of pristine Co_3O_4 electrodes and Co_3O_4-based devices, as stated in the published literature. The present study provides the key perspectives on next-generation Co_3O_4-based EES research.

Received 4th October 2023,
Accepted 19th December 2023

DOI: 10.1039/d3ma00806a

rsc.li/materials-advances

[a] *Department of Physics, Krishna Mahavidyalaya, Rethare Bk, Karad, Maharashtra, India. E-mail: dhanuphysics@gmail.com*
[b] *Department of Physics, Shivaji University, Kolhapur, India. E-mail: psp_phy@unishivaji.ac.in*

Radhika S. Desai

Mrs. Radhika S. Desai is currently working as an Assistant Professor, at Krishna Mahavidyalaya, Rethare BK, MS, India. She received her MSc degree from Shivaji University, Kolhapur, in 2005. Now, she is pursuing a PhD under the supervision of Dr Dhanaji S. Dalavi. Her research interests include nanostructured smart materials for energy storage and electrochromic applications.

Vinayak S Jadhav

Mr. Vinayak S. Jadhav is currently pursuing a PhD under the supervision of Prof. (Dr) Pramod S. Patil, MS, India. He received his MSc degree from Dr Babasaheb Ambedkar Marathwada University, Aurangabad, in 2014. His current research interests include nanostructured materials for energy storage and electrochromic applications.

1. Introduction

In recent years, fulfilling the growing energy demands and reducing the environmental degradation caused by non-conventional energy sources have become important issues. Energy harvesting using renewable energy sources, their proper conversion, and the development of related advanced storage techniques have become major research areas and are being widely studied. In particular, batteries, capacitors, electrochemical capacitors (ECs) and supercapacitors (SCs) are the most widely used energy storage systems. The Ragone plot in Fig. 1(a) depicts the power density *vs.* energy density of the above energy storage systems. It shows that capacitors have high specific power (ability to supply stored charge) in the order of 10^5 W kg^{-1}, while batteries have high specific energy (ability to store charge) in the order of 10^2 W h kg^{-1}. But the specific energy of SCs (10–100 W h kg^{-1}) is greater than that of capacitors ($<10^{-1}$ W h kg^{-1}).[1,2] SCs with high specific power (10^4 W kg^{-1}) are superior to a battery as they can store and supply energy at relatively high rates. So to some extent, SCs can bridge the gap between these two well-known energy storage systems.[3] Various attributes such as long cycling stability (10^5 cycles), fast charge–discharge rate, and easy fabrication with the low maintenance of supercapacitors enable them as an efficient alternative solution to providing high power in areas where the current battery technology has failed. As SCs fail to store large energy, this failure can be effectively faded by increasing the specific capacitance and operating voltage.[4]

Improving the specific energy of supercapacitors without compromising their specific power is one of the most critical challenges. Xie *et al.* suggested some striking strategies from their study to accomplish this goal: firstly, to explore distinctive materials that undergo fast surface electrochemical reactions without phase transformation. Secondly, developing networked, hierarchically porous electrodes with low diffusion and ohmic polarization, or an electrode containing stacked thin energy storage layer and a conductive layer can also significantly overcome the diffusion limit and help to utilize the entire porous electrode efficiently. Furthermore, the cell voltage of a supercapacitor depends on the electrolyte stability voltage window. Studies have shown that the operating voltage of active electrode materials increases after using organic electrolytes instead of aqueous electrolytes.[5]

Therefore, it would be very beneficial to use ionic liquids with a wide potential window (up to 4 V) and to explore new hybrid materials combining double-layer capacitance as well as pseudo-capacitance mechanisms.[6] In contrast, the high specific energy of lithium-ion batteries makes them more capable of gratifying the power supply needs of various devices such as laptops, cell phones, and next-generation electric and hybrid electric vehicles. However, the major drawback of a battery is that its efficiency decreases at high charge–discharge rates. With this goal, many research efforts are being made to synthesize more reliable as well as efficient energy storage devices.[7]

Transition metal oxides (TMOs) and hydroxides, conducting polymers (CPs), and carbonaceous materials are widely utilized as functional materials for EES applications. Transition metal oxides (TMOs) and hydroxides can be easily synthesized through a variety of low-cost and straightforward methods. These approaches provide a means to precisely control their electrical conductivity and surface morphologies.[8] They are considered to have relatively high capacitance due to their various redox reactions during rapid charging–discharging with

Pramod S. Patil

Prof. Pramod S. Patil is currently working as the Pro-Vice Chancellor of Shivaji University, Kolhapur, MS, India. He is the former Dean of Science and Technology. He has served as the former founder and Director of the School of Nanoscience and Technology, Former Head of the Physics Department, and Coordinator of the Department of Energy Technology. Prof Patil is a recipient of the DAAD fellowship, Germany, and the Brain Pool fellowship, South Korea. He has established the Center of Nanofabrics. After having received his PhD degree from Shivaji University in 1990, Prof. Patil has been zealously engaged in research on solar cells, electrochromic smart window materials, supercapacitors, sensors, and nanotechnology. He has more than 450 research articles, 5 patents and several book chapters to his credit and has received more than 22500 citations with an h index of 75.

Dhanaji S. Dalavi

Dr Dhanaji S Dalavi is currently working as an Assistant Professor at Krishna Mahavidyalaya, Rethare BK, MS, India. He is the Head of the Department of Physics. He received his MSc degree in Physics and PhD degree in "Electrochromic Smart Window" from Shivaji University, Kolhapur, in 2008 and 2013 respectively. He is a recipient of the prestigious Dr D. S. Kothari Post-Doctoral Fellowship, UGC, India. His research interest includes nanostructured materials for electrochromic smart windows, gas sensors, and electrochemical supercapacitors. He has published 36 research papers in a well reputed international journal and 1 book and has received more than 1750 citations with an h-index of 23.

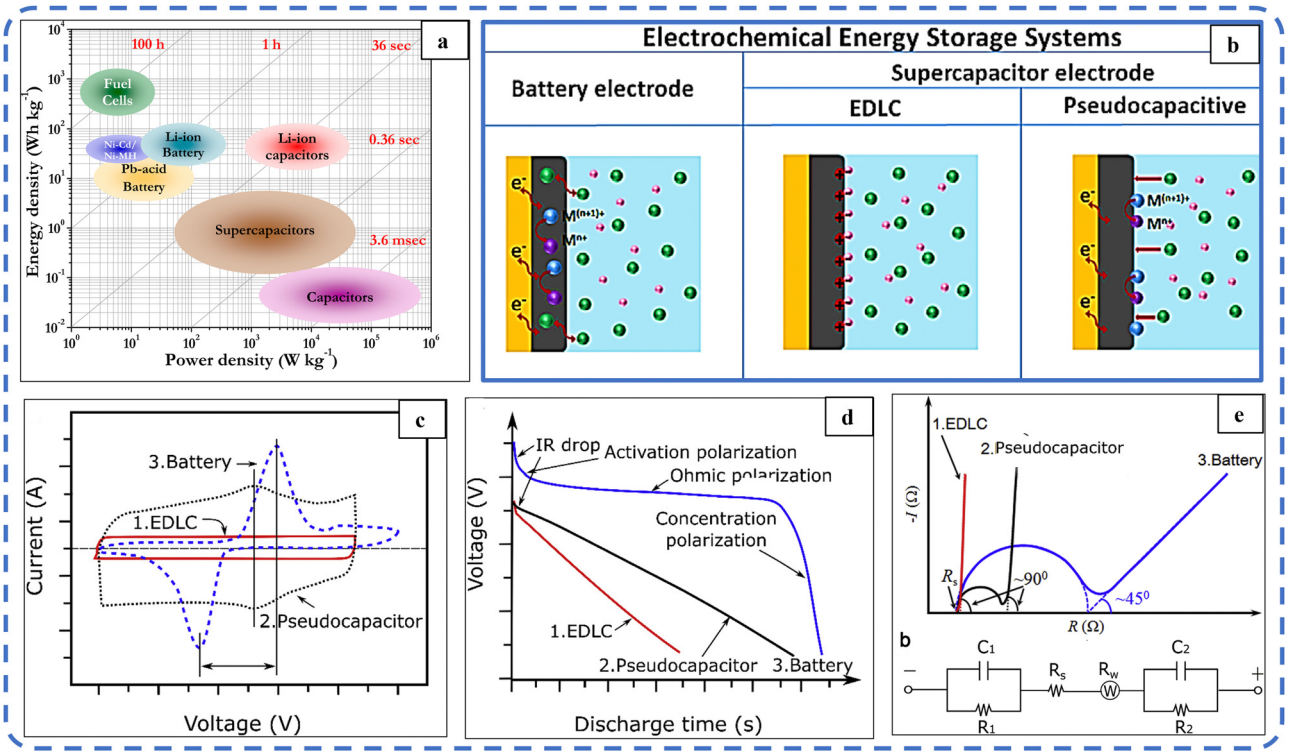

Fig. 1 (a) Ragone plot. Reproduced with permission from ref. 2. Copyright 2014 ACS publications. (b) Schematic diagram of charge storage mechanisms in batteries and supercapacitor electrode materials. Reproduced with permission from ref. 22. Copyright 2019 Wiley Online Library. (c) Typical CV, (d) typical galvanostatic discharge plots and (e) typical Nyquist plots of an ideal EDLC (red, curve 1), pseudocapacitor (black, curve 2), and battery (blue, curve 3). Reproduced with permission from ref. 5. Copyright 2018 Elsevier.

multi-oxidation states. With further benefits such as safe processing and handling capabilities and environmental friendliness, low-cost TMOs serve as superior electrode materials for energy storage applications and are being studied extensively.[9] But they suffer from mechanical instability and structural degradation which results in low rate capability and deteriorates the performance of the synthesized electrode.[10] To address this challenge, multiple strategies have been proposed. These include the synthesis of composite electrodes, doping techniques, and the creation of diverse nanostructured electrodes. These approaches aim to enhance the performance and capabilities of electrodes in electrochemical applications The selection and production of highly efficient electrodes is an important task in the development of practical purpose energy storage applications. Among the emerging active electrode materials, certain transition metal oxides (TMOs) like iridium oxide (IrO_2), rhodium oxide (RhO_2), and ruthenium oxide (RuO_2) stand out for their exceptional capacitance. This is attributed to their ability to undergo rapid and reversible redox reactions on the electrode's surface Despite their high specific energy and capacitance, their high cost has greatly hindered their commercial use. This failure has prompted the development of alternative materials such as NiO, Co_3O_4, MnO_2, V_2O_5, and so on.[11]

Before choosing a specific material for a given application, it is important to consider the overall system essentials, such as safety, cost, and environmental impact. Low-cost Co_3O_4 possesses several properties that make it appropriate for utilization in energy storage applications. Some of its key characteristics are outlined below:

Theoretical specific capacitance

Co_3O_4 has a high theoretical specific capacitance of 3560 F g^{-1}. This remarkable property positions it as a compelling choice for energy storage applications.

Great redox activity

Co_3O_4 is capable of multiple redox reactions involving the conversion between Co(II) and Co(III) states, which is advantageous for high-capacity and high-energy-density applications.[12]

Good rate capability

Co_3O_4 exhibits high charge/discharge rates, making it suitable for applications that require rapid energy transfer.

Promising anode material in lithium-ion batteries

Due to its excellent capacity retention and compatibility with lithium-ion systems, Co_3O_4 has gained considerable attention as an anode material in lithium-ion batteries.[13]

The cycling performance of Co_3O_4-based electrodes can be improved by mitigating volume changes during cycling through various strategies such as synthesizing the nanostructures and their composites.[14]

Thermal and corrosion stability

Co_3O_4 demonstrates thermal stability, enabling it to withstand high operating temperatures without experiencing substantial decomposition or phase alterations.[15,16]

Along with this, the natural abundance, environmental benignity, and ultra-high capacity of Co_3O_4 electrodes have attracted considerable attention in the current development of lithium-ion batteries and supercapacitor applications.

So far, several research groups have reviewed the investigation of Co_3O_4 materials for various applications. In particular, the report presented by Mei *et al.*[17] and Lee *et al.*[18] related to nanostructured cobalt-based compounds for electrochemical capacitor application is remarkable. Then, Hamdani *et al.* have outlined the study of the electrochemical and electrocatalytic properties of spinal cobaltite oxides for oxygen evolutionary reaction (OER) or oxygen reduction reaction (ORR).[19] Recently, Hu *et al.*[20] and Wang *et al.*[21] provided a very comprehensive overview of Co_3O_4 and Co_3O_4-based composite nanomaterials for high-performance supercapacitor applications. However, this review systematically summarizes the tremendous progress in the hydrothermal and solvothermal growth of Co_3O_4 for EES applications. It also provides a brief and relevant description of the various strategies adopted to develop more efficient electrodes with miscellaneous hierarchical porous architectures. It also focuses on a concise overview of the existing literature related to symmetric/asymmetric supercapacitor devices based on the Co_3O_4 electrode material and its performance, along with published statistical data.

This review article is organized into two main parts. Initially, this review provides introductory details about the crystal chemistry of Co_3O_4, its various applications, essential information on hydrothermal and solvothermal techniques, and the research progress timeline of Co_3O_4. Then, the first part summarizes the studies on hydrothermal and solvothermal growth of Co_3O_4 for supercapacitor application and the second part outlines the studies on its battery application.

Charge storage mechanism

Based on the charge storage mechanism, ECs are divided into two basic categories: electrochemical double layer capacitors (EDLCs) and pseudocapacitors (PSUs). The combination of these two storage systems, either as a composite electrode or as two different electrodes in a single device, results in a characteristic hybrid system through their synergistic effect.

EDLCs store energy through a surface-controlled ion absorption process, while PSUs undergo surface-controlled (capacitor-like) and faradaic reactions confined to the surface (or near the surface). This storage system leads to a high specific power, which fosters rapid charging/discharging within minutes. In contrast, Li-ion batteries store charge through diffusion-controlled (faradaic) reactions. These diffusion-controlled (battery-like) redox processes are usually very slow. Hence batteries suffer from low power density (charging/discharging time ranges from minutes to hours). The schematic illustration shown in Fig. 1(b) systematically illustrates that the charge storage mechanisms in EDLC, pseudocapacitive and Li-ion battery materials are different from each other.[22]

The EC and battery performance of the active electrodes is evaluated by electrochemical techniques including cyclic voltammetry (CV), galvanostatic charge–discharge (GCD), and electrochemical impedance spectroscopy (EIS). Typical CV, GCD, and EIS profiles of EDLC, PSU, and battery materials are depicted in Fig. 1(c–e).[5] These three techniques assist in deconvoluting the kinetic responses and identifying the charge-storage mechanism in the active electrode material.[23]

In this, electrode kinetics can be easily determined with the power law dependence of current response (i) on the scan rate (v) given by the following relationship:

$$i = av^b \quad (1)$$

Here, a is a constant. The parameter "b" with a value of 0.5 signifies a diffusion-controlled process, where the current response correlates proportionally with the square root of the scan rate. On the other hand, when "b" equals 1, it indicates a surface-controlled process, where the current response demonstrates a linear proportionality to the scan rate ($i \propto v$). The "b" value between 0.5 and 1 indicates a hybrid energy storage system with a transition from battery-like to capacitive-like behavior.[24,25] NiO and Co_3O_4 and their hydroxides sometimes exhibit battery-like behavior; in such situations the true performance metric of the as-synthesized electrode is its capacity (in C g^{-1}) rather than capacitance (F g^{-1}). Such computations will be crucial while assembling a full device using a capacitive negative electrode.[26]

Crystal chemistry of cobalt oxide

Cobalt has four well-known polymorphs: cobaltous monoxide or cobaltous oxide (CoO), cobaltic oxide (Co_2O_3), cobalt(IV) oxide (CoO_2), and cobaltosic oxide or cobalt cobaltite (Co_3O_4).[17] Cobaltous oxide, cobaltous monoxide or cobalt(II) oxide is the stable oxide of cobalt, obtained after calcination at 1000 °C, and is grey. In the allotropic form, it exists as a yellow-green powder. It is an anodic coloring material widely used as a counter electrode in electrochromic devices.[27]

Mössbauer, X-ray, and chemical techniques have confirmed the existence of two distinct structural forms of CoO, namely, CoO(I) and CoO(II), with densities of 6.4 g cm^{-3} and 3 g cm^{-3}, respectively. Further, Ok and Mullen reported that above 573 K CoO(II) transforms into stable CoO(I).[28] The heating of CoO in the presence of air between 385 and 910 °C converts it to Co_3O_4.[29] Co_2O_3 has been identified as a versatile material with notable properties, including a superparamagnetic nature suitable for applications in microwaves and biomedicine.[30] Additionally, it serves as a catalyst for ring-opening polymerization[31] and demonstrates effectiveness as an active electrode material for supercapacitors.[32] These diverse characteristics make Co_2O_3 a promising candidate for various technological applications.

The normal spinel structure $A[B_2]O_4$ of Co_3O_4 was first reported by Cossee in 1956.[33] The ordinary black-colored Co_3O_4[29] with a lattice parameter of 8.09 Å[34] is the most stable

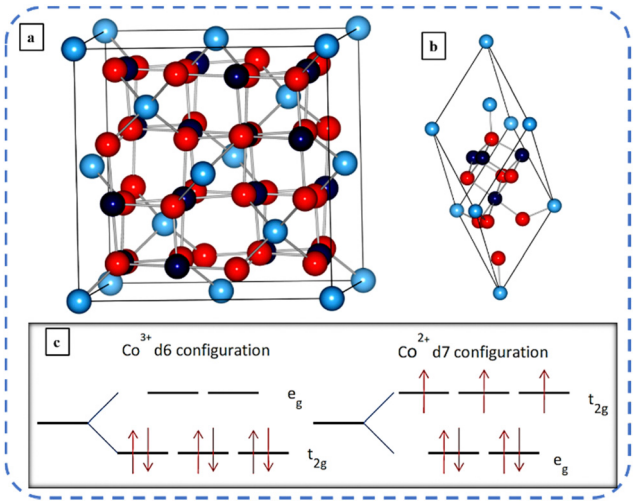

Fig. 2 Schematic representation of a (a) unit cell and (b) primitive cell of Co_3O_4 (with light and navy-blue balls representing Co^{2+} and Co^{3+} ions respectively and red balls O^{2-} ions). (c) Crystal field splitting of Co^{3+} ions and Co^{2+} ions. Reproduced with permission from ref. 36. Copyright 2011, American Physical Society.

mixed $[Co^{II}Co^{III}{}_2O_4]$ valence compound in the Co–O system.[27,35] The cubic normal spinel structured Co_3O_4 has two oxidation states: Co^{2+} and Co^{3+}. They occupy interstitial tetrahedral and octahedral sites, respectively, of closed-packed FCC lattices formed by the oxygen ions. Fig. 2(a and b) depicts the schematic illustration of the unit and primitive cell of cubic Co_3O_4 (space symmetry group *Fd*3*m*) respectively. The unit cell of Co_3O_4 contains 32 oxygen and 24 cobalt atoms. Out of 24 cobalt atoms, 16 cobalt atoms (navy-blue balls representing Co^{3+}) are surrounded by six octahedral oxygen (red balls representing O^{2-} ions), and the remaining 8 cobalt atoms (light-blue balls representing Co^{2+}) are surrounded by four tetrahedrally distributed oxygen ions.[34] Here, in Fig. 2(c), these two oxidation sites split five degenerate (having the same energy) atomic d orbitals into two groups, thus resulting in 3 unpaired d electrons on Co^{2+}, and all the d electrons of Co^{3+} are paired. d_{xy}, d_{xz}, and d_{yz} orbitals (non-axial d-orbitals, *i.e.* lie in between the axes) are called t_{2g} (triply degenerate) orbitals, whereas the d_{z^2} and $d_{x^2-y^2}$ (axial d-orbitals, *i.e.* lie along the axis) orbitals are called e_g (doubly degenerate) orbitals.[36] The octahedral Co^{3+} ion has fully occupied t_{2g} states while the overlying e_g-states are almost empty and for the tetrahedral Co^{2+} ion all e_g-states and the majority of t_{2g}-states are filled, but the minority of the overlying t_{2g}-states are partially filled. This elucidates the non-magnetic and large magnetic moment of Co^{3+} (zero permanent moments) and Co^{2+} ions (moment of $3.26\mu_B$) respectively.[37,38] Co_3O_4 undergoes an antiferromagnetic transition at a Néel temperature of about 40 K.[39,40] Co_3O_4 is a p-type semiconductor with electrical conductivity in the range of 10^{-4} to 10^{-2} S cm^{-1};[41] its theoretical lithium-loading capacity is about 890 mA h g^{-1},[42] and its direct and indirect) band gaps are 2.10 eV and 1.6 eV, respectively.[16,36] α and β are the two crystalline polymorphs of cobalt hydroxides. The positively charged $Co(OH)_{2-x}$ layers and charge balancing ions (NO_3^-, Cl^-, *etc.*) between these layers produce the lamellar network of isostructural α-hydroxides (α-$Co(OH)_2$). The stoichiometric β-$Co(OH)_2$ crystals comprise hexagonally packed hydroxyl ions with Co(II) occupying the alternate rows of octahedral sites, without any anion. Blue-green colored α-$Co(OH)_2$ having greater interlayer spacing (>7 Å) exhibits superior electrochemical activity compared to pink-colored β-$Co(OH)_2$ with an interlayer spacing of 4.6 Å.[43,44] Huang *et al.* systematically investigated the transformation of cobalt hydroxides (α-$Co(OH)_2$ and β-$Co(OH)_2$) into cobalt oxides (Co_3O_4, CoOOH) at low temperatures by varying OH^- : Co^{2+} ratios. It was confirmed that, when this ratio lies between 1 : 1 and 1.8 : 1, the initially formed α-$Co(OH)_2$ phase tends to oxidize into Co_3O_4. For the ratios in the range of 2 : 1 to 50 : 1 the resulting β-$Co(OH)_2$ phase oxidizes into CoOOH.[45] As the oxidation power of hydroperoxide increases with higher temperature, a well-crystallized single phase of spinel structure Co_3O_4 was noticed to be formed only above 180 °C.[46]

Synthesis routes

To date, cobalt oxide-based films have been developed by different synthesis routes such as sol–gel,[47] pulsed laser deposition (PLD),[47] electrodeposition,[48] spray pyrolysis,[16] magnetron sputtering,[49] hydrothermal method,[46] chemical vapor deposition,[50] *etc.* High-pressure conditions provide an important tool to develop new materials through volume contraction, stabilizing thermally unstable materials and improving the reactivity of reactants. These techniques help to increase the knowledge of the correlation between composition, structure, chemical bonding, and resulting physicochemical properties of materials.[51] Hydrothermal and solvothermal methods involve thin film synthesis at high pressures (about 1 atm to several kilobars) and high temperatures (about 100–10 000 °C).[52] Hydrothermal synthesis involves chemical reactions in an aqueous solution (water as solvent) above the boiling point of water. In certain scenarios, water serves multiple roles—it acts as a catalyst, participates as a solid phase component, and, under specific conditions, contributes to altering the physical and chemical properties of reactants and products. Solvothermal synthesis involves chemical reactions occurring in solutions other than water at relatively high temperatures. In this case, a non-aqueous or organic solvent as a reaction medium dissolves the reactants (which affects the chemical reaction rate) and affects the concentration of active species of the reactants. Various alcohols, glycerol, ethylene glycol, ammonia, methanol, *etc.* are the commonly used solvents in solvothermal synthesis. The critical temperature and pressure of some solvents are comparatively lower than that of water (for more details on critical data, refer to ref. 53). An appropriate choice of solvent is based on its density, melting point, boiling point, solvent polarity (a key parameter as it describes the interaction between solvent and solute), *etc.*[54,55]

Hydrothermal/solvothermal techniques are extremely effective approaches for crystal growth and the development of almost all inorganic crystals. Significantly, the starting material used in these methods should be homogeneous, pure, and as fine as possible. These methods offer many advantages,

including the control of particle size (by preparation temperature) and particle shape (by starting material). These approaches assist in the synthesis of low-temperature forms such as α-quartz and α-berlinite, metastable states, high vapor pressure materials, organic/inorganic composites, *etc*.[52]

In 1903, Malzac patented the process for the leaching of sulfides of cobalt and recommended the use of high temperature conditions for the synthesis.[56] In 1917, Morey and Fenner for the first time reported the systematic study of the hydrothermal method with their publication of the synthesis of a ternary system based on H_2O–K_2SiO_3–SiO_2.[57] Preparation of cobalt(II, III) oxide *via* the thermal decomposition of various cobaltous salts ($Co(OAc)_2$, CoC_2O_4, $CoSO_4$, $Co(NO_3)_2$, *etc.*) in air at very high temperatures in the range of 250–900 °C has been reported till 1978. Subsequently, in 1978, Sugimoto *et al*. prepared monodispersed cubic crystals of Co_3O_4 at 100 °C in an autoclave (also called 'bombs') in the presence of acetate ions and an oxidizing agent (O_2). This was the first attempt to grow Co_3O_4, at low temperatures, with a well-defined shape and uniform size.[58] Until 1993, cobalt had not been much studied, possibly due to its complex structure and more than two oxidation states. Initially, Simpraga examined the cyclic voltammetry of cobalt in alkaline solutions at several potential ranges at 298 K and confirmed the reversible redox behavior of cobalt oxide in a NaOH electrolyte with two anodic and two corresponding cathodic peaks.[59] Table 1 summarizes the timeline of the research progress of Co_3O_4.

Applications of Co_3O_4

In 1960, cobalt oxide was studied for the first time as a catalyst for the total oxidation of hydrocarbons and carbon monoxide.[60] It was then studied for various applications, such as an active material in electrochromic devices (as it switches from intense brown in the oxidized state (colored state) to green in the reduced state (bleached state)),[27,61] solid-state gas sensors,[62] active and stable heterogeneous catalysts,[63] magnetoresistive devices,[64] as a negative electrode in rechargeable lithium batteries,[42] in water splitting,[65–67]as a sensor for determination of nitrite in wastewater,[68,69] acetaminophen detection in biological samples and commercial pharmaceutical preparations,[70] electrode material for the vanadium flow battery (VFB),[71] photoelectrochemical applications (PEC),[72] in the development of latent fingerprints,[73] to detect hydrogen peroxide in the nanomolar concentration range,[74] environmental remediation applications, such as the degradation of dyes, dye waste, and antibiotics, sodium-ion hybrid capacitors (SICs),[75] in diverse catalytic and biomedical applications due to its unique antimicrobial, anticancer, catalytic, antioxidant, antifungal, and enzyme inhibition properties,[76,77] an electrochemical sensor for simultaneous and selective determination of hydroquinone (HQ) and catechol (CT),[78] field effect transistors,[79] solar cells,[80] as a photocatalyst,[81] for anticancer treatment applications[82] and so on. Applications of Co_3O_4 in various fields are listed in Fig. 3.

The direct optical band gaps of Co_3O_4 NPs (about 1.48 and 2.19 eV) make them suitable as a photocatalyst for the degradation of organic pollutants using visible light.[76] Recently, Co_3O_4 and graphitic carbon nitride (g-C_3N_4) constructed by the tris-triazine unit have been used in the development of p–n junction all-solid-state supercapacitors based on the photoirradiation-enhanced capacity (PIEC) principle. Photoirradiation-mediation is one of the promising strategies to promote energy conversion and storage applications. Here the capacity of the as-synthesized device was observed to increase by 70.6% at the maximum current density of 26.6 mA cm^{-2} with the help of solar light irradiation.[83] Spinel-structured Co_3O_4 (p-type semiconductor) with a band gap of 1.8 eV has photo-sensitive and pseudocapacitive properties, and thus is suitable for photo-assisted supercapacitor applications. But its light response efficiency is not good, which can be increased by combining it with N-type semiconductors (such as TiO_2) to improve the utilization of solar power in the energy storage process.[84]

Performance metrics related to EES systems

The performance of an electrode material developed for the EES application is estimated based on several performance metrics including capacity, capacitance, specific energy, specific power, *c*-rate, and cycle stability. Capacitance is the ability to store energy in the form of electric charge, calculated by taking the ratio of the amount of electric charge stored and the difference in the electric potential. The amount of electrical charge that can be extracted from a battery at a specific voltage is called the battery capacity.

$$\text{Capacity} = \int I(v)\mathrm{d}t\,(\text{in Ah}) \tag{2}$$

I (in A) refers to discharge current and t (in s) refers to discharge time. The specific capacitance (C_s) and specific

Table 1 The development timeline of Co_3O_4

1956	Normal spinel structure $A[B_2]O_4$ of Co_3O_4 reported by Cossee.
1978	Synthesized monodispersed Co_3O_4 cubic crstals at 100 °C in an autoclave (also called a 'bomb') and this was the first attempt to grow Co_3O_4 at low temperatures with a well-defined shape and uniform size
1993	In NaoH solution, after cycling a transition from absolute irreversibility to relatively reversible redox behaviour of Co_3O_4 was observed
1997	Cobalt oxide was synthesized by the electrochemical precipitation method and the capacitance of a device assembled from two cobalt oxide electrodes was reported to be approximately 10 F g^{-1}
1999	Reported largely reversible redox and pseudocapacitance behaviour of Co_3O_4 in aqueous NaOH and an average pseudo capacitance of about 49.6 mF cm^{-1} (apparent)
1999	Hydrothermally predicted Co_3O_4 fine particles were used as precursors to synthesize $LiCoO_2$ particles
2000	The anodic properties of Co_3O_4 as a lithium storage material with its excellent electrochemical properties were first reported by Pozot *et al.* in 2000, and another study reported its reverse capacity of 900 mA h g^{-1}
2002	The electrochemical behaviour of Co_3O_4 as a positive and negative (superior) electrode was studied
2002	Monodispersive nanocrystalline Co_3O_4 eloctrode (with 3–4 nm particle size) was synthesized *via* a gel hydrothermal oxidation route
2004	Co_3O_4 hollow nanospheres as an anode for use in Li-ion cells were synthesized by a surfactant-assisted solvothermal method

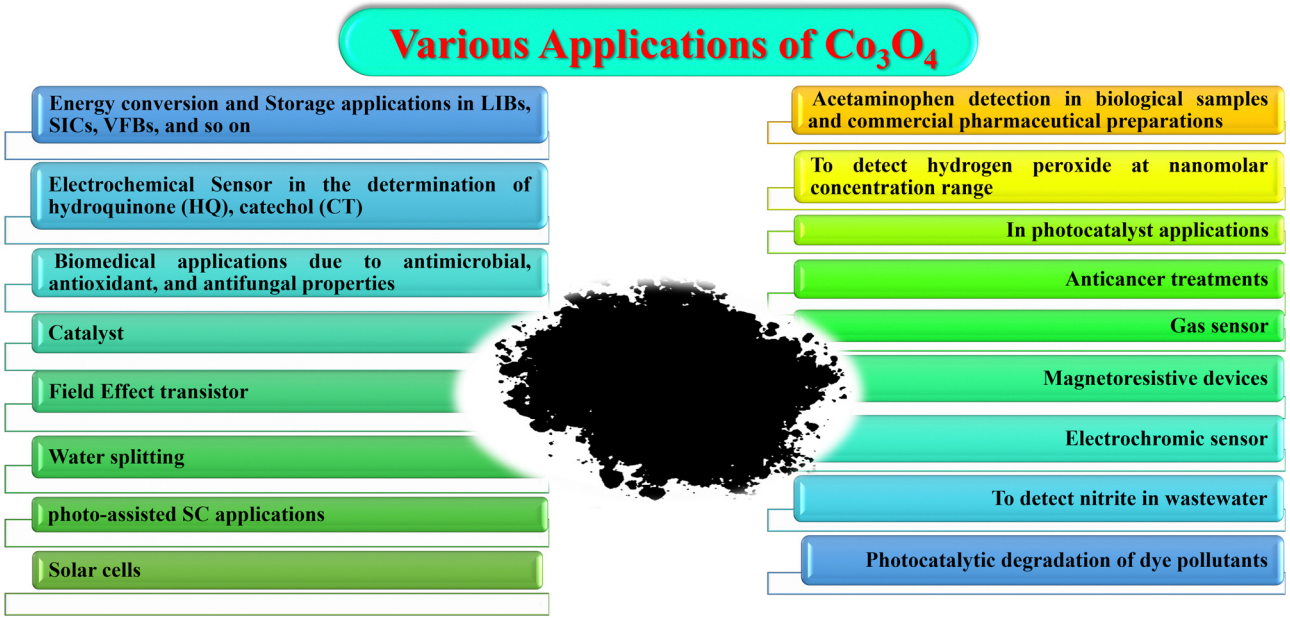

Fig. 3 Various applications of Co_3O_4.

capacity (C_{sp}) from CV and GCD graphs can be calculated using the following equations: from the CV curve,

$$C_s = \frac{\int^I (v)\mathrm{d}v(\text{in A V})}{m(\text{in g})v(\text{in V s}^{-1})\Delta V(\text{in } v)} \text{ in F g}^{-1} \quad (3)$$

$$C_{sp} = \frac{\int^I (v)\mathrm{d}v(\text{inAV})}{\text{m(g)} \times 3600} \text{ in mAhg}^{-1} \quad (4)$$

from the GCD curve,

$$C_s = \frac{I(\text{in A}) \times \Delta t(\text{in s})}{m(\text{in g}) \times \Delta V(\text{in V})} \text{ in F g}^{-1} \quad (5)$$

$$C_{sp} = \frac{\int I(\text{in A})\Delta t(\text{in s})}{m(\text{in g}) \times 3600} \text{ in mA h g}^{-1} \quad (6)$$

where the integration of current over the voltage window will give the total voltammetric charge (in ampere volts); v is the scan rate (in V s^{-1}), I the current (in mA), t the discharge time (in s), m the mass of the active material (in g), v the scan rate (V s^{-1}), and V the potential (in V).[25]

Energy density or volumetric energy density (in W h L^{-1} or W h cm^{-3}) and specific energy or gravimetric density (in W h kg^{-1}) provide information about the amount of energy stored in each volume and a given mass, respectively. How quickly the stored/available energy can be delivered is expressed as power density/volumetric energy density (in W L^{-1}) and specific power (in W kg^{-1}).[85] The specific energy (W h kg^{-1}) depends on the number of charge carriers per unit mass (known as specific charge (A h kg^{-1}). A large number of available charge carriers per unit mass helps to achieve the goal of high specific energy and slow transportation/transfer of ions from the electrolyte into the host electrode reducing the rate capability of the charge/discharge reaction. The following equations were used to estimate the specific energy and power of the device:

$$\text{Specific energy } (\text{inW h kg}^{-1}) = E = \frac{C(\text{in F g}^{-1}) \times \text{V}^2(\text{in V})}{2 \times 3.6} \quad (7)$$

$$\text{Specific power } (\text{in W kg}^{-1}) = P = \frac{E(\text{in W h kg}^{-1}) \times 3600}{t(\text{in s})} \quad (8)$$

where V is the resultant voltage of the device and t is the discharging time.[86] The C-rate is determined by the charging or discharging speed relative to the battery's maximum capacity and the cycle life is measured based on the decay in capacity after a large number of repeated charge–discharge cycles.[17]

Recent strategies to enhance the energy storage performance of Co_3O_4

The addition of heteroatoms (also known as doping) is a critical approach to enhance the active electrode's performance. This process supports improving the material's electrical conductivity, boosts the ion absorption capacity, and adjusts the electronic structure. It helps to improve the electrode material's capacitance and catalytic performance. As reported, this method is the most feasible strategy to significantly enhance the conductivity and catalytic activity of Co_3O_4 by triggering oxygen vacancies.[87] Recently various research groups have focused on the investigation of doped Co_3O_4 with metal ions for energy storage applications. A series of studies have been reported, for example, Co_3O_4 doped with iron (Fe),[88] praseodymium (Pr),[89] tin (Sn)[90,91] antimony (Sb),[92] cerium (Ce),[93] copper (Cu),[94] vanadium (V),[95] and so on. The resulting electrodes have displayed various morphologies, enhanced electrochemical performance, and cycle stability. The Ar-plasma-assisted cobalt oxide with abundant oxygen vacancies showed powerful application in the development of flexible

waterproof rechargeable hybrid zinc batteries (Zn-air batteries and Zn-ion batteries with energy density and power density). These oxygen vacancies promote reversible Co–O ↔ Co–O–OH redox reaction in cobalt oxide and lead to good oxygen reduction reaction and oxygen evolution (ORR/OER) performance.[82] More recently, Zhang *et al.* introduced the metal cations Fe^{3+} and Cu^{2+} as the structure-directing agents to develop Cl-doped Co_3O_4 hierarchical nanospheres. Detailed characterization, along with density functional theory (DFT) analysis, has affirmed the creation of oxygen vacancies in Co_3O_4. This phenomenon results in an augmentation of electroactive sites and a reduction in bandgap width. Consequently, it improves electron transfer efficiency and enhances the surface activity of Co_3O_4.[96] MOFs have gained a lot of attention due to their merits of high porosity, atomic-level dispersion of metal nodes, and tunable structures in a variety of applications. However pristine MOFs suffer from poor electrical conductivity and degradation in the electrolyte.[97] They are combined with TMOs, CPs, and carbon derivatives to solve these problems. Nowadays, metal–organic framework (MOF) derived Co_3O_4[98] is also widely studied; the findings highlighted the durability of the electrode materials at high current densities over a long cycle[99] for improved energy storage applications. Despite its superior properties, the practical use of pristine Co_3O_4 as a supercapacitor is hindered by issues such as low electrical conductivity and significant volume expansion during charge–discharge cycles.[100] Carbon derivatives like graphene have attracted much attention in energy storage due to their properties such as mechanical and chemical stability, high electrical conductivity, and a large theoretical surface area of 2630 $m^2\ g^{-1}$. However, the aggregation and restacking of individual graphene sheets limit the use of available surfaces to achieve high capacitance.[101] The use of conductive polymers in energy storage is attributed to their high charge storage capacity, high electrical conductivity, easy preparation process, and low cost. However, the bulk structure of conducting polymers suffers from low specific capacity, chemical instability, and poor cycling performance due to insufficient access to electrolytes.[102] In this context, the incorporation of Co_3O_4 with CPs and carbon derivatives to develop composite electrode materials can be a good strategy to improve the overall storage performance of Co_3O_4 electrodes. So far, a few reports have been published related to various binary and ternary nanocomposites based on Co_3O_4 including graphene/RuO_2/Co_3O_4,[103] Co_3O_4@Au-decorated PPy,[104] rGO-Co_3O_4-PPy,[105] Co_3O_4@C@PPy,[106] Co_3O_4/rGO,[81,107,108] and the Co_3O_4@polypyrrole/MWCNT hybrid nanocomposite for energy storage applications. Recently, a microbox heterostructure based on Co_3O_4 as a low-cost and high-performance electrocatalyst for rechargeable Zn air batteries was reported.[109] Three-dimensional (3D) hybrid networks based on Co_3O_4 and rGO also displayed high-performance SC applications.[97,110]

2. Co_3O_4 as a supercapacitor

To realize the full potential of active electrode materials, new architectures must be developed that can permit a more efficient charge/ion transport through the electrode.[111] The morphology of synthesized active electrode materials significantly influences their optical and electrochemical performance. Various morphologies, including mesoporous nanoneedles,[112] needle-like nanotubes,[113] hollow octahedral cages,[114] pompon-like microspheres,[13] nanocapsules,[115] 3D hierarchical nanobooks,[116] and more, have been reported for the preparation of Co_3O_4-based active electrodes in energy storage applications (Fig. 4).

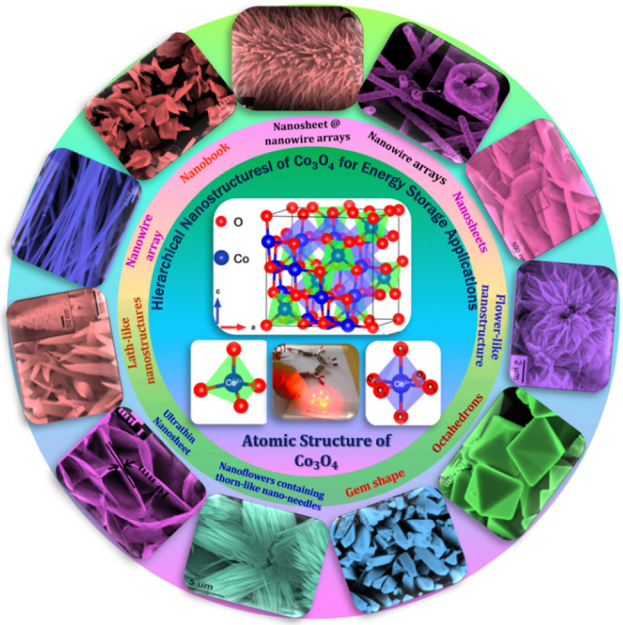

Fig. 4 Various hierarchical nanostructures of Co_3O_4 for energy storage applications.

Hydrothermal method

Based on the pore size, porous materials are classified into three types: micropores (<2 nm), mesopores (2–50 nm), and macropores (>50 nm). To enhance the efficiency during energy conversion and storage, the rapid development of electrode materials with a mesoporous structure is important as the mesoporous structure provides a high surface area as well as a large pore volume. This mesoporous structure effectively adsorbs guest species/ions on the inner and outer surfaces and within the pore space. These nanoporous structures, with large specific surface area, are responsible for their wide range of applications. Selective dissolution or dealloying is the simplest and least expensive method for manufacturing nanoporous metals. In this method, a metal can be easily removed from the alloy or a metallic solution. Deng *et al.* used this approach to synthesize a nanoporous Ni substrate, in which they selectively removed Cu from the electrodeposited Ni–Cu alloy. The high surface area of the formed Ni substrate provides active sites for pseudocapacitance enhancement, and the high porosity provides more accessible pathways for electrolytes and endorses ion transport within the electrode. Therefore, anodically deposited Co oxide on the nanoporous Ni substrate resulted in a high specific capacitance (2086 F g^{-1} at 50 mV s^{-1}).[117]

Due to the unique chemical and physical properties of one-dimensional (1D) architectures such as nanowires, nanorods, and nanotubes, they are found suitable and beneficial for achieving hierarchical assemblies of functional networks.[118] 1D nanostructures provide fast diffusion pathways for ions and electrons and facilitate efficient transfer across the electrode's active surface area. In 2009, Wang *et al*. investigated the optical, magnetic, and supercapacitance properties of nanoporous Co_3O_4 nanorods. High-resolution transmission electron microscopy (HRTEM) analysis displayed the (220) crystal planes of Co_3O_4 nanorods with an interplanar spacing of about 0.285 nm. The grown Co_3O_4 achieved a BET_{SSA} of about 232 $m^2\ g^{-1}$. High BET_{SSA} and nanoporous cobalt oxide nanorods (with a diameter of 400 nm) achieved high specific capacitance (C_s) in an aqueous electrolyte.[119]

Various soft-templating,[120] hard-templating,[121] *in situ* templating,[122] and template-free routes[123] were employed to synthesize mesoporous materials. Along with their benefits, all these approaches have some weaknesses. In the soft templating approach, the formation of the ordered network relies primarily on the interaction between the guest species and the surfactant molecule. The hard templating technique is complex and time-consuming. On the other hand, in the *in situ* templating approach, it is very challenging to overcome the formation of disordered and randomly distributed mesoporous networks, and in the template-free method, it is often difficult to identify developed pore architectures.[124]

Cui *et al*. used cetyltrimethylammonium bromide (CTAB) as a soft template (cationic surfactant), which contributed to the growth of consistent morphology having an ordered chain structure. The reported Co_3O_4 nanorods (diameter 20–50 nm) maintained their initial C_s even after 500 cycles without any significant loss.[125] Recently, Kunhikrishnan reported that the concentration of PVA influences the phase and surface morphology of the electrode. The absence of impurity peaks in XRD ensures the formation of a high-purity spinel Co_3O_4 electrode material. Water-soluble PVA contains hydroxyl groups in long carbon chains that stabilize the material by chelating and physically trapping cobalt ions and species in the polymeric network during the formation of the material. It also inhibits free cobalt ions in the precursor solution so that a slow nucleation process occurs; its optimized concentration offers high-quality nanorods and nanosheets for pseudocapacitive applications.[126]

Mineralizers and additives are inorganic or organic substances, wherein mineralizers (used in high concentrations) are advantageous in controlling the pH of the solution, while additives (in relatively low concentrations) assist in dispersing particles or controlling crystal morphology.[55] Mineralizing agents function to accelerate both crystal growth and nucleation processes.[127] Various mineralizing agents such as NaOH, HMT, and urea are often used. The use of such agents varies the release rate of OH^- and each will result in different morphologies. The OH^- release rate plays an essential role in determining the growth environment, which can be optimized by changing the pH value of the reaction solution.[128] Also, the presence of mineralizing agents during the synthesis process is beneficial in enhancing the adsorption properties and water stability of the product.[129]

The mineralizing agent urea also acts as a hydrolyzing agent and a precipitating agent[130] in the synthesis process of Co_3O_4. It plays an influential role in the evolution of the structure of the functional electrode. While studying the influence of urea (as a precipitant) concentration on the morphology of the Co_3O_4 electrode, the synthesized electrode showed high structural flexibility due to the large aspect ratio. The slow hydrolysis of urea provides OH^- and CO_3^{2-} ions, which offer good crystallinity along their longitudinal axis and may favor the slow and anisotropic growth of nanowires. These carbonate ions contribute to the formation of the intermediate compound cobalt carbonate hydroxide ($Co(CO_3)_{0.5}(OH)\cdot 0.11H_2O$). As reported, glycerol plays a crucial role in the evolution of more uniform morphology, as in its absence a combination of nanowire bundles and large irregular nanoparticles was observed. Almost 98% cyclic retention after 2000 cycles resulted in the tailored morphology.[131] Formamide ($COHNH_2$) can also be used instead of urea to serve as both hydrolyzing and precipitating agent.[132]

A high specific capacitance per unit area is highly desirable for practical supercapacitor electrodes. However, high mass loading usually increases the ''dead'' material that restricts the available accessible sites for electrolytes in the electrode material and thus prevents the utilization efficiency of the material. However, increased specific capacitance with high mass loading indicates high utilization efficiency of the electrode. Overstated specific capacitances have often been detected even at very low mass loadings of the active material (<1 mg).[133] Yu *et al*. demonstrated that, like urea, the optimized amount of NH_4F is a potential promoter of mass loading on the current collector and supports the evolution of different morphologies. The higher amount of NH_4F produces more ordered and distinct hierarchical structures. The morphological evolution after 1 h and 4 h due to variations in NH_4F concentration is shown in Fig. 5(a–d). The CV, GCD, and areal capacitance variations are depicted in Fig. 5(e–h), respectively. The CV profile reveals that the redox peaks of the four electrodes are found at specific potential locations, which could be attributed to the different sites available due to their different morphologies. It also confirms that the thin-nanowire-cluster morphology (fabricated with a 1 : 5 ratio of Co^{2+} : NH_4F) acquires higher areal capacitance (1.92 F cm^{-2}) and better rate capability than other synthesized samples.[134] The purpose of efficient charge transfer was attained with the development of self-supported hollow Co_3O_4 nanowire arrays as shown in Fig. 6(a) and its magnified image in Fig. 6(b) (the inset corresponds to the side view of the synthesized nanowire). For better cycling performance, hollow nanowire design plays a pivotal role. It further enriches the diffusion kinetics of electrons and ions by providing numerous active sites and small internal resistance. Here, the synergistic effect of axial screw dislocations and the Kirkendall effect resulted in the Co_3O_4 electrode with a well-aligned hollow nanowire array (average diameter of 20 nm). The axial screw dislocations on the crystal surface are responsible for orientating 1D β-$Co(OH)_2$ nanowires along the (001) direction. This axial screw dislocation

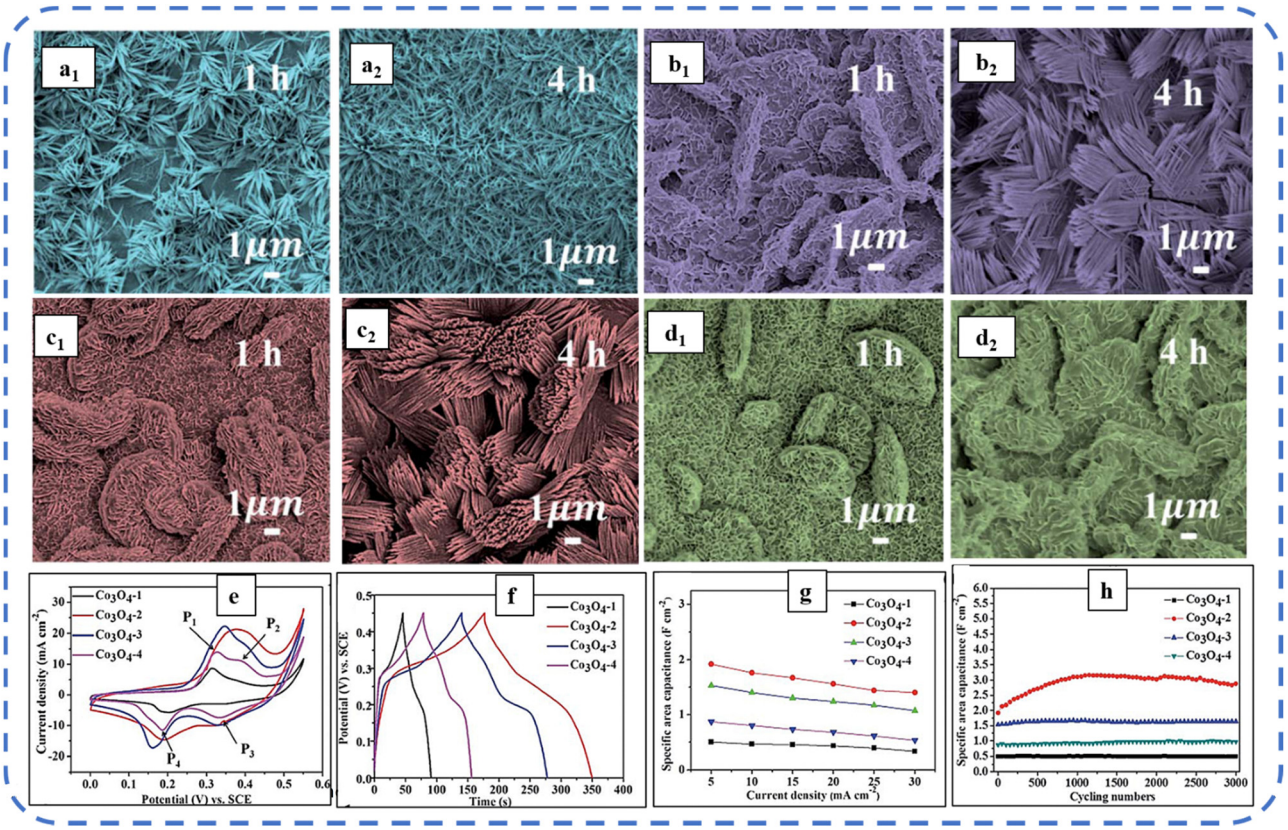

Fig. 5 SEM images of morphology evolution at 1 h and 4 h for (a_1) and (a_2) nanowires, (b_1) and (b_2) thin nanowire-clusters, (c_1) and (c_2) thick nanowire-clusters and (d_1) and (d_2) fan-like bulks of Co_3O_4 electrodes with varied NH_4F concentration. (e) CV, (f) GCD, and (g) variation of capacitance as a function of current density. (h) Capacitance as a function of cycle number of as-synthesized samples. Reproduced with permission from ref. 134. Copyright 2016, RSC publications.

contributes to providing active sites for the continued attachment of surface-adsorbed atoms, thereby accelerating the growth of β-$Co(OH)_2$ and facilitating the transformation of β-$Co(OH)_2$ nanowires into hollow Co_3O_4 nanowires (refer to the HRTEM image in Fig. 6(c) and SAED pattern in Fig. 6(d)). In the Kirkendall effect, an inward flow of vacancies occurs to balance the fast outward transport of cations and can condense into voids at the centre of the nanowire. The hollow centre and the open space between the individual nanowires benefit sustaining the structure during cycling and relaxing the volume expansion. The Co_3O_4 nanowires retain 91% capacitance after 7500 cycles at 2 A g^{-1} (Fig. 6(e)).[135] Yuan *et al.* fabricated large-scale self-supported Co_3O_4 nanoparticles (NPs) and reported typical advantages of using HNO_3-etched nickel sheets as conducting substrates. Even after 8 h powerful sonication treatment, they can still adhere strongly to the HNO_3 pre-treated nickel foam (Fig. 6(f–h)). CV profiles as shown in Fig. 6(i) show a similar geometry without any distortion (at both extreme potentials) even at a higher scan rate of 500 mV s^{-1}, disclosing the excellent electrochemical reversible redox reaction behavior to achieve good reversibility and rate capability. Furthermore, even at high current densities, only 7% capacitance loss was observed after 2200 GCD cycles.[136]

Subsequently, Yao *et al.* developed 1D hierarchical hollow Co_3O_4 nanotubes using activated carbon and guanidine hydrochloride as the hard template and precipitant, respectively. The N_2 adsorption–desorption isotherms demonstrate a type-IV isotherm with a large hysteresis loop due to capillary condensation resulting in the formation of numerous mesopores in 1D hollow Co_3O_4 nanotubes. The synthesized Co_3O_4 electrode achieved a C_s of 1006 F g^{-1} at 1 A g^{-1},[137] which is much higher than that obtained with L-arginine as a precipitant (483.8 F g^{-1} at 1 A g^{-1}).[138] Recently, Co_3O_4 hierarchical hollow spheres grown on N-doped carbon substrates have been reported to retain more than 98% of their initial capacitance after 10 000 cycles.[139] Afterwards, a self-supported Co_3O_4 nanowire array with sharp tips (average diameter of 70 nm and a length of 25 mm) was successfully developed by Xia *et al.* The pseudocapacitive behavior elucidated by CV confirms the two characteristics of redox couples A_1/C_1 corresponding to the conversion between CoOOH and Co_3O_4 ($Co_3O_4 + OH^- + H_2O \leftrightarrow CoOOH + e^-$) and A_2/C_2 is attributed to the change between CoOOH and CoO_2.

It can be represented by the following reactions, respectively:

$$Co_3O_4 + OH^- + H_2O \leftrightarrow 3CoOOH + e^-$$

$$CoOOH + OH^- \leftrightarrow CoO_2 + H_2O + e^-$$

As the scan rate increases, the oxidation and reduction peaks shift to higher and lower potentials, respectively, and only one oxidation peak and one reduction peak are observed at 200 mV s^{-1}. The GCD study showed that after 1000 cycles,

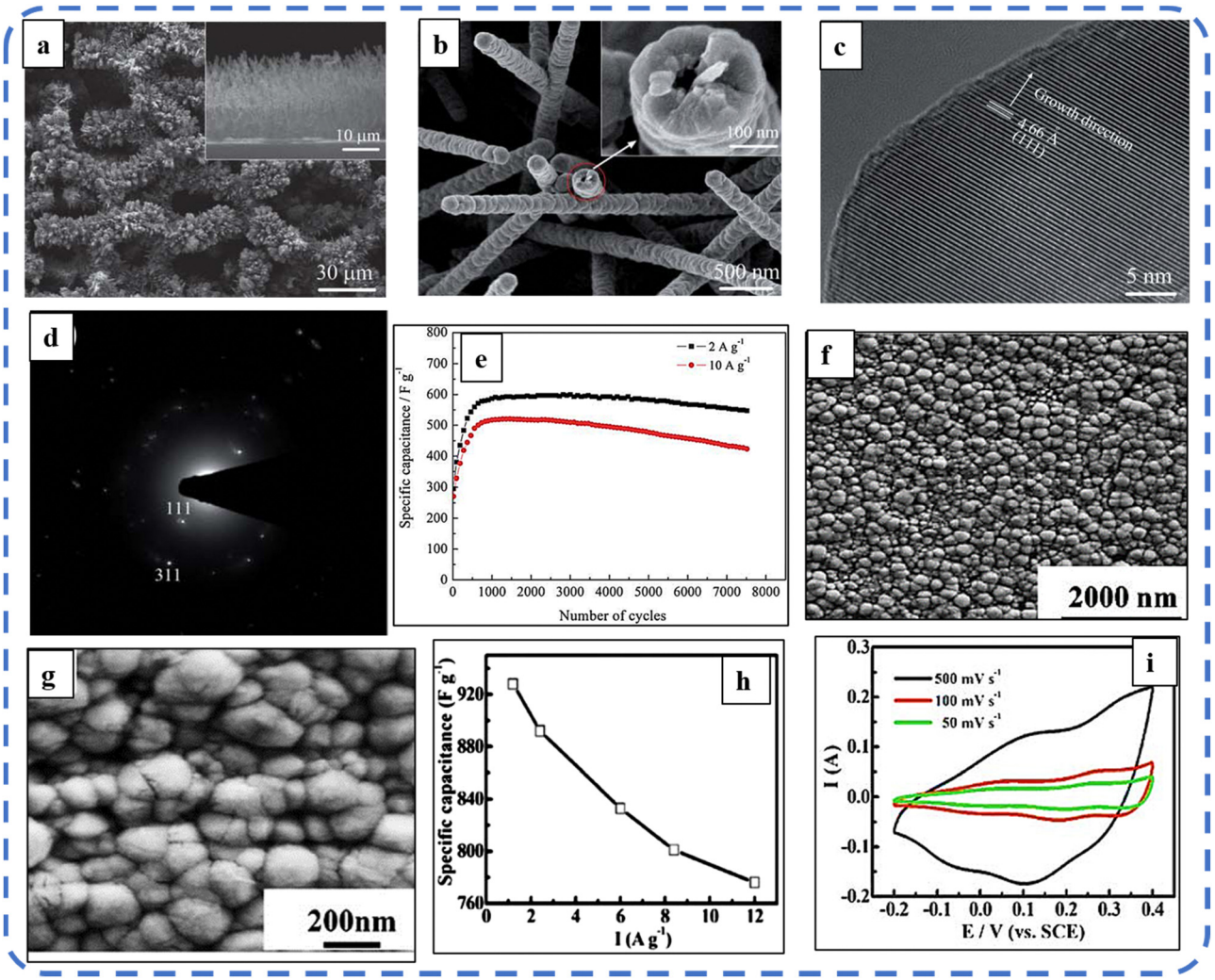

Fig. 6 (a) and (b) SEM images of self-supported Co_3O_4 at various magnifications. (c) HRTEM image, (d) SEAD pattern and (e) cycling performance at 2 and 10 A g^{-1}. Reproduced with permission from ref. 135. Copyright 2011 RSC publications. (f) and (g) SEM images of Co_3O_4 nanoparticles at different magnifications. (h) Capacitance at various current densities. (i) CV at different scan rates. Reproduced with permission from ref. 136. Copyright 2011 RSC publications.

nanowires become more activated, and the electrolyte gradually penetrates the Co_3O_4 nanowire structure, utilizes more sites, and contributes to the high capacitance (754 F g^{-1} at 2 A g^{-1}). TEM analysis demonstrated that the unique nanowire array morphology preserves and maintains the structural integrity even after 4000 cycles and is responsible for the good electrochemical performance of the electrode.[140]

Howli *et al.* synthesized porous Co_3O_4 nanowires on a flexible carbon fiber and achieved a C_s of about 3290 F g^{-1} at a scan rate of 5 mV s^{-1}, which is very close to that of the theoretical capacitance value. The high capacitance is attributed to the ion movement within the porous nanowires (schematic representation is depicted in Fig. 7(a)). Further, they developed an ASC symmetric supercapacitor device, using active electrodes based on Co_3O_4 nanowires and a (PVA)/KOH gel electrolyte, and a schematic of the synthesized device is shown in Fig. 7(b). The synthesized ASC symmetric device attains a high specific energy of 6.7 W h kg^{-1} at a specific power of 5000 W kg^{-1}. ASC displays the quasi-rectangular shape of the CV profile, which confirms the ideal capacitive nature. The device retained 95.3% capacitance after 5000 GCD cycles, with a slight increase in charge transfer resistance from 2.8 to 3.6 Ω during these cycles (refer to Fig. 7(g and h)). With high specific power, the four devices in the series can light up 5 LEDs for 1 min illustrating the practical use of the synthesized symmetrical supercapacitor (SSC) device.[141]

Binder-assisted growth of active electrodes is an ideal strategy to develop a more adhesive film and to reduce pulverization. However, binders confine the availability of active sites and increase the resistance between the current collector and the electrode. Binder-free growth aids in evading the uneven growth of the active material on the conducting substrate.[142] The binder- and template-free approach is still found to be useful and still preferred in developing the Co_3O_4 nanostructures on conducting substrates.[143] With this rational approach, Adhikari *et al.* studied the influence of urea concentration on

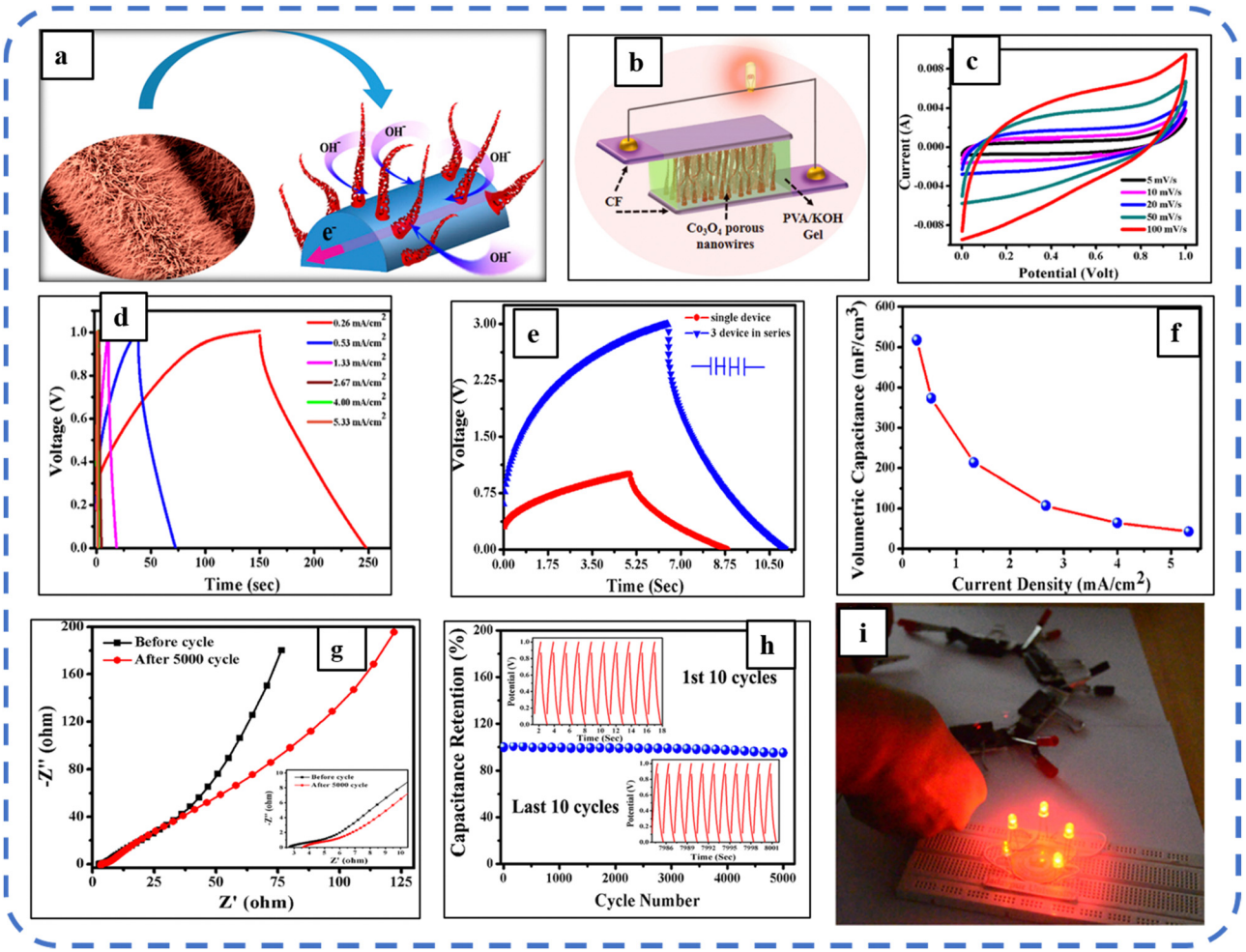

Fig. 7 (a) Schematic representation of ion movement within the unique structure. (b) Symmetric device based on Co_3O_4 nanowires. (c) CV and (d) GCD performance of the synthesized device. (e) Charging–discharging profile of the single and 3 devices in series. (f) Volumetric capacitance as a function of current density. (g) Impedance spectra, (h) cyclic performance and (i) digital photographs of glowing LEDs using the synthesized devices connected in series. Reproduced with permission from ref. 141. Copyright 2017 ACS Publications.

the surface area, morphology, and electrochemical properties of the developed electrodes. They concluded that low urea concentration is effective in achieving a high surface area structure with high specific capacitance. The different morphologies are the consequence of variation in the urea concentration, as it changes the basicity of the reaction mixture. Above 80 °C, urea hydrolyses and operates as a steady source of OH^- ions. This helps to reduce the formation of agglomeration/close-packed structures. With the optimized urea concentration, good cycling performance of the Co_3O_4 electrode was reported.[144] Likewise, Awais *et al.* developed Co_3O_4 nanowires using a binder-free growth approach. Nyquist plot analysis performed over the 0.01–10 MHz frequency range showed the zero charge transfer resistance (R_{ct}) and very low ESR (1 Ω) of the electrode. As a result, Co_3O_4 nanowires exhibited a C_s of 1140 F g^{-1} at 1 A g^{-1} in a 3 M KOH electrolyte. The as-synthesized nanowires displayed 93.3% cycle stability and 100.2% coulombic efficiency, after 5000 GCD cycles at 10 A g^{-1} current density. Further, the assembled hybrid supercapacitor device based on Co_3O_4 as the positive electrode and activated carbon as the negative electrode showed excellent electrochemical performance. The synergy between the faradaic and non-faradaic reaction mechanisms of the hybrid electrode achieved a maximum specific power of 11.80 kW kg^{-1} at a specific energy of 18.20 W h kg^{-1} with high rate capability.[145]

2D and 3D nanoarchitectures with excellent properties such as high porosity, large surface area, and high ion storage capacity are always helpful in accomplishing the goal of excellent EES device performance. 3D nanostructures are more beneficial over 1D and 2D morphologies in EES applications, due to their interesting features such as providing large channels for electrolyte ions by acting as ion buffering reservoirs and providing structural mechanical stability.[146] Large research groups are continuously striving to synthesize various nanostructured morphologies that are more reliable and useful for improving the overall performance of EES electrodes/devices. Inspired by this, Maher *et al.* developed ultra-layered well-arranged uniform rectangular 2D layered sheets of Co_3O_4 for energy storage applications. The neutral surfactant Triton X-100 assisted in decreasing the aggregation and development of

a 2-fold layered structure. The resulting porous electrode with a high surface area displayed exceptional cyclic, structural, and electrochemical stability, almost 100% coulombic efficiency, and 98.5% capacitance retention after 2000 continuous GCD cycles at a high current density of 16 A g^{-1}.[147] Hu *et al.* developed surfactant-free monodispersed mesoporous Co_3O_4 nanosheets. The size of the nanosheets is about 15 nm thick and about 1 μm in width. GCD studies revealed that the C_s of the electrode varied from 880 F g^{-1} to 54 F g^{-1} at a corresponding discharge current density of 1 to 10 A g^{-1}.[130] Qui *et al.* reported nickel foam-supported ultrathin Co_3O_4 nanosheets (NSAs) as highly mesoporous microstructures with pore sizes of 2–10 nm. Fig. 8(a) depicts the SEM image of Co_3O_4 NSAs and Fig. 8(b) shows the schematic illustration of the advantages of building mesoporous Co_3O_4 ultrathin nanosheets. With this distinctive microstructure, they act as a strong reservoir for OH^- and facilitate sufficient redox reactions at high current densities. The highly linear and symmetrical CV curves of Co_3O_4 nanosheets were observed at various current densities (1 to 15 A g^{-1}) and they had delivered a maximum C_s of about 2194 F g^{-1} at 1 A g^{-1} due to a very small R_{ct} of about 2 Ω (Fig. 8(d)). The Ragone plots in Fig. 8(f) show that even at a high specific power of 3.8 kW kg^{-1} the Co_3O_4 NSAs achieved a specific energy of 41.6 W h kg^{-1}.[148] The same group developed the ultrathin hierarchical 3D mesoporous (pore size 3–8 nm) structures of Co_3O_4 with conch-like nanostructure arrays *via* optimized use of urea and NH_4F. Fig. 8(g) depicts a schematic illustration of the grown structure and Fig. 8(h) shows the SEM images at distinct magnifications. This unique morphology with fast redox kinetics and high mass loading (5 mg cm^{-2}) achieved an areal capacitance of 4.11 F cm^{-2} at a current density of 5-mA cm^{-2} in a 2 M NaOH electrolyte. The fast redox kinetics is attributed to the high BET_{SSA} (82.5 m^2 g^{-1}) and large pore-size distribution in the structure. This provides short diffusion pathways and facilitates multiple electroactive sites for rapid redox reactions at the electrode–electrolyte interface.

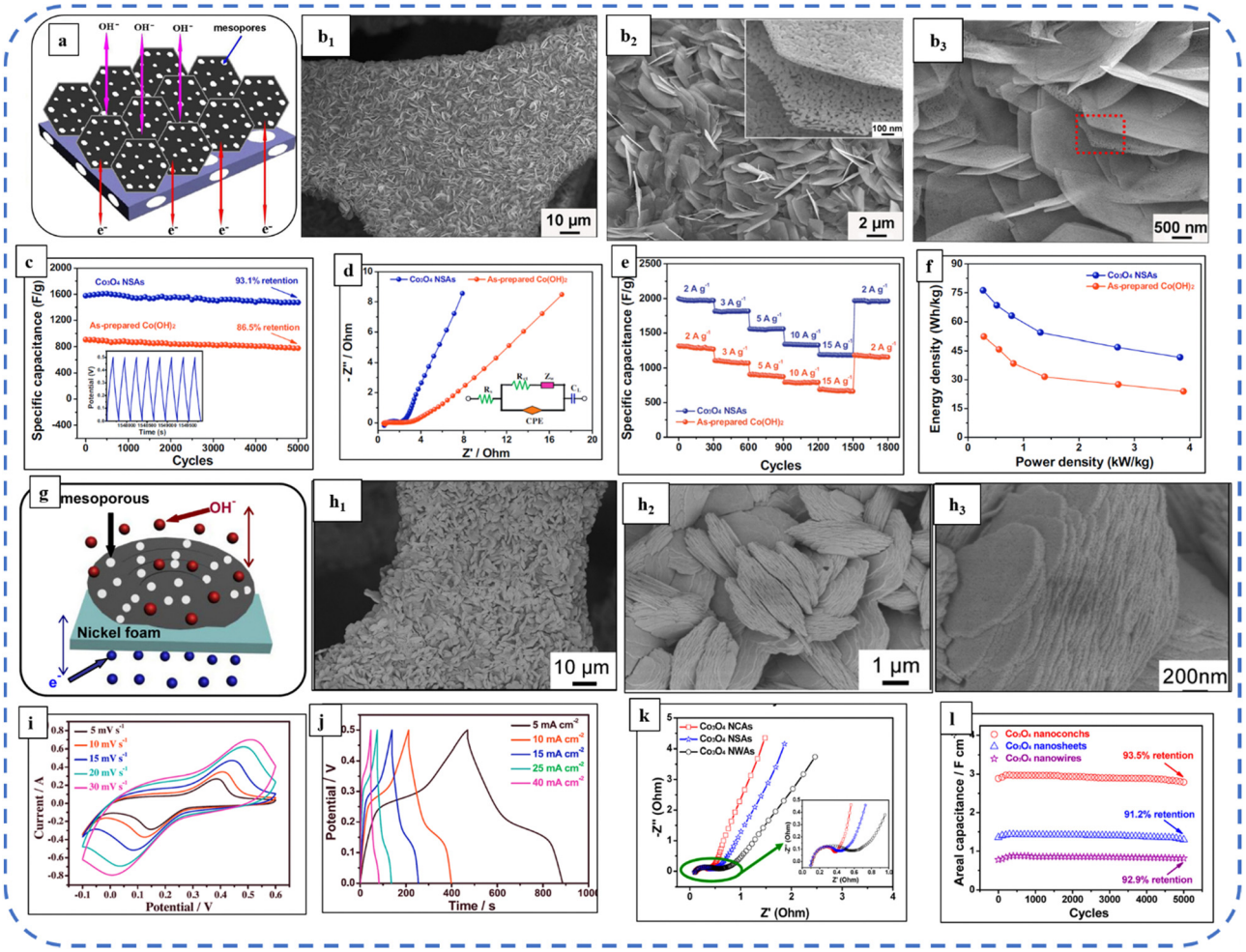

Fig. 8 (a) Schematic illustration of advantages of the synthesized nanosheet electrode. (b_1)–(b_3) SEM images of the as-synthesized sample at different magnifications. (c) Cycling performance. (d) Nyquist plots. (e) Rate performance at different scan rates. (f) Ragone plots of Co_3O_4 NSAs and as-prepared $Co(OH)_2$ electrodes. Reproduced with permission from ref. 148. Copyright 2015 Elsevier. (g) schematic illustration of advantages of the synthesized nanoconch structure. (h_1)–(h_3) SEM images at different magnifications. (i) CV, (j) GCD and (k) Nyquist plots. (l) Cycling performance of the synthesized electrode at a current density of 25 mA cm^{-2}. Reproduced with permission from ref. 149. Copyright 2014, Elsevier.

Moreover, only 6.4% loss was obtained after 5000 cycles, showing the excellent cycle stability of the electrode (Fig. 8(l)).[149]

The ultrathin mesoporous Co_3O_4 nanosheets (size 2.5–5 nm) (Fig. 9(a)) with a BET surface area of 91.482 m^2 g^{-1} were fabricated. The nanosheet structure provides enough channels and space for the transport of ions/electrons at the electrode/electrolyte interface and is responsible for superior pseudocapacitive performance in 2 M NaOH solution with a wide potential window (1.4 V) and an areal capacity of 610 mF cm^{-2} at a current density of 1 mA cm^{-2}. To investigate the practical application, Wang *et al*. designed an asymmetric supercapacitor device using the Co_3O_4 electrode as the positive electrode and porous carbon as the negative electrode (the schematic is depicted in Fig. 9(c)). Fig. 9(d) shows the CV of the developed asymmetric device at different scan rates. The device retains 90.2% of its initial capacitance after 3000 cycles (Fig. 9(e)). The remarkable performance of the device can be easily estimated as the device can keep the LEDs on even after 220 seconds (Fig. 9(f and g)).[150]

Ding *et al*. studied the influence of an ion-assisted hydrothermal approach on the morphology of the energy storage active electrode. In this, electrodes were prepared using various ion additives such as Na^+, Cl^-, NO_3^-, Ac^-, $C_2O_4^-$, CO_3^{2}, K^+, and Mg^{2+}, and the corresponding growth mechanism was explored. A 3D hierarchical flower-like Co_3O_4 structure, constructed with NaCl additive and HMT hydrolysis agents, yielded hexagonal nanosheets. The resulting electrode demonstrated exceptional capacitance retention, maintaining 96.07% even after 10 000 cycles.[151] Subsequently, Yetim *et al*. developed nanosheets, nanospheres, poppy flower-like structures, and clover field-like structures of Co_3O_4 using various additives such as urea, polyvinylpyrrolidone, ethylenediamine, and sodium hydroxide, respectively. The electrochemical activity examined by CV confirmed that the charge is stored with a reversible faradaic redox reaction process and all samples exhibited pseudocapacitive behavior.[152] Later, Umar *et al*. developed and studied the supercapacitor characteristics of perforated Co_3O_4 nanosheets using HMT. Interestingly, HMT accomplishes two important roles here: first, it forms a stable chelate complex with metal ions while acting as a chelating agent, and secondly, as a hydrolyzing agent, it hydrolyzes to release OH^- ions and helps in the formation of metal hydroxides. The perforated nanosheets exhibited a high specific capacitance of 1455.64 F g^{-1} at 1 A g^{-1} current density. Additionally, the fabricated symmetric device shows high specific energy and specific power of about 11.26 W h kg^{-1} and 1558.44 W kg^{-1} respectively, much higher than those reported previously.[153]

Afterward, Wang *et al*. elucidated the influence of slight temperature variations, which resulted in a substantial difference in the Co_3O_4 microstructure. Different consequent lath-like, necklace-like, and net-like morphologies are depicted in Fig. 10(a–c). Among these, mesoporous net-like Co_3O_4 nanostructures (which resulted at 50 °C) achieved a C_s of 1090 F g^{-1} with a high mass loading of 1.4 mg cm^{-2}. The electrode developed at 50 °C achieved a higher surface-to-volume ratio and enclosed a large area under the cyclic voltammogram (CV) curve, revealing a higher amount of charge storage compared to other synthesized structures. The study demonstrated that small variations in the synthesis process can produce substantial changes in the microstructure and consequently amazing electrochemical performances (Fig. 10(f)).[154]

Many surfactants and polymers with different functional groups are used in Co_3O_4 synthesis to control its morphology. Surfactants and polymers are primarily used in chemical

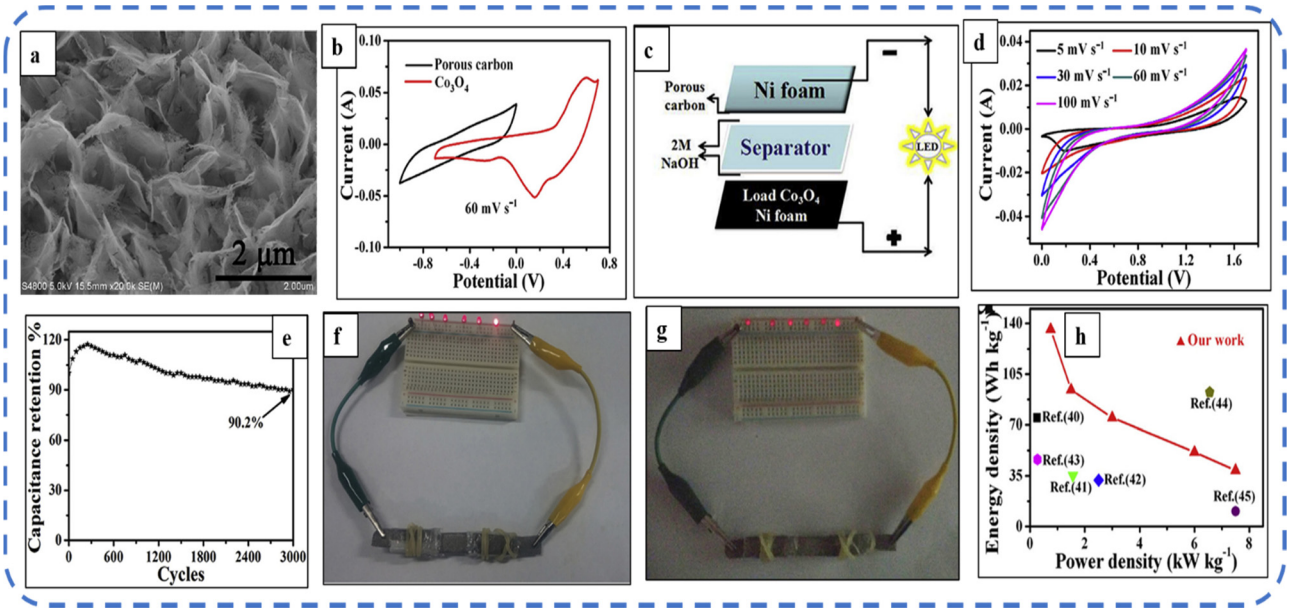

Fig. 9 (a) FESEM image of mesoporous Co_3O_4 ultrathin nanosheets. (b) CV curves of porous carbon and Co_3O_4. (c) Schematic of an asymmetric device. (d) CV curves and (e) cycling performance of the Co_3O_4//C device. (f) and (g) Lighting of LEDs after 1 and 220 s respectively. (h) Ragone plots. Reproduced with permission from ref. 150. Copyright 2016 Elsevier.

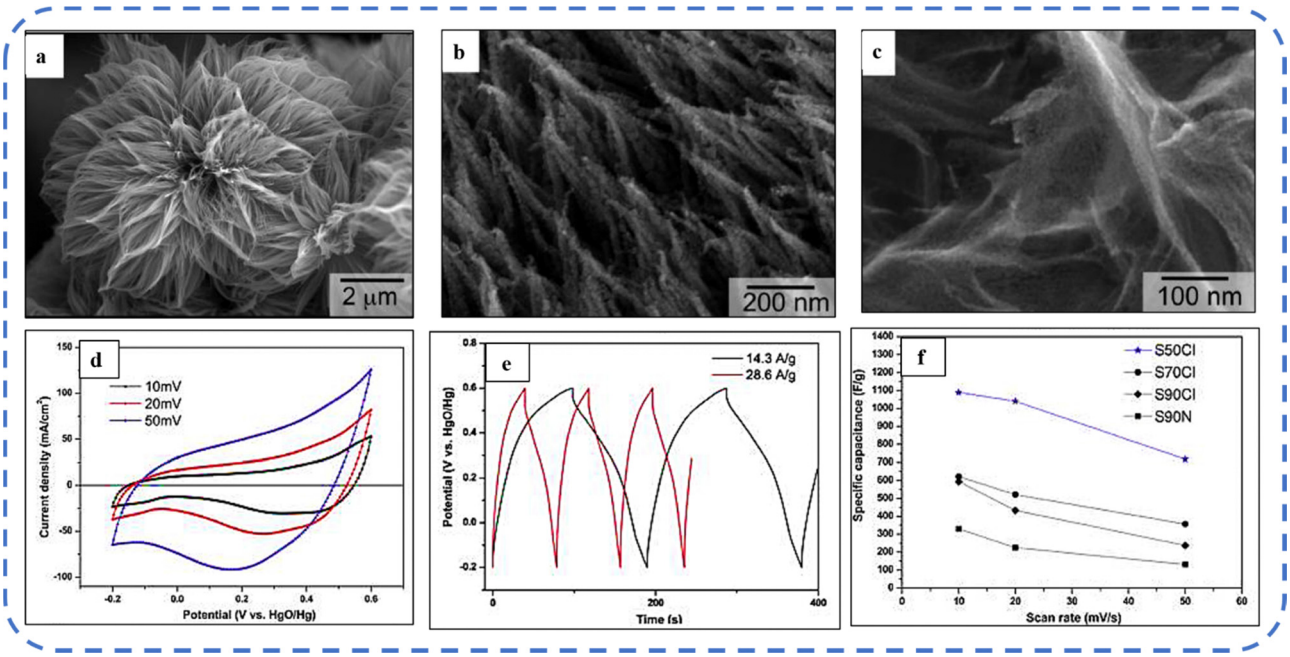

Fig. 10 SEM images of (a) flower-like nanostructure that resulted at 90 °C. (b) Necklace-like nanostructure that resulted at 70 °C. (c) Net-like Co_3O_4 nanostructures that resulted at 50 °C. (d) CV and (e) GCD of the net-like Co_3O_4 nanostructure. (f) Capacitance variation of all synthesized samples *vs.* scan rate. Reproduced with permission from ref. 154. Copyright 2011 ACS publication.

reactions to preclude particle agglomeration and to control the growth of nanoparticles. But their removal often needs the repeated cleaning of the prepared particles or electrodes.[144] Subsequently, Lester *et al.* synthesized cubic Co_3O_4 nanoparticles by using cobalt(II) acetate tetrahydrate as a precursor without any surfactant. The nanoparticles with an average size of 15–30 nm resulted in an optimized reaction time. The results showed that, as the temperature increases, the particle size increases, and simultaneously the conversion rate of cobalt(II) acetate tetrahydrate to Co_3O_4 nanoparticles also increases.[155]

Various anionic (SDS), cationic (CTAB), and non-ionic (Triton X-100) surfactant molecules were used to develop different Co_3O_4 nanostructures. It is realistic to expect that the nucleation growth will vary due to differences in selective adsorption and interaction of surfactant molecules with inorganic precursors. These surfactants strongly influence the physicochemical properties of the active electrode. The presence of these three surfactants resulted in distinct morphologies such as bundle-like-sheet, nest-like, and flake-like morphologies with BET_{SSA} ranging from 50 to 77 $m^2\ g^{-1}$. The nest-like morphology that emanated from the presence of SDS, with a wide distribution of mesopores and macropores, achieved the highest C_s among the three samples and retained 80% of the initial capacitance after 1000 GCD cycles.[156] Later, the same group synthesized Co_3O_4 flakes utilizing CTAB and NH_4F additives. In a 2 M KOH electrolyte this electrode achieved a C_s of about 1820 F g^{-1} at 1 A g^{-1} current density. The schematic illustration of the synthesis process and SEM images are shown in Fig. 11(a). Fig. 11(b–d) indicates the CV, GCD, and variation of specific capacitance for various current densities, respectively.[157] More recently, Velhal *et al.* reported the CTAB and Triton X-100 mediated cobalt oxide micro- and nanostructures with excellent electrochemical stability over large charge–discharge cycles.[158]

Besides, Hongmei *et al.* reported the 3D gem-shaped Co_3O_4 nanostructures with a pore size and pore volume of 13.6 nm and 0.069 cc g^{-1}, respectively, in a mesoporous regime on a nickel foam substrate. The as-synthesized Co_3O_4 nanomaterial achieved excellent C_s (1060.0 F g^{-1} at 1 A g^{-1}) in a 6 M KOH electrolyte and long-term cycling stability. Moreover, the fabricated asymmetric Co_3O_4//AC supercapacitor with the as-prepared Co_3O_4 as the positive electrode provided a high specific energy of 44.99 W h kg^{-1} at a specific power of 200 W kg^{-1}. The excellent electrochemical performances can be attributed to the high BET_{SSA} (117.7 $m^2\ g^{-1}$), unique uniform 3D gem morphology with suitable pore structure, and conductivity of the substrate.[159]

Apart from the surfactant, the solvent used plays a crucial role in shaping the morphology of the electrode material. Ouyang *et al.* investigated the influence of solvents (of varied volume ratio of water and ethanol) on the morphology and electrochemical properties of the electrode. The developed honeycomb-like Co_3O_4 electrode in C_2H_5OH/H_2O solution (with a volume ratio of 1 : 1) exhibited superior C_s than that in pure water and pure ethanol solvents.[160] Subsequently, Samal *et al.* synthesized a nanocube Co_3O_4 electrode while investigating the effect of synthesis temperature between 100 °C and 180 °C on growth and surface morphology (Fig. 12(a)). The studies showed that electrodes synthesized at 180 °C exhibited high reversibility due to easy adsorption/desorption of ions from the aqueous electrolyte. As observed in the Raman shift analysis (shown in Fig. 12(b)), the intensity of the characteristic bands of Co_3O_4 (positioned at 475 cm^{-1}, 518 cm^{-1}, and 682 cm^{-1})

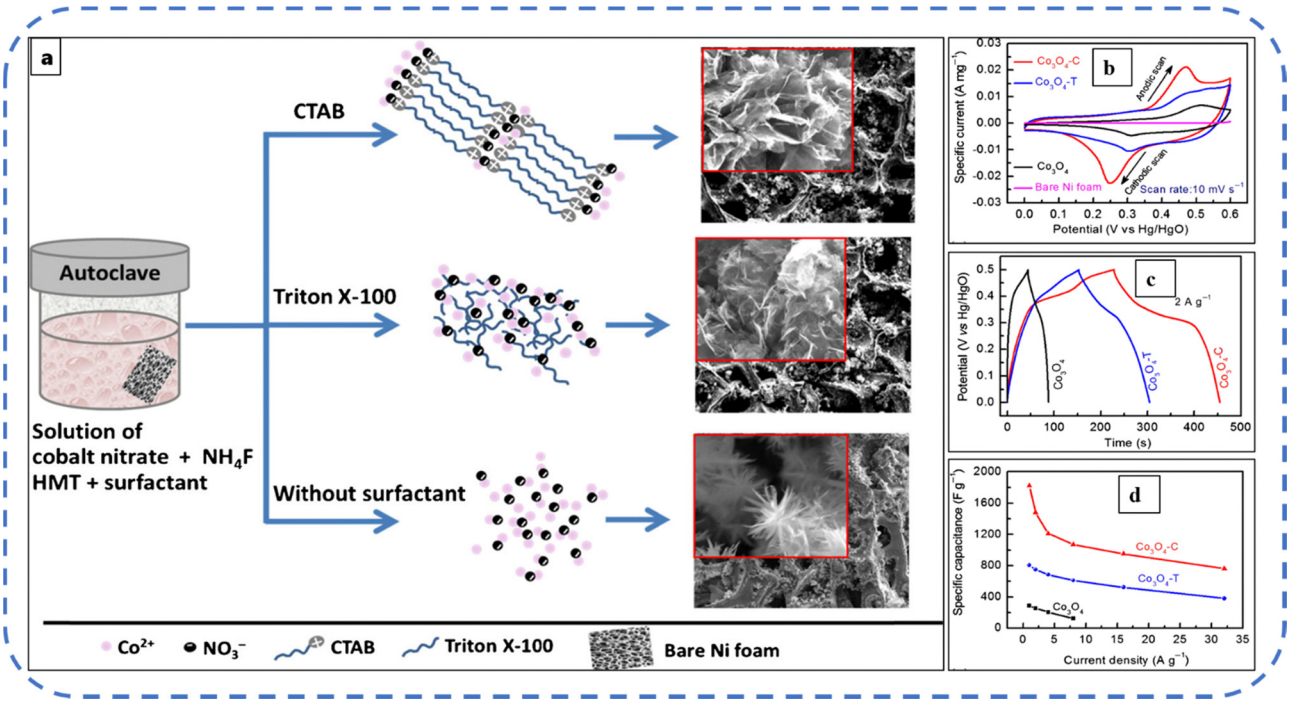

Fig. 11 (a) Schematic illustration of the synthesis process of various Co_3O_4 morphologies with and without the surfactant (with SEM images). (b) CV, (c) GCD and (d) specific capacitance variation with respect to the current density of the as-synthesized Co_3O_4 nanostructures. Reproduced with permission from ref. 157. Copyright 2017 Springer Nature.

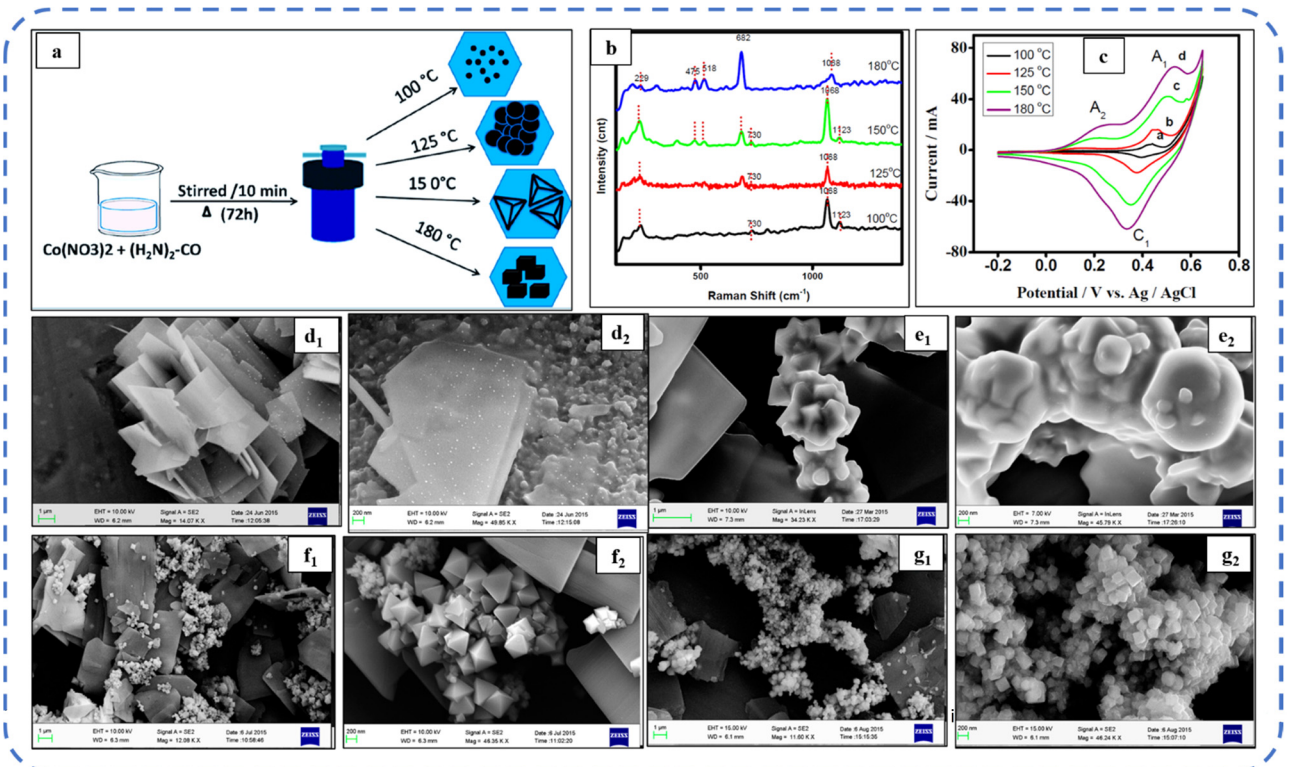

Fig. 12 (a) Schematic illustration of the synthesis process and the resulting structures. (b) Raman shift and (c) CV of all synthesized samples at 50 mV s^{-1}. Low and high magnification images of the Co_3O_4 electrode obtained at (d_1) and (d_2) 100 °C, (e_1) and (e_2) 125 °C, (f_1) and (f_2) 150 °C, and (g_1) and (g_2) 180 °C. Reproduced with permission from ref. 161. Copyright 2017 MDPI publications.

progressively increases with temperature. Fig. 12(d–g) depicts the various morphologies developed as the temperature rises from 100 °C to 180 °C. In particular, at 100 °C, SEM investigations reveal the flake-like nanostructures which have the initial growth of cubes on their surface (Fig. 12(d1 and d2)). At 125 °C, the surface morphology showed flake-like nanostructures (Fig. 12(e1 and e2)). Then, non-uniform pyramidal-like shapes were observed at 150 °C (Fig. 12(f1 and f2)) and with a further increase in temperature (180 °C) a large quantity of cube-like nanostructures were noticed (Fig. 12(g_1 and g_2)). A well-resolved redox peak was observed at 180 °C in the CV as shown in Fig. 12c and that resulted in a C_s of 833 F g^{-1} at 50 mV s^{-1} scan rate.[161]

Studies have shown that a lower synthesis temperature results in the formation of more promising microstructures and benefits from a higher surface-to-volume ratio, with nearly equal mass loading. Therefore, Feng *et al.* attempted to transform Co(II) → Co(III) at the lowest possible temperature. For this, they used cobalt complex ammonia during the synthesis process and oxidized the $[Co(NH_3)_6]_2$ precursor rather than the generally used $Co(OH)_2$. During this, they synthesized Co_3O_4 microspheres at 100 °C reaction temperature with 850 F g^{-1} C_s at 1 A g^{-1} current density.[162] With the same approach, they demonstrated the large-scale preparation of sub-3 nm atomic layer Co_3O_4 nanofilms (the schematic of synthesis steps is illustrated in Fig. 13(a and b)) with an ultrahigh specific capacitance of 1400 F g^{-1}. The development of Co_3O_4 nanofilms with uniform thickness and smooth surfaces is observed with a high-resolution 3D scanning probe microscopy (SPM) image shown in Fig. 13(d). The selected area electron diffraction (SAED) image study confirms the polycrystalline characteristics with the five concentric diffraction rings assigned to the (111), (220), (311), (511), and (531) planes of Co_3O_4.[163] Afterwards, they developed hollow Co_3O_4 microspheres with nanosized shells (50 nm in size) at 120 °C without using any template, organic reagent and additional calcination (schematic steps are depicted in Fig. 13(a and c)). The size and quality of these microsphere cavities are directly related to the amount of H_2O_2. A sufficient amount of H_2O_2 is suitable to obtain hollow microspheres; otherwise, it will result in the formation of a solid sphere. The decomposition of H_2O_2 produces the O_2 bubbles that serve as the center of core–shell structure formation. Fig. 13(g and h) shows the high-magnification SEM and TEM images of hollow microspheres. It can be seen from the inset of Fig. 13(i) that after 1000 cycles, a slight change in charge transfer resistance was noticed. The as-synthesized electrode displayed a maximum C_s of 1227 F g^{-1} and 97.5% initial capacitance retention after 1000 GCD cycles[164] The appropriate amount of H_2O_2 in the reaction mixture yields good-quality Co_3O_4 nanostructures such as nanoparticles, nanodiscs, and well-defined octahedral nanostructures.[165] Several reports have shown that high mass loading results in very low capacitance, typically in the range of 0.1–1.0 F cm^{-2}. However,

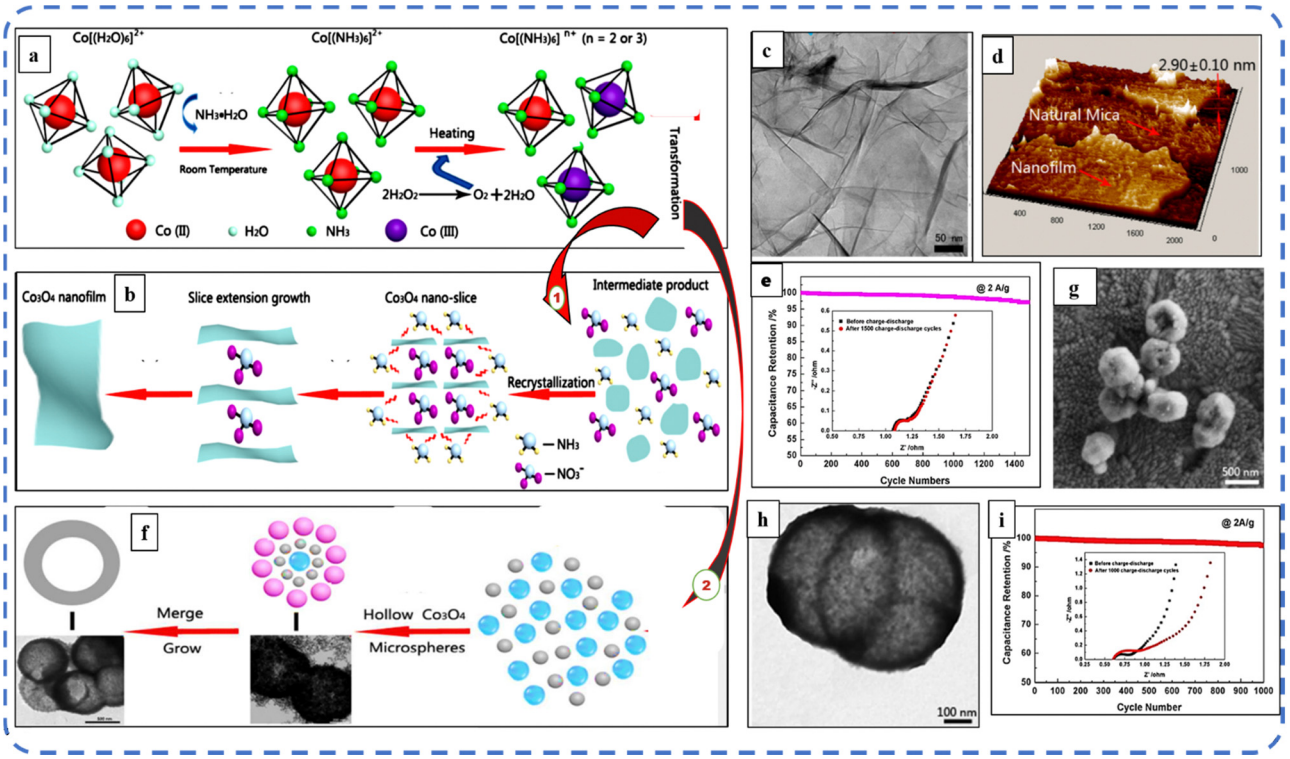

Fig. 13 (a) and (b) Schematic of the formation of an atomic layer Co_3O_4 nanofilm. (c) TEM, (d) high-resolution 3D scanning probe microscopy (SPM) image of Co_3O_4 nanofilm and (e) capacitance retention and the inset shows the EIS of nanofilms before and after 1500 GCD cycles. Reproduced with permission from ref. 163. Copyright 2015 ACS Publications. (a) and (f) Schematic of the formation of hollow Co_3O_4 microspheres with nano-sized shells. (g) SEM, (h) TEM and (i) cycle stability and the inset shows the EIS of hollow microspheres before and after 1000 GCD cycles. Reproduced with permission from ref. 164. Copyright 2015 RSC Publications.

high mass loading is an essential requirement for the commercial application of electrodes. To overcome this problem, Kwak *et al.* developed a mesoporous structure with a BET surface area of 141 $m^2\ g^{-1}$ and high mass loading ($\sim$9.7 mg cm^{-2}). The SEM investigations revealed that thorn-like nanoneedles were formed on the nanoflower, which appear to have grown on top of each carbon fiber. Despite high mass loading, Co_3O_4 on a carbon fiber paper (CF) substrate resulted in a high areal capacitance of about 1.35 F cm^{-2} at 1 mV s^{-1} scan rate. This nanostructured electrode retained almost 100% capacitance after 2500 cycles.[166] Vertically grown Co_3O_4 porous acicular nanorod arrays resulted in the presence of optimized NH_4F concentration. CV analysis showed that as the scan rate increases, the anodic and cathodic peaks shift toward positive and negative potentials, respectively, along with slight deformation in the curve noticed at higher potentials due to the increased polarization phenomenon. Further, Jiang *et al.* developed an ASC symmetrical device based on the synthesized electrode, which displayed good electrochemical stability (98.8%) after 5000 cycles. When the specific energy of the device decreases from 48.63 to 19 W h kg^{-1}, the corresponding specific power increases from 600 to 6000 W kg^{-1}.[167]

Another strategy used to augment the electronic conductivity of Co_3O_4 is to develop its thin layer on the surface of a porous and electrically conducting substrate. Nickel foam as a substrate provides excellent mass transport properties due to the availability of a large surface area and helps in the development of a highly porous hierarchical architecture.[168] Aadil *et al.* deposited urchin-like Co_3O_4 nanoarchitecture on nickel foam (refer to Fig. 14(a)) with a BET-specific surface area (BET_{SSA}) of about 165 $m^2\ g^{-1}$. The nanoarchitecture contains two types of micropores with a diameter of 22 nm and 12 nm, as shown in Fig. 14(b). The CV profile of pristine nickel foam as shown in Fig. 14(d) at various scan rates provides information about two pairs of oxidation/reduction bumps (B_1/B_4 and B_2/B_3) indicating its pseudocapacitance behavior. Fig. 14(e) shows a negligible change in the area under the CV profile after 5000 cycles, demonstrating the excellent cycle stability of the electrode. For the initial 1000 cycles, the synthesized electrode achieved 102.2% capacitance retention and after the subsequent 5000 cycles, it maintained 95.7% of its initial capacitance (Fig. 14(f)). The excellent cycle stability and rate capability of the synthesized electrode emanated from the hierarchical and highly porous structure, as this structure acts as an ion buffering reservoir, reduces structural damage due to volume changes during ion insertion/extraction processes, facilitates mass charge transport, and increases the electrolyte–electrode contact area.[143]

Hybrid nanostructures with the combination of 0D, 1D, 2D, and 3D structures are even more beneficial for excellent electrochemical performance. The development of such hybrid nanostructures promotes synergistic behavior and sophisticated properties of the host electrode by overcoming drawbacks associated with individual structural features. The subsequent study showed that nanosheets present themselves as an efficient template for the growth of hierarchical nanowire arrays and help to minimize structure or phase loss with excellent morphology and phase stability.

Yang and colleagues successfully synthesized hierarchical nanowires with an average diameter of 50–100 nm and a length

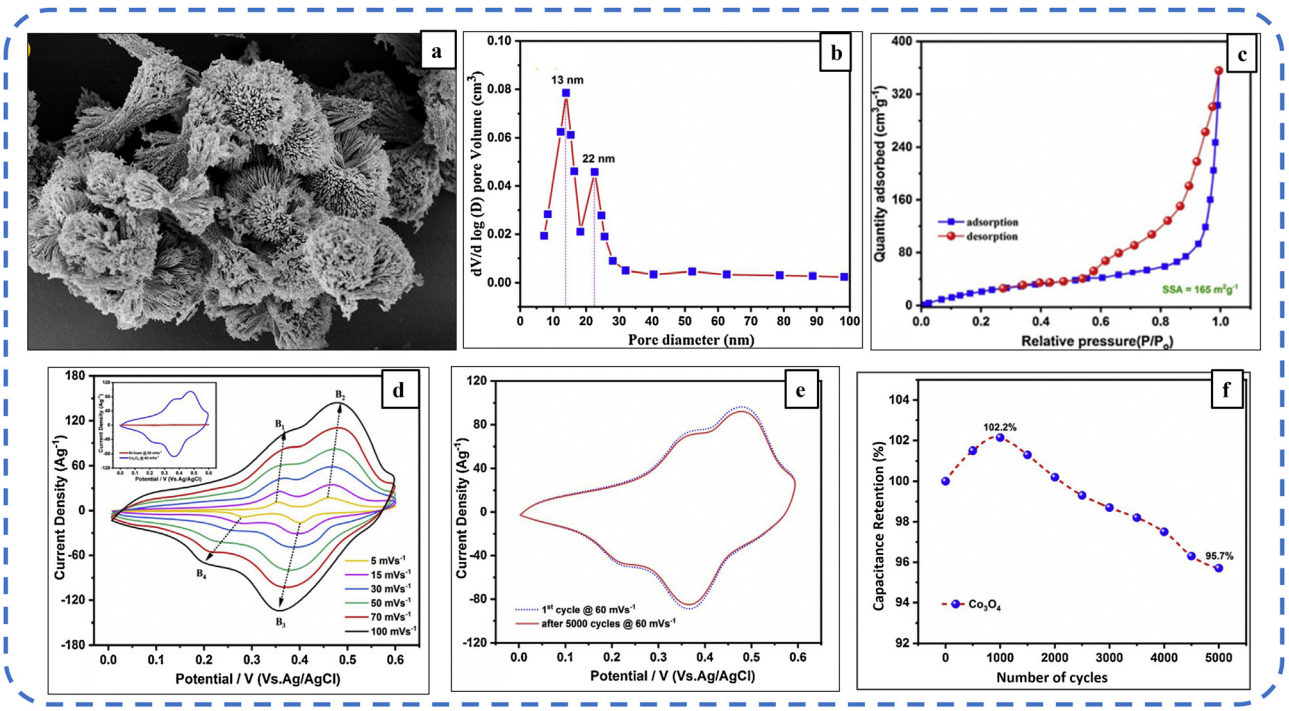

Fig. 14 (a) FESEM image displaying the urchin-like nanoarchitecture. (b) N_2 adsorption/desorption isotherms. (c) Pore size distribution. (d) CV profile at different scan rates. (e) CV profiles at the 1st cycle and after 5000th cycles. (f) Specific capacitance retention of the synthesized Co_3O_4 electrode. Reproduced with permission from ref. 143. Copyright 2020 Elsevier.

of 0.5–1 mm on a uniformly grown nanosheet array. Each nanosheet is firmly attached to the substrate to ensure the active participation of each nanosheet in the electrochemical reactions. The space between adjacent nanowires is beneficial for easy electrolyte diffusion into the internal region of the electrode. The as-synthesized Co_3O_4 nanosheets at the nanowire array achieved an areal capacitance of about 5.44 F cm^{-2} (715 F g^{-1}) at 5 mA cm^{-2} current density and retained 100% capacitance even after 1000 cycles. Here NH_4F also played an important role in achieving effective mass loading and tight adhesion of the material on the Ni-foam substrate.[168] Some studies have shown that the 3D structure resolves the conflict between the mass loading of electrochemically active material and its usage efficiency. But then, with reasonable mass loading, the 3D architecture of a 2D long-range (~5 μm) and thin (~10 nm) nanosheet array with desirable morphology and size was developed by Yang *et al.* *via* a two-step hydrothermal approach. Here the 2D long-range structure assisted fast redox reactions by providing continuous pathways for charge transfer. The smaller thickness provided a large contact surface area between the electrode and the electrolyte and facilitated the efficient use of active electrodes for the diffusion of ions. As the penetration depth of the KOH electrolyte is approximately 20 nm, it can use most of the area of a thin film (with 10 nm thickness).[169] Without the use of any template or complex process, Liao *et al.* reported the growth of 2D Co_3O_4 nanosheets into 3D hierarchical microspheres. The flower-like hierarchical microspheres (HMs) of pseudocapacitive Co_3O_4 electrodes with a large surface area of 115 m^2 g^{-1} were investigated. The cyclic voltammogram (CV) analysis in a 3 M KOH solution revealed a C_s of 541.9 F g^{-1} at a scan rate of 5 mV s^{-1}.[138]

A unique ultrathin nanosheet array structure consisting of well-aligned uniform long-range (5 mm in length) and thin (10 nm in thickness) nanosheets with reasonable mass loading was developed *via* a double hypothermal approach. Hexagonal β-$Co(OH)_2$ nanosheet arrays formed after the first hydrothermal reaction were again treated with excess Co^{2+} and a base such as urea (NS-U) or hexamethylenetetramine (HMT) (NS-H). SEM images of both NS-U and NS-H are depicted in Fig. 15(a, b). The two lattice sites of 0.23 nm and 0.29 nm observed in HRTEM (Fig. 15(c)) investigations correspond to the $(2\bar{2}2)$ and (220) planes of Co_3O_4. The narrow redox peaks manifest fast redox reactions, which are noticed as shown in Fig. 15(d) for the NS-H sample. The Co_3O_4 nanosheet array prepared by HMT treatment (NS-H) exhibited a C_s of 1782 F g^{-1} at a current density of 1.8 A g^{-1}. This mesoporous structure displayed a higher BET_{SSA} of about 211 m^2 g^{-1} compared to the NS-U sample. Further, an asymmetric supercapacitor device was designed with NS-H as a positive electrode and activated carbon as a negative electrode. Moreover, the device displayed a C_s of 108 F g^{-1} and a high specific energy of 134 W h Kg^{-1} at a specific power of 1111 W kg^{-1}. The excellent electrochemical performance of the material is attributed to the 3D mesoporous (pore size 7.65 nm) architecture consisting of 2D ultrathin nanosheets grown vertically on a nickel substrate and the dual hydrothermal approach used to develop this mesoporous structure.[12]

It is worth revealing that the use of a surfactant is also essential, as it can assist in forming a more layered, porous architecture, without agglomeration. The succeeding examples illustrate that surfactant-mediated synthesis of Co_3O_4 facilitates the development of varied morphologies. Yang *et al.* studied the effect of the precipitating agent, surfactant, solvent, pH value, and amount of oxidant on the morphology and structure of Co_3O_4. The investigation showed that the molar ratio of H_2O_2 and Co^{2+} (>2.5 : 1.0) assists in the formation of the spinel crystal structure of Co_3O_4.[170] Subsequently,

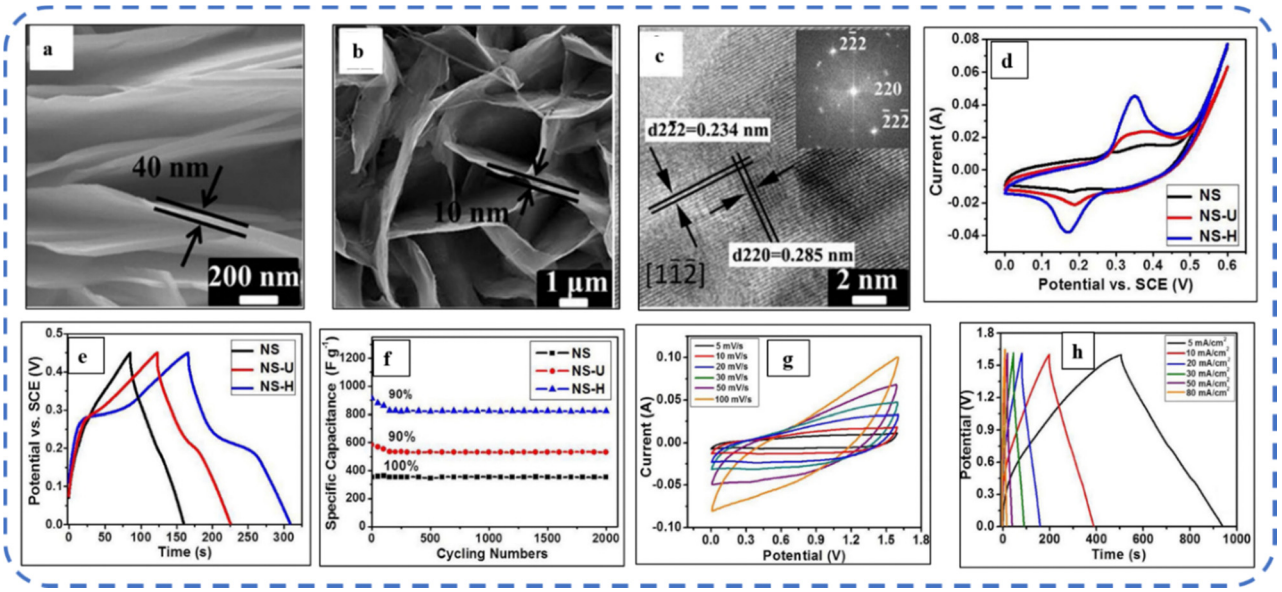

Fig. 15 (a) SEM images of the NS-U electrode. (b) and (c) SEM and HRTEM of the NS-H electrode. (d) CV, (e) GCD and (f) cycle stability of as-synthesized NS, NS-U and NS-H electrodes. (g) CV and (h) GCD of the synthesized asymmetric device based on NS-H and activated carbon as positive and negative electrodes, respectively. Reproduced with permission from ref. 12. Copyright 2013 Nature Publications.

Wang *et al*. used the Triton X-100 surfactant for the synthesis of the Co_3O_4 electrode for energy storage with nanowire-flake morphology. Moreover, the asymmetric device attained a specific energy of 61.60 W h kg^{-1} at a specific power of 1440 W kg^{-1} and can provide power to run an air fan for about 2 min after being fully charged.[172]

Subsequently, Wei *et al*. fabricated self-supported 3D hetero-structured Co_3O_4 arrays on Ni foam with nanowires anchored on the nanoflakes (Fig. 16(a)). The resulting structure promotes more active sites and higher electrolyte ion diffusion. With remarkable pseudocapacitive properties, Co_3O_4 arrays attained a C_s of 2053.1 F g^{-1} and 87.6% capacitance retention after 3000 cycles at a current density of 10 mA cm^{-2} (Fig. 16(b)). Additionally, the hybrid supercapacitor based on the as-synthesized electrode as a positive electrode and N-rGO as a negative electrode showed excellent electrochemical performance. A schematic illustration of the hybrid supercapacitor device is shown in Fig. 16(c). The Nyquist plot of the device (as shown in Fig. 16(d)) intercepts the *x*-axis at 0.33, indicating the low equivalent series resistance (ESR) and 1.87 Ω as the charge transfer resistance. This hybrid device with a wide potential window (1.6 V) achieved a specific energy of 15.9 W h kg^{-1} at a high specific power of 4 kW kg^{-1} and retained 93.3% capacity even after 10 000 cycles (Fig. 16(e and f)), revealing excellent prospects in practical applications.[171]

Another parameter that is vital in the physicochemical characteristics of electrodes is electrolyte. Electrolyte compatibility with an electrode material, ion size, operating potential window, and operating temperature are essential factors that influence the performance of active electrodes. All these aspects depend on the choice of the electrolyte. Studies of aqueous electrolytes have shown that due to their small ion size, they can easily penetrate the small pores that originate in the electrodes and encounter a low ionic resistance. Nevertheless, in alkaline electrolytes, such as in KOH, Co_3O_4 results in a narrow potential window (~1.5 V) and as a consequence in low specific energy (<50 W h kg^{-1}) and poor cycle life. Also, sometimes, during electrochemical reactions, electrodes dissolve into electrolytes and this affects their performance. Various strategies have been employed to broaden the potential window. Among these strategies, the most widely used approach is the selection of an appropriate electrolyte or the addition of Co^{2+} cations into the electrolyte to stabilize the electrode material by overcoming its dissolution issue, which assists in broadening the potential window. The organic electrolytes can provide a wide operating potential window above 3 V and long cyclic stability. Subsequently, Padmanathan *et al*. inspected the energy storage performance of a hierarchical Co_3O_4 nanowire/nanoflower hybrid structure electrode in a tetraethylammonium tetrafluoroborate ($TEABF_4$) and propylene carbonate (PC) containing non-aqueous (organic) electrolyte. The high-resolution scanning electron microscope (HRSEM) images are summarized in Fig. 17(a and b) showing the well-constructed growth of the free-standing nanowire/nanoflower architecture of Co_3O_4 on the CF substrate. The report shows that the fabricated symmetric supercapacitor in 1 M $TEABF_4$ achieved a wider potential window of ~2.5 V and an excellent cycle stability of about 80% after 10 000 cycles (refer to Fig. 17(c)) which is much higher than that obtained in a 3 M KOH electrolyte (46% after 5000 cycles as shown in Fig. 17(d)).

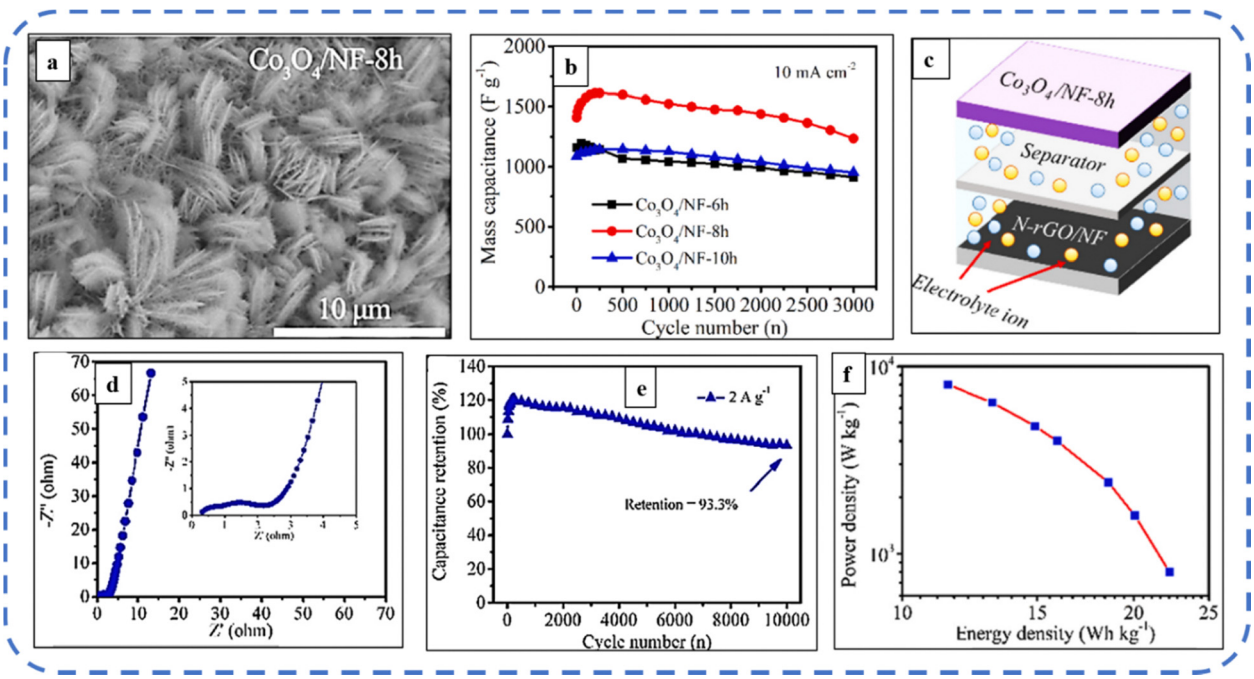

Fig. 16 (a) SEM image of the Co_3O_4 electrode grown after 8 h reaction time. (b) Cycle stability of samples developed at 6 h, 8 h and 10 h. (c) Schematic illustration of the developed asymmetric supercapacitor device. (d) Nyquist plots, (e) cycle stability and (f) Ragone plot of the Co_3O_4/NF-8 h//N-rGO/NF hybrid supercapacitor device. Reproduced with permission from ref. 171. Copyright 2021 Elsevier publications.

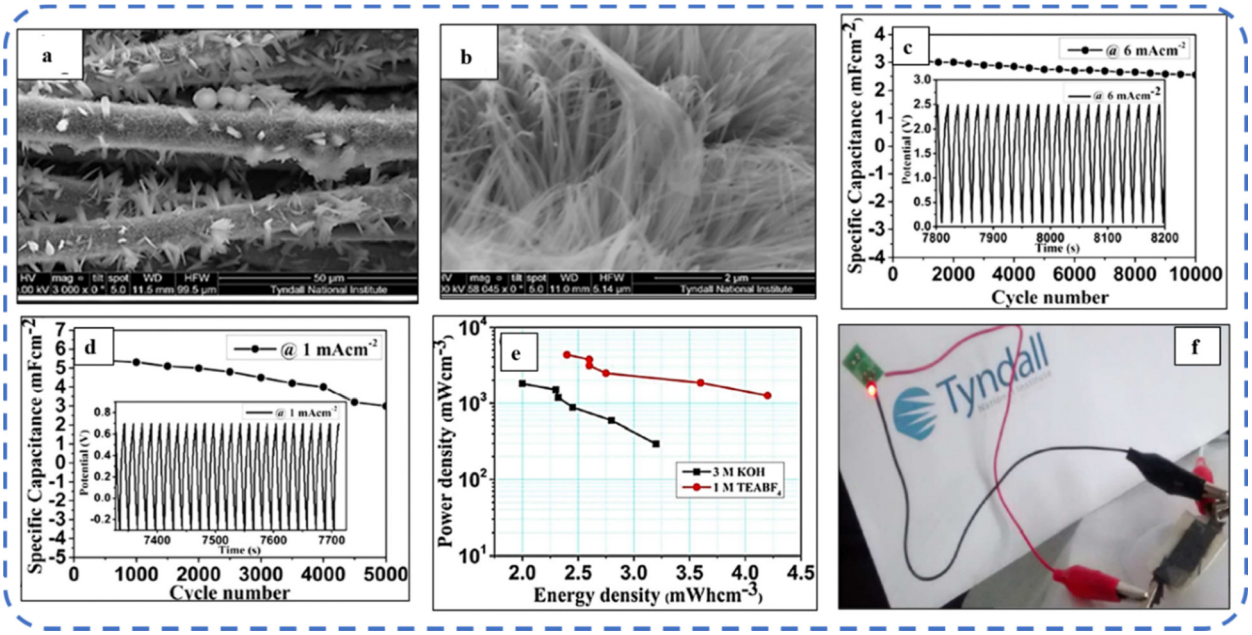

Fig. 17 (a) and (b) HRSEM images of the hierarchical Co_3O_4 nanowire/nanoflower hybrid structure. (c) and (d) Cycle stability of the symmetric supercapacitor in 1 M $TEABF_4$ and in a 3 M KOH electrolyte respectively. (e) Ragone plot and (f) photograph of a LED lighted by a charged supercapacitor in 1 M $TEABF_4$. Reproduced with permission from ref. 4. Copyright 2015 RSC Publications.

In Fig. 17(f), the glowing red LED indicates the practical use of the device.[4] Later, Chatterjee and coworkers studied the effect of a hydroquinone (HQ) containing Na_2SO_4 electrolyte on the CV profile of Co_3O_4 nanocrystals with urchin spine-like morphology. Investigations revealed that the HQ containing Na_2SO_4 electrolyte provides charge transfer resistance almost 40% less than that of the Na_2SO_4 electrolyte. The Co_3O_4 nanocrystals displayed a C_s of 2433 F g^{-1} at 2 mV s^{-1} scan rate in HQ containing Na_2SO_4, which is much greater than that in Na_2SO_4 and NaOH electrolytes.[172]

Consequently, a mesoporous Co_3O_4 electrode with flower-wire-nanoparticle tertiary hierarchical architecture was synthesized by Chen *et al.* *via* a hydrothermal route and subsequent sintering treatment. Further, an all-solid-state (ASC) asymmetric supercapacitor device based on the Co_3O_4 electrode as the positive electrode and AC as the negative electrode was designed. Moreover, the device in a PVA/KOH gel electrolyte achieved a specific energy of 16.25 W h kg^{-1} at a specific power of 7500 W kg^{-1}.[173] More recently, Xie *et al.* prepared various nanostructures by adjusting the reaction time. The nanoflowers with the mesoporous (pore size range 5–10 nm) petal architecture design of the Co_3O_4-based electrode exhibited enhanced electrochemical performance. They simultaneously used the training activation approach. In the ''activation process'', the C_s of the electrode was enhanced with the increase of cycle numbers during either the CV or galvanic charge–discharge (GCD) process. With this approach, the C_s of flower-structured Co_3O_4 electrodes was remarkably enhanced from 2.266 to 4.472 F cm^{-2} at a current density of 1 mA cm^{-2}. The expanded mesoporous architecture facilitated the penetration of electrolytes and assisted in superior cycle stability and rate capability.[174]

In summary, various porous morphologies resulting *via* the hydrothermal approach like nanoparticles, nanowires, nanosheets, and nanoflakes, different hollow structures like microspheres and nanotubes, and also hybrid morphologies such as nanosheet at nanowire arrays, nanowire/nanoflower hybrid structure, and nanoneedles assembled into a nanoflower are briefly described in this section. A summary of the precursors, various additives, reaction conditions, developed morphologies, and corresponding supercapacitive properties along with BET_{SSA} of hydrothermally grown Co_3O_4 for its supercapacitor application is tabulated in Table 2.

Solvothermal method

In particular, the solvothermal approach is quite useful for preparing various self-assembled architectures with the assistance of different solvents as reaction media. Statistical data for pristine Co_3O_4, synthesized through the solvothermal technique for supercapacitor applications, is presented in Table 3. The following section will provide a brief detail of this data. Solvents play a critical role in shaping the morphology of Co_3O_4 crystals by controlling the structural organization. Dielectric constants of the solvent have a considerable effect on the nucleation growth and viscosity is another parameter that might also impact the nucleation rate of the Co_3O_4 crystal. Solvents with large dielectric constants mainly promote 1D linear structural growth and those with small dielectric constants are more likely to produce 2D or 3D structures. Yang *et al.* systematically investigated the effect of various solvents on the morphology and electrochemical performance of Co_3O_4 nanocrystals. The results showed that the electrode displayed sheet-like, herbs-like, and net-like morphologies for ethanol,

Table 2 Data analysis of supercapacitor performance of hydrothermally grown Co_3O_4. Here C_a is the areal capacitance in F cm^{-2}, C_s is the specific capacitance in F g^{-1}, I_d is the current density in A g^{-1}, BET_{SSA} is the BET surface area, and SR is the scan rate in mV s^{-1}

Precursor	Substrate	Reaction temp. and time	Annealing temp. and time	Morphology	C_s (in F g^{-1}) or C_a (in F cm^{-2})@SR (in mV s^{-1}) or I_d (in mA cm^{-2} or A g^{-1})	Cycle stability or rate capability	BET_{SSA} (in m^2 g^{-1}) and pore volume (in cm^3 g^{-1})	Electrolyte	Potential window (V)	Ref.
$Co(NO_3)_2{\cdot}6H_2O$ + DW + $CO(NH_2)_2$ + ethanol	CFP	180 °C for 12 h	300 °C for 3 h	Nanowire/nanoflower hybrid structure	4.8 mF cm^{-2}@ 3 mA cm^{-2}	80% (1000)	60.3 m^2 g^{-1}	1 M $TEABF_4$ + PC	−0.5 to 0.7	4
$CoCl_2$ + DW + $CO(NH_2)_2$		105 °C for 6 h	300 °C for 3 h	Nanorods	280 F g^{-1} @5 mV s^{-1}		232 m^2 g^{-1}	2 M KOH	−0.25 to 0.55	119
$Co(NO_3)_2{\cdot}6H_2O$ + deionized water + PVA + diethylamine		180 °C for 24 h	300 °C for 3 h	Nanorods	1022 F g^{-1}@5 mV s^{-1}	88% (2000)		1 M KOH	0–0.5	126
$Co(NO_3)_2{\cdot}6H_2O$ + HMT + DW	Ni foam	120 °C for 6 h	300 °C for 3 h	Nanosheets	880 F g^{-1}@1 A g^{-1}		65 m^2 g^{-1}	1 M KOH	0 and 0.6	130
$CoSO_4{\cdot}7H_2O$ + glycerol + DW + urea		170 °C for 24 h	400 °C for 2 h	Nanowires	251 F g^{-1}@1 mV s^{-1}	98% (2000)		2 M KOH	0.1–0.6	131
$CoCl_2{\cdot}6H_2O$ + urea + NH_4F + deionized water	Ni foam	115 °C for 6 h	300 °C for 3 hours	Nanowires	1.92 F cm^{-2}@5 mA cm^{-2}	72.91% (30 mA cm^{-2})		2.0 M KOH	0–0.55	134
$Co(NO_3)_2$ + sodium nitrate + ammonia solution + DW	Si and Ni foam	120 °C for 12 h	250 °C for 1 h	Hollow nanowire arrays	599 F g^{-1}@2 A g^{-1}	73% (2–40 A g^{-1})		1 M KOH	0.1–0.6	135
$Co(NO_3)_2{\cdot}6H_2O$ + NH_4NO_3 + ammonia + H_2O	Ni sheet	90 °C for 14 h	80 °C for 12 h.	Nanoparticles	928 F g^{-1}@1.5 A g^{-1}	93% (2200)		2 M KOH	−0.2 to 0.4	136
$CoSO_4{\cdot}7H_2O$ + deionized water + guanidine hydrochloride + activated carbon		160 °C for 16 h	500 °C for 4 h	Hollow nanotubes	1006 F g^{-1} @1 A g^{-1}	91% (1000)	42 m^2 g^{-1}	2.0 M KOH	−0.4 to 0.65	137
$CoSO_4{\cdot}7H_2O$ + L-arginine + deionized water		100 °C for 24 h	300 °C for 4 h in air	Hierarchical microspheres	541.9 F g^{-1}@5 mV s^{-1}	89.5% (2000)	115 m^2 g^{-1}	3.0 M KOH	0–0.6	138
$Co(NO_3)_2$ + NH_4F + $CO(NH_2)_2$	Ni foam	120 °C for 9 h	350 °C for 2 h	Nanowire array	754 F g^{-1}@2 A g^{-1}			2 M KOH		140
$Co(NO_3)_2{\cdot}6H_2O$ + NH_4F + $CO(NH_2)_2$	CFP	120 °C for 6 h	400 °C for 3 h	Nanowires	3290 F g^{-1}@5 mV s^{-1}	93.5% (2000)		3 M KOH	−0.2 to 0.7	141
$Co(NO_3)_2{\cdot}6H_2O$ + CH_4N_2O	Ni foam	120 °C	450 °C for 4 h	Urchin-like	848 F g^{-1}@1 A g^{-1}	95.7% (5000)	165 m^2 g^{-1}	3 M KOH	0–0.6	143
$Co(NO_3)_2{\cdot}6H_2O$ + $CO(NH_2)_2$ + deionized water		180 °C for 10 h	350 °C for 3.5 h	Brush like	764 F g^{-1}@5 mV s^{-1}	64% (5000)	50.10 m^2 g^{-1}	3 M KOH	0.0–0.6	144
$Co(NO_3)_2{\cdot}6H_2O$ + $CO(NH_2)_2$ + deionized water	Ni foam	180 °C for 6 h		Nanowires	1140 F g^{-1}@1 Ag^{-1}	93.3% (5000)		3 M KOH	0.0–0.5	145
$Co(NO_3)_2{\cdot}6H_2O$ + $CO(NH_2)_2$ + Triton X-100		120 °C for 24 h	300 °C	Rectangular 2D flakes	548 F g^{-1}@8 Ag^{-1}	98.5% (2000)	97 m^2 g^{-1} and 0.2 cm^3 g^{-1}	1 M KOH	0.2–0.5	147
$Co(NO_3)_2{\cdot}6H_2O$ + NH_4F + $CO(NH_2)_2$ + H_2O	Ni foam	110 °C for 12 h	400 °C for 3 h	Nanosheets	2194 F g^{-1}@1 A g^{-1}	93.1% (5000)	102 m^2 g^{-1}	1 M KOH	−0.2 to 0.6	148
$Co(NO_3)_2{\cdot}6H_2O$ + NH_4F + H_2O + $CO(NH_2)_2$	Ni foam	140 °C for 9 h	400 °C for 3 h	Conch-like nanostructure arrays	4.11 F cm^{-2}@5-mA cm^{-2}	93% (5000)	82.5 m^2 g^{-1}	2 M NaOH	−0.1 to 0.6	149
$Co(NO_3)_2{\cdot}6H_2O$ + deionized water + ethanol + HMT	Nickel foam	90 °C for 12 h	320 °C for 2 h	Nanosheets	610 mF cm^{-}@1 mA cm^{-2}	94.5% after 3000	91.482 m^2 g^{-1}	2 M NaOH	0.7–0.7	150
$Co(NO_3)_2{\cdot}6H_2O$ + HMT + water + anhydrous ethanol	Ni foam	90 °C for 3 h	400 °C for 3 h	Hexagonal nanosheets	327.3 F g^{-1}@0.5 A g^{-1}	96.07% (10 000)	61.8 m^2 g^{-1}	6 M KOH	0–0.6	151
$Co(NO_3)_2{\cdot}6H_2O$ + HMT + deionized water + NH_4OH		180 °C for 6 h	550 °C for 3 h	Nanosheet	1455.64 F g^{-1}@ 1.0 A g^{-1}	94.10% (2000)		3 M KOH	0–0.6	153
$CoCl_2{\cdot}6H_2O$ + urea + Milli-Q water + polypropylene	Nickel foam	50–90 °C for 1–24 h	170–300 °C for 4 h	Net-like	1090 F g^{-1}@10 mV s^{-1}			1 M NaOH	−0.2 to 0.5	154
$Co(NO_3)_2{\cdot}6H_2O$ + SDS + distilled water		120 °C for 24 h	300 °C for 3 h	Nest-like	404 F g^{-1}@2 A g^{-1}	80% (1000)	66 m^2 g^{-1} and 0.31 cm^3 g^{-1}	1 M KOH	0.0–0.65	156

Table 2 (*continued*)

Precursor	Substrate	Reaction temp. and time	Annealing temp. and time	Morphology	C_s (in F g^{-1}) or C_a (in F cm^{-2})@SR (in mV s^{-1}) or I_d (in mA cm^{-2} or A g^{-1})	Cycle stability or rate capability	BET_{SSA} (in m^2 g^{-1}) and pore volume (in cm^3 g^{-1})	Electrolyte	Potential window (V)	Ref.
$Co(NO_3)_2{\cdot}6H_2O$ + NH_4F + CTAB + triple DW	Ni foam	120 °C for 12 h	350 °C for 2 h	Flake-like	1820 F g^{-1}@1 A g^{-1}		66 m^2 g^{-1} and 0.16 cm^3 g^{-1}	2 M KOH	0.0–0.6	157
$Co(NO_3)_2{\cdot}6H_2O$ + deionized water + ammonia solution	Nickel foam	120 °C for 10 h	300 °C for 2 h	Gem shape	1060.0 F g^{-1}@1 A g^{-1}	99.6% (5000)	117.7 m^2 g^{-1}	6 M KOH	0–0.6	159
$Co(NO_3)_2$ + C_2H_5OH + H_2O + $CO(NH_2)_2$	Ni foam	90 °C for 10 h	300 °C for 3 h	Honeycomb structure	2509.4 F g^{-1}@1 A g^{-1}	74% (1000)		3 M KOH	−0.5 to 0.65	160
$Co(NO_3)_2$ + $NaNO_3$ + deionized water + $NH_3{\cdot}H_2O$ + H_2O_2		100 °C for 12 h		Microspheres	850 F g^{-1}@1 A g^{-1}	90.8% (1000)		2.0 M KOH	−0.5 to 0.55	162
$Co(NO_3)_2$ + $NaNO_3$ + deionized water + $NH_3{\cdot}H_2O$ + H_2O_2		140 °C for 12 h		Nanofilms	1400 F g^{-1}@1 A g^{-1}	97% (1500)		2.0 M KOH	0.4–0.8	163
$Co(NO_3)_2$ + $NaNO_3$ + deionized water + $NH_3{\cdot}H_2O$ + H_2O_2		120 °C for 12 h		Hollow microspheres	1227 F g^{-1}@1 A g^{-1}	97.5% (1000)		2.0 M KOH	−0.25 to 0.55	164
$Co(NO_3)_2{\cdot}6H_2O$ + NH_4F + $CO(NH_2)_2$	CFP	120 °C for 5 h	400 °C for 4 h	Thorn-like nanoneedles assembled into a nanoflower	1.35 F cm^{-2}@1 mV s^{-1}	Almost 100% (2500)	141 m^2 g^{-1} and 0.18 cm^3 g^{-1}	1 M KOH	0–0.6	166
$Co(NO_3)_2{\cdot}6H_2O$ + deionized water + NH_4F + $CO(NH_2)_2$	Ni foam	130 °C for 5 h	400 °C for 2 h	Porous acicular nanorods	1486 F g^{-1}@1 A g^{-1}	98.8% (1000)	59.4 m^2 g^{-1}	2 M KOH	0.0–0.45	167
$Co(NO_3)_2{\cdot}6H_2O$ + NH_4F + $CO(NH_2)_2$	Nickel foam	100 °C for 9 h	523 K for 3 h	Nanosheet at nanowire arrays	715 F g^{-1}@5 mA cm^{-2}	100% (1000)		1 M KOH	0–0.44	168
$Co(NO_3)_2{\cdot}6H_2O$ + NH_4F + HMT	Ni foam	120 °C for 12 h	250 °C for 3 h	Nanosheet arrays	1782 F g^{-1}@1.8 A g^{-1}	>90% (2000)	211 m^2 g^{-1}	2 M KOH	0–0.6	12
$Co(NO_3)_2{\cdot}6H_2O$ + Triton X-100	Ni foam	120 °C for 4 h	350 °C for 2 h	Nanowire-flake	1230.65 F g^{-1}@1 A g^{-1}	95.8% (5000)		6 M KOH	0–0.5	175
$Co(NO_3)_2{\cdot}6H_2O$ + $CO(NH_2)_2$ + deionized water	Ni foam	120 °C for 8 h	350 °C for 2 h	Nanoarray	2053.1 F g^{-1} or 6.16 F cm^{-2}@1 A g^{-1}	87.6% (3000)		6 M KOH	0–0.5	171
$Co(NO_3)_2{\cdot}6H_2O$ + Triton X-100 + urea		120 °C for 12 h	300 °C for 2 h	Urchin spine shaped	2433 F g^{-1}@2 mV s^{-1}			1 M Na_2SO_4 (with Hq)	−0.3 to 0.8	172
$Co(NO_3)_2{\cdot}6H_2O$ + $CO(NH_2)_2$	Ni foam	120 °C for 8 h	350 °C for 2 h	Nanowires	2.266 F g^{-1}@1 mA cm^{-2}	84.6% (5000)		6 M KOH	0–0.7	174
$CoN_6Na_3O_{12}$ + deionized water + absolute ethanol + polyvinyl pyrrolidone		150 °C for 12 h	500 °C for 2 h	Nanocubes	∼430.6 F g^{-1}@10-mV s^{-1}	∼85% (1000)	61.5 m^2 g^{-1} and 0.074 cm^3 g^{-1}	6 M KOH	−0.4 to 1	176
$Co(NO_3)_2$ + urea + deionized water	Ni foam	95 °C for 8 h	400 °C for 2 h	Nanowires	880.2 F g^{-1} @1 A g^{-1} (122.3 mA h g^{-1}@1 A g^{-1})	100% (3000)	26.04 m^2 g^{-1}	2 M KOH	0–0.6	177

Table 3 Data analysis of supercapacitor performance of solvothermally grown Co^3O^4. Here C_a is the areal capacitance in F cm^{-2}, C_s is the specific capacitance in F g^{-1}, I_d is the current density in A g^{-1}, BET_{SSA} is the BET surface area, and SR is the scan rate in mV s^{-1}

Precursor	Substrate	Reaction temp. and time	Annealing temp. and time	Morphology	C_s (in F g^{-1}) or C_a (in F cm^{-2})@SR (in mV s^{-1}) or I_d (in mA cm^{-2} or A g^{-1})	Cycle stability or rate capability	BET_{SSA} (in m^2 g^{-1}) and pore volume (in cm^3 g^{-1})	Electrolyte	Potential window	Ref.
$Co(NO_3)_2{\cdot}6H_2O$ + $(CH_2OH)_2$+ $CO(NH_2)_2$+ deionized water		160 °C for 20 h	400 °C for 2 h	Porous nanobooks	590 F g^{-1}@0.5 A g^{-1}	97.4% (1000)	19.45 m^2 g^{-1} and 0.11 cm^3 g^{-1}	6 M KOH	−0.1–0.45 V	116
$Co(NO_3)_2{\cdot}6H_2O$ + CTAB + glycerol	Nickel foam	180 °C for 24 h	250 °C for 4 h	Nanonet	1063 F g^{-1}@10-mA cm^{-2}	90.8% (1000)		6 M KOH	0 to 0.6 V	178
$Co(Ac)_2{\cdot}4H_2O$ + ethanol + ammonia	Ni foam	150 °C for 3 h		Nanocubes	1913 F g^{-1}@8 A g^{-1}	70% (650)	74.80 m^2 g^{-1}	0.5 M KOH	0.1–0.7 V	179
$Co(NO_3)_2{\cdot}6H_2O$ + absolute methanol + CTAB + DW	Ni-foam	120 °C for 8 h	250 °C for 4 h in air	Nanoflower	1936.7 F g^{-1}@0.2 A g^{-1}	78.2% (1000)		6.0M KOH	0.4–0.45	180
$Co(NO_3)_2{\cdot}6H_2O$ + CTAB+ H_2O + absolute methanol	CFP	180 °C for 24 h	250 °C for 4 h	Nanowire	1525 F g^{-1}@1 A g^{-1}	∼91–94% (5000)	75.94 m^2 g^{-1}	KOH	0–0.8 V	181
$Co(Ac)_2{\cdot}4H_2O$ + NaOH + ethanol		220 °C for 20 h	300 °C for 3 h	Hexagonal platelet	476 F g^{-1}	82% (2000)	289 m^2 g^{-1}	2 M KOH	−0.4 to 0.4 V	182
$Co(NO_3)_2{\cdot}6H_2O$ + $CO(NH_2)_2$ + DW	Ni foam	120 °C for 4 h	250 °C for 4 h	Nanowires	493 F g^{-1}@0.5 A g^{-1}			2 M KOH	0–0.6 V	183
$CoCl_2{\cdot}6H_2O$ + ethanol + DW + NaOH	–	200 °C for 4 h	–	Hollow octahedra	192 F g^{-1}@2 A g^{-1}	3000 cycles		2 M KOH	0 to 0.6 V	184
$Co(NO_3)_2{\cdot}6H_2O$ + $CO(NH_2)_2$ + ethanol	Ni-foam	150 °C for 15 h	350 °C for 2 h	Nanowires	1600 F g^{-1}@10 A g^{-1}	Almost 100% (5000)		1 M KOH	0–0.7 V	185
$CoCl_2{\cdot}6H_2O$ + nitrilotriacetic acid + isopropyl alcohol + DW	Ni-foam	180 °C for 24 h	300 °C for 0.5 h	Porous nanowires	2815.7 F g^{-1}@2 A g^{-1}	88.8% (1100)		2 M KOH	0 to 0.55 V	186
Cobalt(II) acetate tetrahydrate + *N*,*N*-dimethylformamide + DW+ hydrazine monohydrate	Ni-foam	190 °C for 12 h	300 °C for 3 h	Nanohorn	2751 F g^{-1}@1 A g^{-1}	46.8% rate capability		6 M KOH	0–0.6 V	187
Cobalt(II) acetylacetonate + cobalt(III) acetylacetonate+ ethanol + DW+ H_2O_2 + NaOH		140 °C for 8 h	500 °C for 5 h	Nanoparticles	778 F g^{-1}@5 mV s^{-1}			KOH	−0.3 to 0.7 V	188

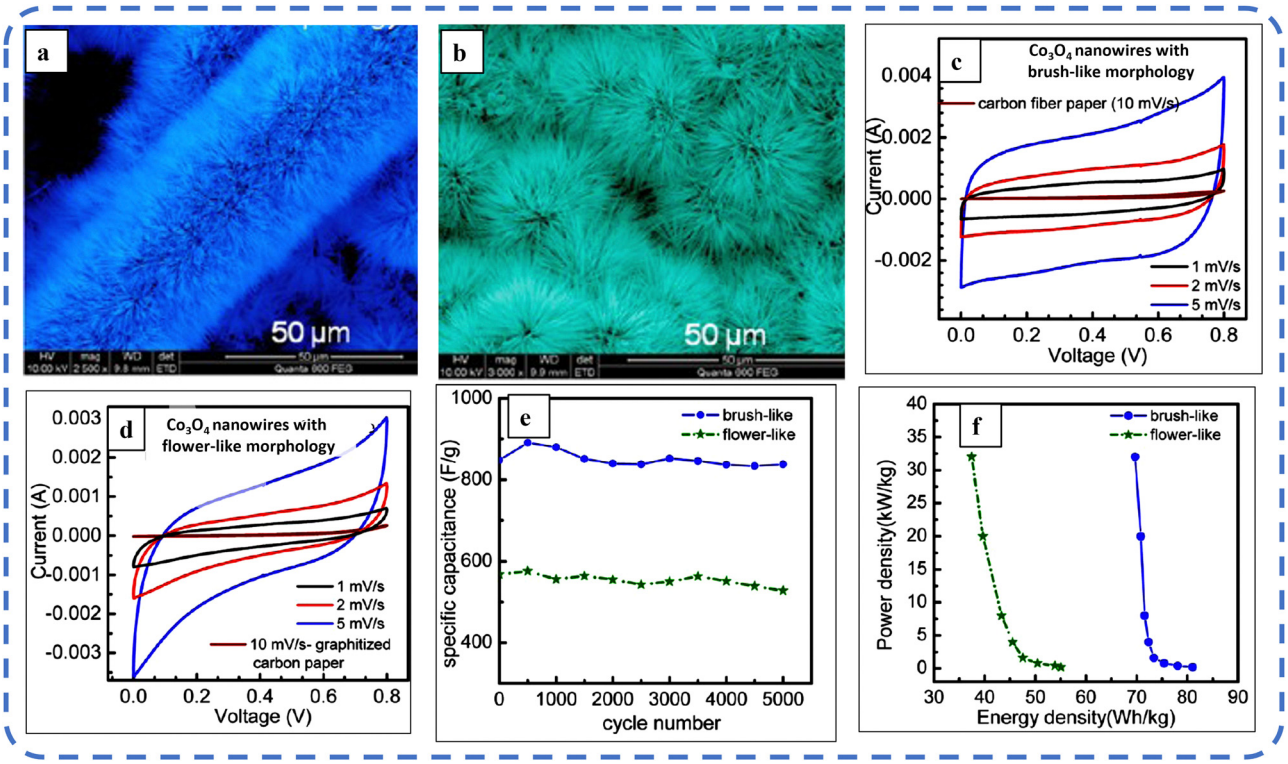

Fig. 18 (a) and (b) SEM images of Co_3O_4-b and Co_3O_4-f nanowires. (c) and (d) CV, (e) cycle stability and (f) Ragone plot of brush-like (Co_3O_4-b) and flower like (Co_3O_4-f) nanowires. Reproduced with permission from ref. 181. Copyright 2012 ACS Publications.

ethylene glycol (EG), and glycerol (GR) respectively (as the dielectric constant of GR > EG > ethanol). The Co_3O_4 electrode with a nanonet-like structure grown in the presence of glycerol and CTAB offered the highest C_s of 1063 F g^{-1} at 10 mA cm^{-2} current density.[178] Then, in the presence of ethanol, Pal and co-workers developed Co_3O_4 nanocubes, which achieved a significant C_s of about 1913 F g^{-1} at a current density of 8 A g^{-1}.

Subsequently, Rakhi *et al.* reported the effect of variation of the current collector on the structural morphology and physicochemical properties. Surfactant (CTAB)-assisted microstructures were grown on CF paper and planar graphitized CF displayed the brush-like (Co_3O_4-b) (Fig. 18(a)) and flower-like (Co_3O_4-f) (Fig. 18(b)) nanowires, respectively. Fig. 18(c and d) depicts the CV of both the nanostructures at different scan rates, revealing that the specific capacitance decreases as the scan rate increases. At high scan rates, ion diffusion is very slow and merely the outer surface of the electrode can be used for charge storage. Ragone plots of two symmetric supercapacitor (SC) devices based on Co_3O_4-b and Co_3O_4-f are shown in Fig. 18(f). The SC device based on the Co_3O_4-b electrode displayed a specific power of 32 kW kg^{-1} at a specific energy of 69.7 W h kg^{-1}. The Co_3O_4-b electrode achieved a C_s of 1525 F g^{-1} at a current density of 1 A g^{-1}.[181] Porous Co_3O_4 nanowires as a promising candidate with enhanced electrochemical performance for pseudocapacitor application were successfully synthesized using nitrilotriacetic acid (NA) as a chelating agent. Impressively, despite the high scan rate, electrolytes can penetrate the porous Co_3O_4 nanowire matrix very quickly and the short diffusion distance of OH^- accelerates the faradaic reactions and displays an outstanding performance of the material. The as-synthesized electrode achieved a C_s of 2853 F g^{-1} at a current density of 1 A g^{-1} and displayed outstanding rate capability (765 F g^{-1} at 20 A g^{-1}).[186]

Then the variation in morphology from 0D to 2D structures and its correlation with the pseudocapacitive performance of Co_3O_4 nanostructures were analyzed by Deori *et al.* They synthesized hexagonal platelets (2D) with 3–4 μm diameter (Fig. 19(a)) and spherical (diameter 30–35 nm) (0D) (Fig. 19(b)) morphologies at optimized reaction time. The 2D hexagonal platelet morphology with a very high BET_{SSA} of about 289 m^2 g^{-1} achieved good pseudocapacitance behavior by allowing the electrolytic ions (K^+) to use the maximum surface area of the material. The synthesized symmetric device is based on hexagonal platelet Co_3O_4 electrodes (Co_3O_4/KOH/Co_3O_4). The dominating pseudocapacitive contribution can be easily understood with GCD and CV profiles of the cell (Fig. 19(e and f)). The as-synthesized device exhibited excellent electrochemical properties with high cycling stability (retains almost 82% after 2000 cycles) and specific energy of 42.3 W h kg^{-1} at the corresponding 1.56 kW kg^{-1} specific power at a current density of 0.5 A g^{-1} (Fig. 19(h)).[182]

Later Chen *et al.* demonstrated a stepwise splitting growth mechanism for the formation of porous 3D nanobooks, which is controlled by reaction time and urea concentration. During the stepwise splitting growth process, they observed that the 1D $Co(CO_3)_{0.5}(OH)\cdot 0.11H_2O$ precursor nanorods transitioned to 2D

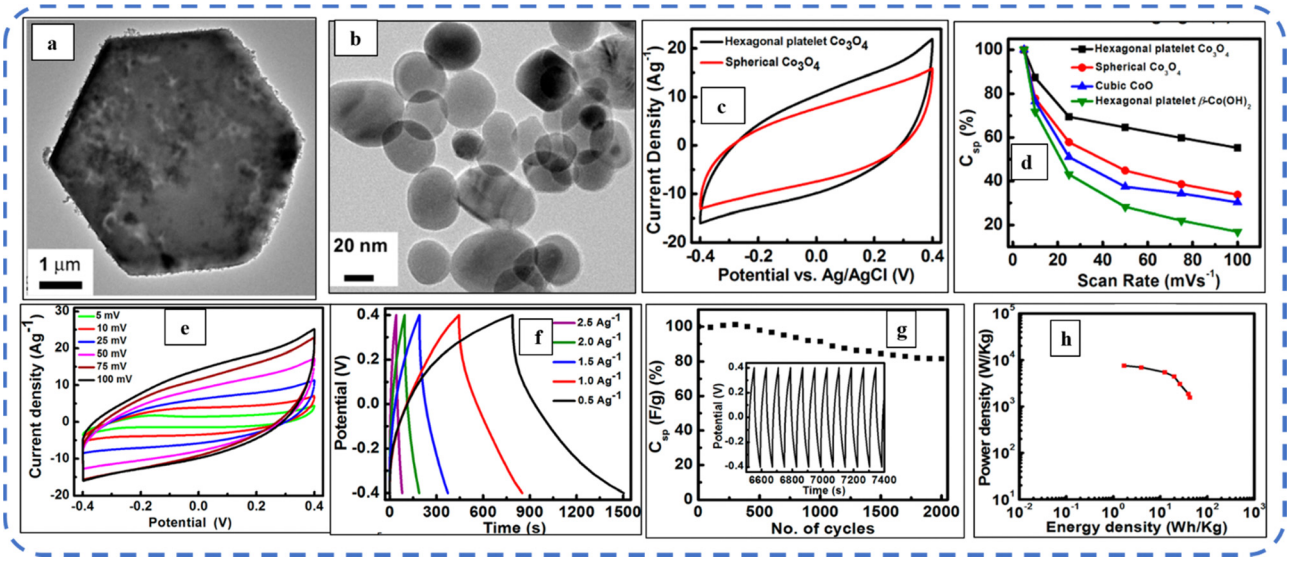

Fig. 19 Low magnification TEM images of (a) hexagonal platelet and (b) spherical morphology of Co_3O_4 nanoparticles. (c) Comparative CV of both resulted morphologies. (d) Variation of specific capacitance with scan rate. (e) CV, (f) GCD, (g) cycling stability and (h) Ragone plot of two electrode systems based on the Co_3O_4 electrode having the hexagonal platelet morphology. Reproduced with permission from ref. 182. Copyright 2015 ACS publications.

nanoplates after a long reaction time and then to a 3D hierarchical book-like architecture and finally after annealing it got transformed into porous and hierarchical Co_3O_4 nanobook-like nanoarchitectures.[75] Qing *et al.* successfully tuned the size and morphology of the Co_3O_4 electrode by optimizing the post-calcination temperature. The green-colored (indication of carbonate nitrate hydroxide hydrate formation) Ni-foam as shown in Fig. 20(a) turns black, signifying the formation of Co_3O_4. The nanoflower Co_3O_4 electrode (Fig. 20(b and c)) that resulted after 4 h calcination at 250 °C achieved an excellent C_s (1936.7 F g^{-1}), which is much greater than that obtained after 14 h calcination (1309.4 F g^{-1}), and retained 78.2% capacitance after 1000 cycles at a current density of 3 A g^{-1}.[180] Subsequently, Cao *et al.* reported the synthesis of hollow Co_3O_4 octahedra (SEM and TEM images are shown in Fig. 20(f and g) respectively) for the first time without using any template, by varying the reaction time. The Nyquist plot (Fig. 20(i)) for the as-synthesized hollow octahedron exhibited a lower ESR (3.6 Ω) than that of the nanocube electrode (with the same reaction conditions by simply changing the starting precursor from $CoCl_2{\cdot}6H_2O$ to

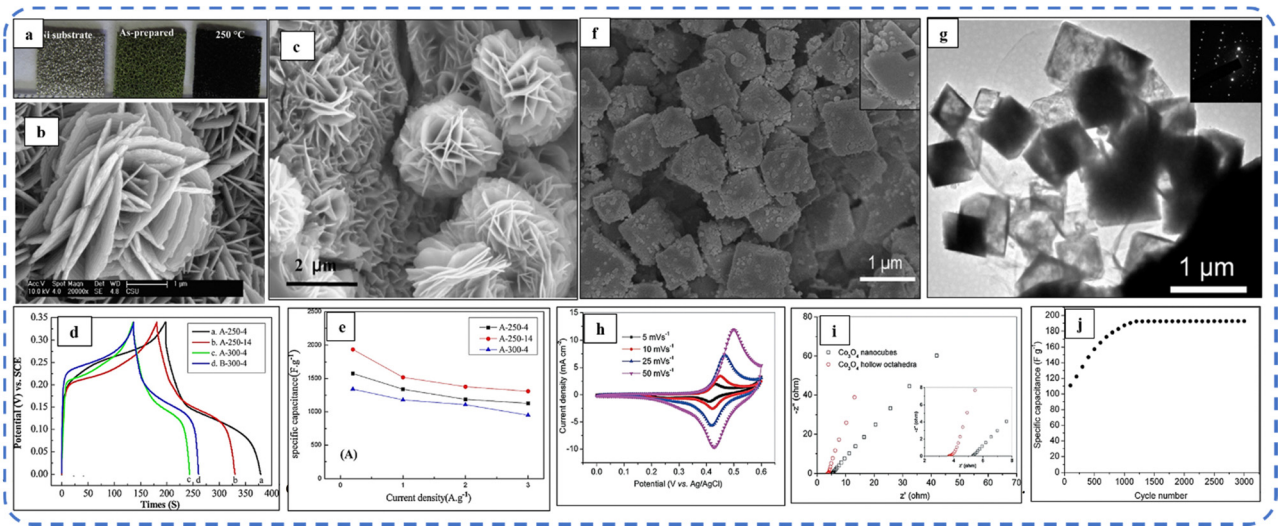

Fig. 20 (a) Photographs of Ni foam during the deposition process. High magnification (b) SEM and (c) TEM images of sample A-250-4 with nanoflower morphology. (d) Comparative GCD of all-synthesized samples under various reaction conditions. (e) Current density *vs* specific capacitance for as-synthesized samples. Reproduced with permission from ref. 180. Copyright 2011 Elsevier publications. High magnification (f) SEM and (g) TEM images. (h) CV at various scan rates. (i) EIS curves and (j) cycle stability of synthesized Co_3O_4 hollow octahedra. Reproduced with permission from ref. 184. Copyright 2017 RSC publications.

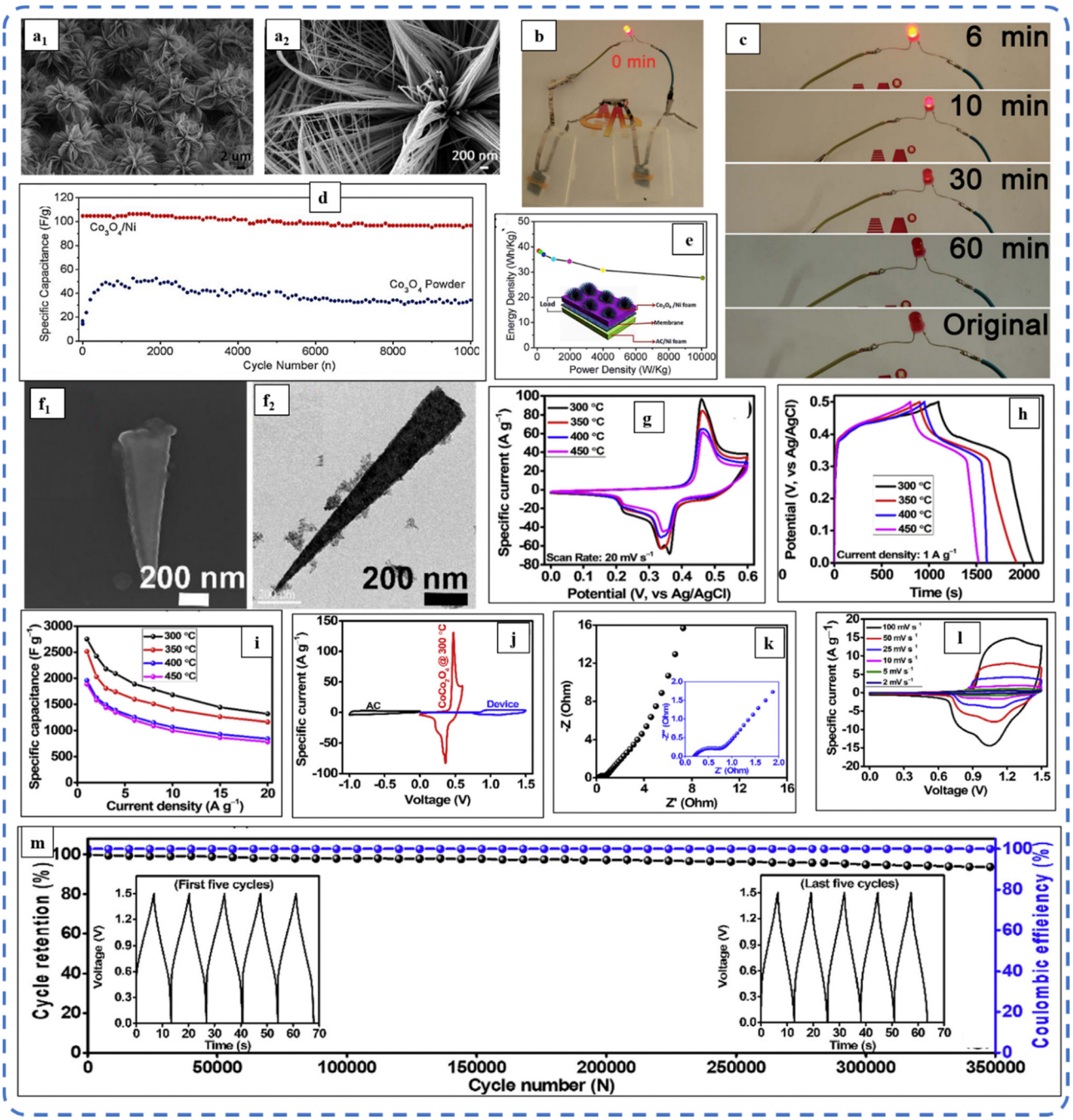

Fig. 21 (a_1) and (a_2) Low and high magnification SEM images of synthesized Co_3O_4. (b) and (d) Brightness of the LED at various times when the two Co_3O_4/Ni//AC asymmetric SC devices are connected in series. (d) Cycle stability and (e) Ragone plot of the synthesized asymmetric device. Reproduced with permission from ref. 185. Copyright 2017 RSC publications (f_1) and (f_2) HRSEM and TEM images of Co_3O_4 nanohorns. (g) CV, (h) GCD and (i) capacitance variation at various current densities of the synthesized Co_3O_4 electrode at different reaction temperatures. (j) CV curves of the AC, Co_3O_4@300 °C, and the developed HSC device. (k) Nyquist plot, (l) CV and (m) cycle stability of the as-developed HSC device. Reproduced with permission from ref. 187. Copyright 2018 Elsevier publications.

$Co(CH_3COO)_2{\cdot}4H_2O$)). The cycling performance shown in Fig. 20(j) reveals that electrolytes cannot easily penetrate the interior of the hollow octahedra; thus, the inner surface could not be fully used for some initial cycles. But with increasing cycles, the electrolyte gradually penetrated the interior of the hollow octahedra and rendered more active Co_3O_4 material.[184]

A high-current-density supercapacitor device based on hierarchical Co_3O_4 microflowers composed of nanowires (diameter of 50 nm) (SEM images are shown in Fig. 21(a1 and a2)) was successfully developed by Wang *et al.* The effect of cobalt salt concentration on morphology was examined and it was found that higher concentrations resulted in elongated nanorods with higher length/diameter (L/D) ratios. The synthesized

electrode achieved high C_s (1600 F g^{-1} at 10 A g^{-1}) and outstanding cycle stability (retains almost 100% after 5000 cycles). The abundant ion channels provided by the nanostructure and the electrical conductivity of nickel are the two main factors that assisted the higher electrochemical performance of the synthesized electrode. They further assembled the Co_3O_4/Ni//AC asymmetric supercapacitor device and evaluated its electrochemical performance. Two devices connected in series can supply power to an LED for about 1 min (Fig. 21(b and c)). As depicted in Fig. 21(d), the device retains almost 100% of its initial capacitance after 5000 GCD cycles at a high current density and with a high specific energy of 34 W h kg^{-1} at 1963 W kg^{-1} specific power (Fig. 21(f)). The superior performance was ascribed to the electronic conductivity of the Ni substrate and large ion channels provided by the 1D nanowire structure of the synthesized Co_3O_4 electrode.[185]

A similar asymmetric supercapacitor device designed by Pan *et al*. exhibited superior cycling stability by maintaining 90.4% of its initial capacitance even after 36 000 cycles.[189] As studied by Sivakumar *et al*., the calcination temperature affects the nanostructure and subsequently the electrochemical characteristics of the electrode. The horn-like Co_3O_4 nanostructures (HRSEM and TEM images are shown in Fig. 21(f1 and f2)) at a calcination temperature of 300 °C achieved the highest C_s ($\sim$2751 F g^{-1} at 1 A g^{-1}) compared to that obtained at 350 °C, 400 °C, and 450 °C. Shivakumar *et al*. developed a hybrid supercapacitor device (HSC) with as-synthesized Co_3O_4 (resulted at 300 °C) as the positive electrode and activated carbon (AC) as the negative electrode. Fig. 21(j) shows the CV curves of the AC (semi-rectangular shape), developed Co_3O_4, and fabricated HSC devices, demonstrating combined characteristics of faradaic and non-faradaic behavior. The HSC device with a very low ESR of about 0.19 Ω (Fig. 21(k)) retained 91.37% of its initial capacitance over 350 000 GCD cycles at 20 A g^{-1} current density (Fig. 21(m)). The unique nanohorn structure comprising well-interconnected and distributed particles having the ability to change volume during continuous charge–discharge cycles is the foremost cause behind the outstanding cyclic performance.[187] Afterwards, UmaSudharshini *et al*. also studied the effect of reaction temperature on the structural, morphological, optical, and electrochemical properties of the synthesized Co_3O_4 electrodes. Studies have shown that crystallite size increases with an increase in reaction temperature from 120 to 200 °C. Here at 140 °C, relatively the lowest reaction temperature reported to date, nanocrystallites as well as small crystallites are formed, yielding a more favorable performance. Above 200 °C, agglomeration occurs due to van der Waals force of attraction. The resulting Co_3O_4 nanoparticles (NPs) (with a mean size of 40 nm) with nanosheet morphology at 140 °C displayed a high C_s of 778 F g^{-1} at 5 mV s^{-1} scan rate. Two distinct direct band gaps (with values of 1.33 and 2.25 eV) were observed for Co_3O_4 nanoparticles synthesized at 140 °C. These gaps are attributed to the $O_2^- \rightarrow Co^{2+}$ and $O_2^- \rightarrow Co^{3+}$ charge transfer processes, confirming the formation of a pure Co_3O_4 electrode.[188]

3. Co_3O_4 as a battery material

Hydrothermal synthesis of Co_3O_4

The electrochemical performance of LIBs is mainly determined by the choice of the electrode material. TMOs have been broadly explored and reported to be a more suitable choice as an anode material for Li-ion batteries, due to their high theoretical capacity, good safety, and large-scale availability. The limited theoretical capacity of graphite (372 mA h g^{-1}) prevents its use as an anode in LIBs, while many TMOs have attracted attention as promising anodes for next-generation LIBs due to their good theoretical capacity, such as Co_3O_4 (890 mA h g^{-1}), CoO (715 mA h g^{-1}), and NiO (718 mA h g^{-1}). But among all these, Co_3O_4 with high theoretical capacity (almost 2.3 times higher than that of graphite) aroused considerable interest as a promising alternative candidate for LIBs.[190]

The anodic properties of Co_3O_4 were first reported in 2000 by Poizot *et al*. Since then, research on its energy storage properties has been accelerated.[191] Although cobalt oxide has gained considerable attention in the past few years with its excellent cycle reversibility and high specific capacity, its practical use for real-world LIB applications is restricted due to the rapid degradation of capacity on cycling and large initial irreversible loss. Preserving the integrity of the electrodes after several charge–discharge cycles is one of the objectives to be achieved in developing highly efficient batteries. The interaction between the electrode and ions mainly depends on the evolution of the nanostructures. Recently, studies have shown that synthesized nanostructured materials, non-aqueous electrolytes, and catalysts are very effective strategies to overcome this deficiency.[113,192] The nanostructure architecture achieves a higher surface-to-volume ratio and path lengths. Further, these nanostructures' area and their accompanying large surface-to-volume ratios help to enhance the insertion kinetics and the device's overall efficiency.[115]

Comprehending the nanoscale topography of the electrode and its consequences on the material's physicochemical properties is most significant for designing nanoscale active materials. Co_3O_4 microspheres with high BET_{SSA} (93.4 m^2 g^{-1}) and larger pore volume (78.4 cm^3 g^{-1}) were grown by Liu *et al*. using hexamethylenetetramine as the precipitator and trisodium citrate as a template. Trisodium citrate (as a structure-directing agent) has shown numerous good results; it has a great influence on morphology and leads to the development of fine superstructures, with nanodendritic hierarchical structures being one of them.[193] The as-synthesized electrode showed good stability by retaining 550.2 mA h g^{-1} storage capacity after 25 cycles at a current density of 50 mA g^{-1}. The solid electrolyte interface (SEI) layer that originates during the discharging process due to the dissolution of both organic solvents and ions on the electrode surface is primarily responsible for the large initial irreversible capacity (about 4259 mA h g^{-1}) and its loss after several cycles.[194,195] The hollow structure can also affect the cycling performance, as this structure lowers the electrode pulverization by decreasing the volume changes during the lithium insertion and extraction process. Various morphologies such as hollow

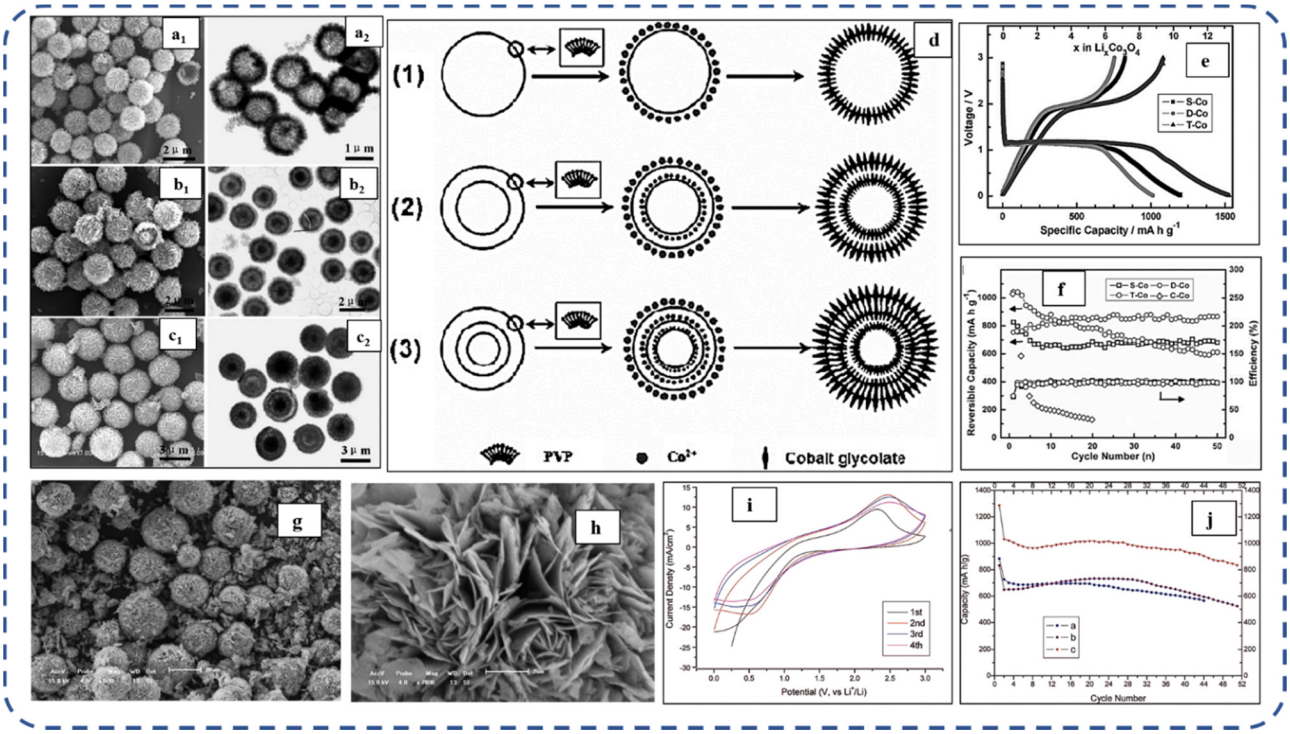

Fig. 22 SEM (a_1), (b_1) and (c_1) and TEM (a_2), (b_2) and (c_2) images of the three samples: (a_1) and (a_2) S-Co, (b_1) and (b_2) D-Co, and (c_1) and (c_2) T-Co. (d) Schematic illustration of the fabrication of multishelled cobalt precursors. (e) Discharge–charge curves of S-Co, D-Co, and T-Co for the first cycle. (f) Discharge capacity retention and coulombic efficiency of the three samples. Reproduced with permission from ref. 196. Copyright 2010, Wiley-VCH Verlag GmbH & Co. KGaA, Weinheim. (g) and (h) Low and high magnification SEM images of pompon-like Co_3O_4 microspheres. (i) CV for the four cycles. (j) Discharge capacity retention for the three synthesized Co_3O_4 electrodes. Reproduced with permission from ref. 13. Copyright 2010 ACS.

quasi-octahedra, hollow octahedra, hollow spheres, and nanoparticles were developed by Wang and coworkers and their investigation revealed that highly stable single-crystalline Co_3O_4 with hollow octahedral cage morphology displayed excellent capacity retention with high discharge capacity (1470.2 mA h g^{-1}).[114]

Currently, multishell structures have attracted much attention in various architectures, but the reported shells are generally aggregated from numerous nanoparticles with irregular arrangements. Among the multishell architectures, the multishell hollow spheres with single-shell (S-Co), double-shell (D-Co), and triple-shell (T-Co) (as shown in Fig. 22(a–c)) developed by Wang *et al.* in the presence of poly(vinylpyrrolidone) (PVP) are very exceptional (schematic illustration of the fabrication of multishell cobalt precursors is depicted in Fig. 22(d)). The multishell formation is attributed to the presence of PVP as a soft template and the formation of cobalt glycolate. High-magnification SEM investigation reveals that all these spherical shells are composed of self-assembled nanosheets. The first discharge capacities of S-Co, D-Co, and T-Co were found to be about 1199.3, 1013.1, and 1528.9 mA h g^{-1}, respectively. Among them, the double-shelled hollow structure offers a good rate capacity as an anode material, by maintaining 866 mA h g^{-1} in 50 cycles, and even at a high scan rate, it delivers a capacity of 500.8 mA h g^{-1} (Fig. 22(e and f)).[196] PVP also plays an important role in the preparation of homogeneous products of smaller size.[132] In another work, the hierarchical porous structures and highly crystalline textures of pompon-like microspheres (Fig. 22(g and h)) were yielded with the assistance of the PVP additive. The CV curve as shown in Fig. 22(i) shows that except for the 1st cycle, all other cycles exhibit the same profile, with the reduction peak located at 2.44 V *vs.* Li^+/Li and the oxidation peak at 0.69 V. The developed electrode exhibited excellent electrochemical characteristics with excellent initial discharge capacity and cycling retention (Fig. 22(j)). The decomposition of the trace $Co(OH)_2$ precipitate may result in CoO impurities due to incomplete oxidation, and after 550 °C the impurity gets transformed into Co_3O_4.[13]

Various research groups have developed remarkable and functional nanostructures using surfactants, such as CTAB, high-quality ordered mesoporous silica SBA-15 (2D), and KIT-6 (3D). For example, finger-like Co_3O_4 nanorods with an initial discharge capacity of 1171 mA h g^{-1} at a current density of 50 mA g^{-1} with good cycle stability (maintained 1006 mA h g^{-1} after 50 cycles) were developed using CTAB as the surfactant[197] Later, they developed hierarchically ordered mesoporous Co_3O_4 materials using mesoporous silica SBA-15 (2D) and KIT-6 (3D) at optimized temperature using a hydrothermal approach. The hierarchical mesoporous Co_3O_4 electrode treated at a lower temperature exhibited superior Li storage performance with a discharge-specific capacity of around 1141 mA h g^{-1} (R_{ct} 20 Ω) compared to the other developed Co_3O_4 samples.[14] Then, nanoporous Co_3O_4 plates with an SBA-15 silica template were studied as anodes for LIBs. The large BET_{SSA} (161.9 m^2 g^{-1}), small crystallite size (approximately 3 nm), and lower thickness

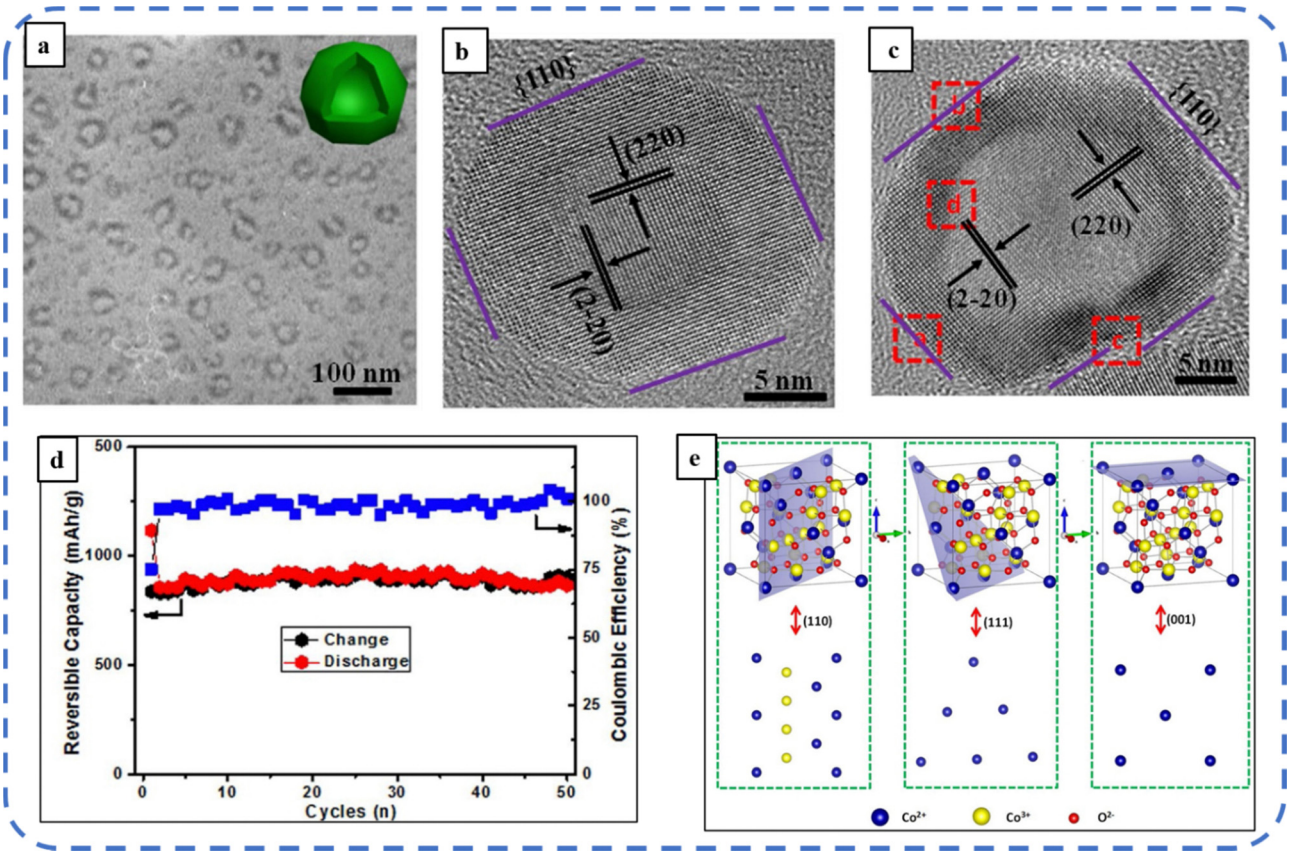

Fig. 23 (a) Low magnification TEM image of Co_3O_4 hollow nanocages (inset: polyhedral nanocage schematic). (b) and (c) HRTEM images of a single Co_3O_4 hollow nanocage. (d) Cycling performance and coulombic efficiency. (e) Theoretical models of 3D and 2D surface atomic configurations of the (110), (111) and (001) planes of Co_3O_4. Reproduced with permission from ref. 202. Copyright 2013 Nature.

(almost 10 nm) offered shorter ion transport/diffusion pathways and provided more surface active sites for the electrode–electrolyte interaction.[198] Then, self-assembled Co_3O_4 microspheres (8 μm diameter) containing nanoplatelets (average thickness 30–70 nm) were developed using CTAB, which formed after a reaction time of about 48 h. CTAB, serving as a cationic surfactant, facilitates the formation of micelles that play a pivotal role in governing the growth mechanism of 2D self-assembled nanosheets. This process leads to the generation of Co_3O_4 nanoplatelets, exhibiting a notable high reversible capacity retention of 620 mA h g^{-1} after 40 cycles.[199]

PVP and sodium acetate as the surfactant and precipitator, respectively, facilitate the growth of mesocrystalline hexagonal Co_3O_4 nanosheets with highly exposed (111) crystallographic planes. The synthesized electrode exhibited excellent electrochemical performance as an anode material for LIBs (1000 mA h g^{-1} at 0.1C) and sodium-ion batteries (600 mA h g^{-1} at 0.1C).[200] Further, diallyldimethylammonium chloride (DDA) and urea as the structure-directing reagent and precipitating reagent, respectively, played an important role in the synthesis of the hierarchical straw-sheaf-like Co_3O_4 structure made up of nanoneedles (length 10 μm and avg. diameter about 80 nm). Later, Wang *et al.* analyzed the surface charge properties of crystal nuclei with and without DDA addition using zeta potential measurement. The optimized amount of DDA exhibited a reversible specific capacity of 903.7 mA h g^{-1} and retained 92% after 300 cycles.[201] Afterward, Co_3O_4 nanocages, with a first discharge capacity of about 1116 mA h g^{-1} (> the theoretical 890 mA h g^{-1}), were fabricated by Liu and co-workers. Fig. 23(a) depicts the TEM image of Co_3O_4 hollow nanocages with an almost uniform size of about 25 nm. Densely packed ethylene glycol molecules on the (100) surfaces (as complexing agents) and O^{2+} containing bubble templates (released from the H_2O_2 reaction) play a crucial role in the nanocage formation process. The authors further studied the relationship between crystal plane structures of Co_3O_4 and their electrochemical performance and stated that highly reactive (110) planes with nanocages have high surface energy and deliver a reversible lithium storage capacity of 864 mA h g^{-1} after 50 cycles (Fig. 23(d)). Here, highly exposed (110) planes, comprising a high concentration of surface atoms, and the large void interiors (Fig. 23(e)) resulted in the good cycle performance and improved rate capability of Co_3O_4 nanocages as anode materials in LIB applications.[202]

Subsequently, the facet-dependent electrocatalytic performance of Co_3O_4 for rechargeable Li–O_2 batteries was investigated by Gao *et al.* They successfully synthesized Co_3O_4 cubes (with exposed (001) planes) and octahedra (with exposed (111) planes) by varying the concentration of the cobalt nitrate hexahydrate precursor and sodium hydroxide. The first discharge-specific capacity of the cathode catalyzed by Co_3O_4 octahedra (2463 mA h g^{-1}) at 100 mA g^{-1} current density is

much higher than that of Co_3O_4 cubes (1787 mA h g^{-1}). The higher specific capacity and cycling performance of Co_3O_4 octahedra (grown with a higher concentration of precursors) are attributed to the richer Co^{2+} and more active sites on the (111) plane of Co_3O_4 octahedra.[203] 1D-oriented Co_3O_4 crystal nanofibers with (220) facets on a carbon matrix were easily grown by controlling the calcination time and they exhibited superior rate capability (delivered 720 mA h g^{-1} over 150 cycles even at 1 A g^{-1}). The high surface energy of the (220) oriented facet and the carbon matrix synergistically reduced phase transformation and particle pulverization effects, resulting in an unusually sustained increase in capacity over 150 cycles.[204]

Since the rate performance and cycling stability of 1D nanostructures are still unsatisfactory, mesoporous Co_3O_4 nanobelts were prepared without any template or structure-directing agent. Huang *et al.* in their study proposed a possible formation mechanism of mixed precursors. After calcination, the Co_3O_4 nanobelts appeared similar to the precursor nanobelts (2–3 μm in length and 100–300 nm in width). The SEM images revealed that these nanobelts include many nanocrystals forming an interconnected mesoporous structure on the surface. The Co_3O_4 nanobelts displayed an initial discharge and charge capacity of about 1412 mA h g^{-1} and 1269 mA h g^{-1} respectively. During the first discharge process, the Li-ion storage is affected by the electrolyte dissolution and formation of the inevitable SEI layer. Although larger SSA is associated with higher irreversible capacity in the first cycle, only a 10.2% loss was observed in this work due to the unique morphology. The growth of architecture is attributed to the release and loss of CO_2, HF, and H_2O during the thermal decomposition of the precursors.[205] Recently wheat-like Co_3O_4 on carbon derived from silk with a nanobelt structure was successfully developed by a one-step hydrothermal technique. The electrode synthesized with a distinctive structure, exhibits noteworthy properties suitable for highly reversible lithium-ion applications.[217]

To effectively avoid structural collapse and potential hazards due to the volume expansion during the charge/discharge process, Zhou *et al.* in their work reported a dandelion-like mesoporous Co_3O_4 electrode containing well-distributed nanoneedles (50 nm in width and 5 μm in length). The interspace among the nanoneedles provides enough area for large-volume expansion during the cycling process. The as-synthesized electrode as the anode material of LIBs exhibited high reversible specific capacities of 1430.0 mA h g^{-1} and 1013.4 mA h g^{-1} for the first and 100th cycles, respectively.[206] Similar mesoporous morphology was developed by Wang *et al.* on Cu foam without any conductive additive or binding agent. The Co_3O_4 @Cu foam displays reversible capacities of 1144, 991, 868, and 626 mA h g^{-1} at 0.5C, 1C, 2C, and 5C, respectively, representing the best rate capabilities.[207] By controlling the pH of the precursor solution, three different morphologies were grown by Jin *et al.* While exploring their effect on morphology and electrochemical performance, the leaf-like morphology (pH = 9 and in the presence of urea) showed superior electrochemical performance compared to other samples. Fast response during diffusion and acceleration of lithium-ions is possible due to the ultrathin structure (1 μm width and 30 nm thickness) of the Co_3O_4-leaf structure.[208]

Later, Reddy *et al.* studied the effect of synthesis temperature on the performance of Co_3O_4 electrodes developed using the urea combustion method which showed the formation of aggregated particulate (10–20 nm) nanostructures. This network encounters structural destruction during successive GCD cycles.[218] Likewise, a similar deterioration in structural integrity was detected by Yu *et al.* during the synthesis of Co_3O_4

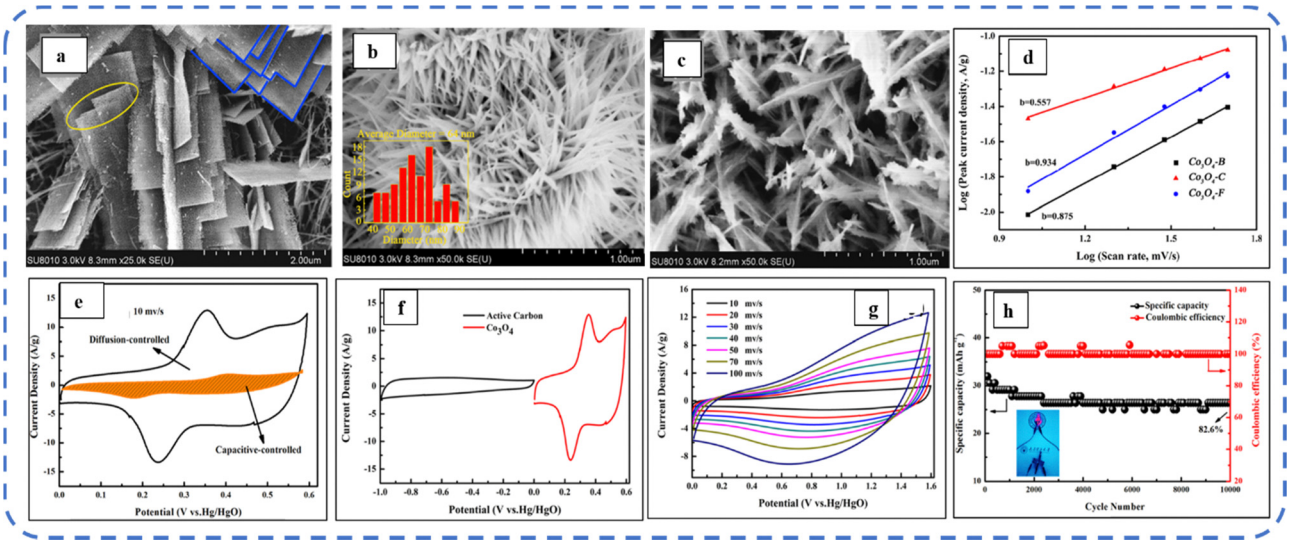

Fig. 24 SEM images of synthesized (a) band-like (Co_3O_4-b), (b) feather-like (Co_3O_4-f) and (c) chrysanthemum-like (Co_3O_4-c) Co_3O_4. (d) Graph of log (peak current density) against log (scan rate) of three electrodes. (e) Capacitive and diffusion-controlled contribution of Co_3O_4-c. (f) CV curves of AC and Co_3O_4-c at 10 mV s^{-1}. (g) CV curves at various scan rates and (h) cycling performance and Coulombic efficiency (the inset image shows the application of the developed device) of the as-synthesized Co_3O_4–C//AC device. Reproduced with permission from ref. 117. Copyright 2021 Elsevier.

nanosheets (10–20 nm thick), composed of numerous interconnected nanoparticles (5 nm in diameter). The as-synthesized electrode yields nearly 593.1 mA h g^{-1} (74.2% of the initial discharge capacity) at the end of 100 cycles.[209]

Over the past few decades, great efforts have been devoted to producing various secondary batteries, such as lead-acid batteries, nickel-cadmium batteries, and lithium-ion batteries, and more recently sodium-ion batteries, aluminum-ion batteries, calcium-ion batteries, *etc*. LIBs are promising as energy storage devices due to their long cycle life, high operating voltage, and energy density, but the desired performance cannot be achieved due to safety issues such as short circuits, explosions during use, and poor charge–discharge performance. Aluminium is widely studied due to its many advantages such as low production cost, long lifetime, and fast charge/discharge response. Liu *et al*. developed nanosphere-rod-like Co_3O_4 for the cathode materials of aluminium ion batteries. It exhibits an initial discharge-specific capacity of 490 mA h g^{-1} at a current density of 50 mA g^{-1}.[210] The change in morphology and its associated reaction mechanism were investigated for the first time during the formation of Co_3O_4 electrodes, by adjusting the urea concentration in the precursor solution. Guo *et al*. found that during the oxidation reaction process, surface-controlled reactions dominate in Co_3O_4 electrodes having band-like (Co_3O_4-b) (Fig. 24(a)) and feather-like (Co_3O_4-f) (Fig. 24(b)) morphologies. Conversely, the chrysanthemum-like Co_3O_4 (Co_3O_4-c) electrode (Fig. 24(c)) is dominated by diffusion-controlled reactions as depicted in Fig. 24(d). The chrysanthemum-like Co_3O_4 composed of nanowires displayed superior electrochemical properties with a specific capacity of 122.3 mA h g^{-1} at 1 A g^{-1} and maintained 100% of the initial value after 3000 cycles. Further, they developed the ASC device using AC as an anode and Co_3O_4-c as a cathode electrode. The CV profile in Fig. 24(f) shows that the potential window of both AC and synthesized Co_3O_4-c is different, and the developed ASC device (Fig. 24(g)) activates in a wide (0–1.6 V) potential window. The ASC displayed a specific energy of 35.3 W h kg^{-1} at 788.8 W Kg^{-1} specific power and good cycle stability with a capacity retention rate of 82.6% after 10 000 cycles (Fig. 24(h)).[177]

The energy storage performance of electrodes can be efficiently enhanced by working on surface/interface engineering and structural defects (such as oxygen vacancies or heteroatoms). Inspired by this notion, Liu *et al*. developed cubic Co_3O_4 crystallites (Fig. 25(a and b) displaying the FESEM and TEM images) with CoO surface layers (~1.1 nm thick) including oxygen vacancies after annealing at 350 °C. The electronic state of the surface elements and the local chemical environment of the samples are depicted with the help of survey XPS spectra in Fig. 25(c and d).

According to the density functional theory calculations, cubic Co_3O_4 crystallites with an optimized CoO–Co_3O_4 interface containing large oxygen vacancies create an unbalanced charge distribution and the existence of oxygen vacancies on the electrode surface improves the intrinsic conductivity of the electrode. So, the synergistic effect of these two is advantageous for ion and electron transport and it assists in the

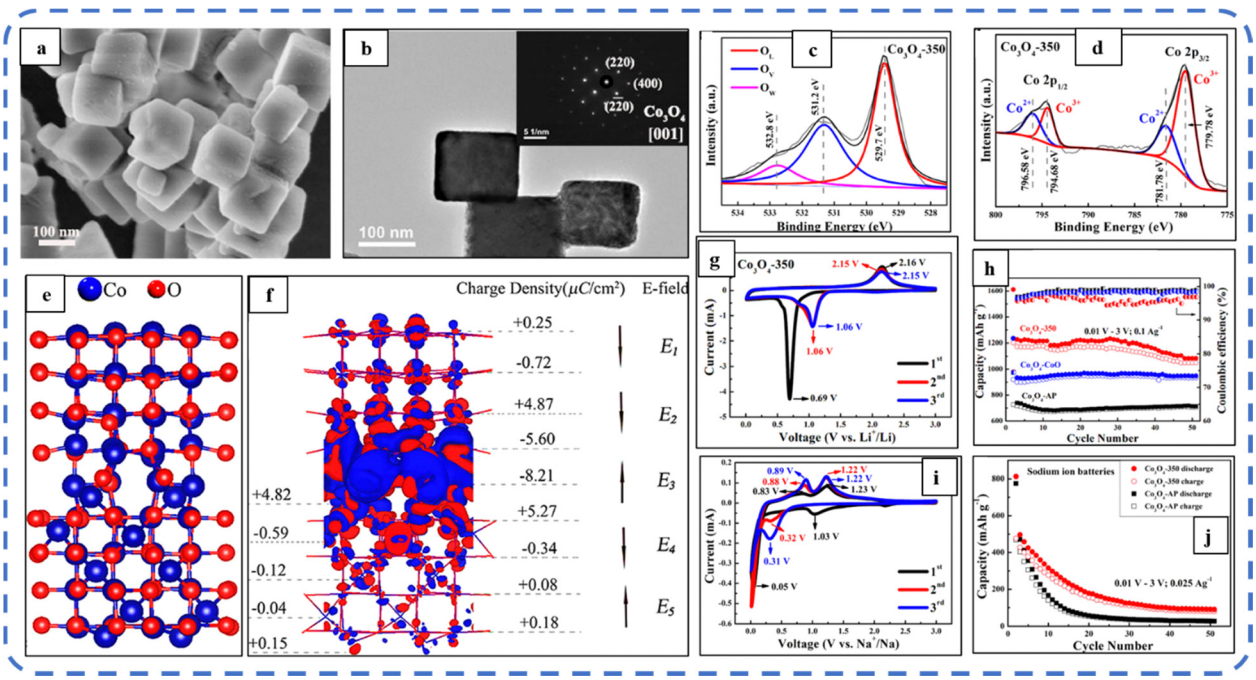

Fig. 25 (a) FESEM and (b) TEM image (the inset shows the SAED pattern); high-resolution XPS spectra of the Co_3O_4-350 sample (d) O 1s region and (c) Co 2p region; slab interfacial model with (e) relaxed structural model for the CoO-(002)–Co_3O_4-(004) interface. (f) Differential charge density of the CoO (002)–Co_3O_4 (004) interfacial system. Blue and red portions indicate negative and positive charge density values, respectively. (g) CV and (h) GCD profiles of lithium storage properties of Co_3O_4-350. (i) CV and (j) GCD profiles of sodium storage properties of Co_3O_4-350. Reproduced with permission from ref. 211. Copyright 2020 ACS publications.

Table 4 Data analysis of battery-like behavior of Co_3O_4 synthesized *via* hydrothermal and solvothermal approaches

Precursor	Reaction temperature	Annealing temp.	Morphology	First discharge capacity (mA h g^{-1}) or current density (mA g^{-1})	Cycle stability or rate capability	BET surface area (m^2 g^{-1}) and pore volume (cm^3 g^{-1})	Electrolyte	Potential window	Ref.
Hydrothermal									
$Co(Ac)_2{\cdot}4H_2O$ + DW + diluted ammonia + polyvinylpyrrolidone (PVP)	180 °C for 48 h	550 °C for 6 h	Pompon-like microspheres	1286.8 mA h g^{-1}			1 M $LiPF_6$ + EC + PC + DEC	0 to 3.0 V	13
$Co(NO_3)_2{\cdot}6H_2O$ + HMT + trisodium citrate + DW	100 °C for 24 h	200 °C for 3 h	Microspheres	About 4259 mA h g^{-1}	550.2 mA h g^{-1} after 25 cycles	93.4 m^2 g^{-1} and 78.4 m^2 g^{-1}	1 M $LiPF_6$ + EC + DEC	0.01 and 3.0 V	195
$Co(CH_3COO)_2{\cdot}4H_2O$ + PVP + ethylene glycol	180–200 °C for 12–24 h	400–600 °C for 1.5–5 h	Nanosheet-assembled multi-shelled hollow spheres	1013.1 mA h g^{-1}	866 mA h g^{-1} after 50 cycles		1 M $LiPF_6$ + EC + DMC + DEC		196
$Co(Ac)_2{\cdot}4H_2O$ + $CO(NH_2)_2$ + CTAB + deionized water	100 °C for 24 h	400 °C for 2 h	Nanorods	1171 mA h g^{-1} @50 mA g^{-1} (265 F g^{-1} @2 mV s^{-1})	1006 mA h g^{-1} after 50 cycles	33 m^2 g^{-1} and 0.11 cm^3 g^{-1}	1 M $LiPF_6$ + EC + DMC and 6 M KOH	0–0.45 V	197
$Co(NO_3)_2{\cdot}6H_2O$ + silica templates	300 °C for 5 h		Hierarchical mesoporous	1489 mA h g^{-1}	1141 after 25 cycles	105 m^2 g^{-1} and 0.23 cm^3 g^{-1}	1 M $LiPF_6$ + EC + DMC	0–3.0 V	14
$Co(NO_3)_2{\cdot}6H_2O$ + PVP + deionized water + ethanol + CH_3COONa	120 °C for 10 h	80 °C for 12 h.	Hexagonal nanosheets	1000 mA h g^{-1} @0.1C		206 m^2 g^{-1}	1 M $LiPF_6$ + EC + DEC and 1 M $NaClO_4$ + EC + DMC	0.0 and 3.0 V	200
$Co(Ac)_2$ + DDA + urea	120 °C for 12 h	450 °C for 2 h	Straw-sheaf-like	1109.4 mA h g^{-1}	100% (300) @500 mA g^{-1}	18.6 m^2 g^{-1} and 0.22 cm^3 g^{-1}	1 M $LiPF_6$ + EC + DEC		201
$Co(NO_3)_2{\cdot}6H_2O$ + NaOH + DW	180 °C for 5 h	500 °C for 3 h	Octahedra	2463 mA h g^{-1} at 100 mA g^{-1}	2100 mA h g^{-1} after 6 cycles		LITFSI and TEGDME		203
$Co(CH_3COO)_2{\cdot}4H_2O$ + $(CH_2OH)_2$ + deionized water + $CO(NH_2)_2$	200 °C for 24 h	500 °C for 2 h	Nanofibers	1442 mA h g^{-1}@100-mA g^{-1}	986 mA h g^{-1} @100 mA g^{-1} after 150 cycles	78.25 m^2 g^{-1} and 0.393 cm^3 g^{-1}	1.0 M $LiPF_6$ + EC + DEC	0.01 and 3.0 V	204
$Co(NO_3)_2{\cdot}6H_2O$ + $CO(NH_2)_2$ + NH_4F	120 °C for 24 h	400 °C for 4 h	Nanobelts	614 mA h g^{-1}@1 A g^{-1}		36.5 m^2 g^{-1}	1 M $LiPF_6$ + EC + DMC	0–3.0 V	205
$Co(NO_3)_2{\cdot}6H_2O$ + $CO(NH_2)_2$ + NH_4F	110 °C for 5 h	400 °C for 2 h	Dandelion-like mesoporous	1430 mA h g^{-1}	1013.4 mA h g^{-1} after 100 cycles	27.6 m^2 g^{-1}	1 M $LiPF_6$ + EC + DMC + DEC	0.01 to 3.0 V	206
$Co(NO_3)_2{\cdot}6H_2O$ + $CO(NH_2)_2$ + NH_4F + deionized water	110 °C for 12 h	300 °C for 2 h	Dandelion-like mesoporous nanostructures	1238 mA h g^{-1}	882 mA h A g^{-1} @2C (100 GCD cycles)	69 m^2 g^{-1}		0.01–3.0 V	207
$Co(Ac)_2{\cdot}4H_2O$ + urea + DW + ammonia	180 °C for 20 h	300 °C for 3 h	Leaf-like	1140 mA h g^{-1}	1245 mA h g^{-1} after 40 cycles@0.1C		1 M $LiPF_6$ + EC + DEC	0.01–3.00 V	208
$Co(NO_3)_2{\cdot}6H_2O$ + $CO(NH_2)_2$ + H_2O	100 °C for 6 h	250 °C for 1.5 h	Nanosheet array	799.2 mA h g^{-1}	593.1 mA h g^{-1} (74.2%) after 100 cycles		1 M $LiPF_6$ + EC + DMC	0–3.0 V	209
$CoCl_2{\cdot}6H_2O$ + $CO(NH_2)_2$ + deionized water	160 °C after 8 h	600 °C for 2 h	Nanosphere-rod-like	490 mA h g^{-1}@50 mA h g^{-1}	122.1 mA h g^{-1} (100 cycles)	5.803 m^2 g^{-1}	$AlCl_3$+ [EMIm]Cl	0.3–2.2 V	210
$Co(NO_3)_2{\cdot}6H_2O$ + NaOH + deionized water	60 °C for 12 h	350 °C for 1 h	Cubic	1611.1 mA h g^{-1}	1049.5 mA h·g^{-1} (50 cycles)		1 M $LiPF_6$ + EC + DMC	0.01–3.0 V	211
$Co(NO_3)_2$ + urea + deionized water + CTAB + SDBS	140 °C for 4 h	300 °C in air for 2 h	Nanowire arrays	582.8C g^{-1}@1 A g^{-1}	93.1% (25 000)			0–0.6 V	212
Solvothermal									

Table 4 (*continued*)

Precursor	Reaction temperature	Annealing temp.	Morphology	First discharge capacity (mA h g^{-1}) or current density (mA g^{-1})	Cycle stability or rate capability	BET surface area (m^2 g^{-1}) and pore volume (cm^3 g^{-1})	Electrolyte	Potential window	Ref.
$Co(NO_3)_2{\cdot}6H_2O$ + PVP + N,N-dimethylformamide (DMF)	190–230 °C for 20–40 h	4–600 °C for 2 h	Porous nanocapsules	1572 mA h g^{-1}@110 mA g^{-1}	Appr.1000 mA h after 20 cycles		1 M $LiPF_6$ + EC + DMC	0–3.0 V	115
$Co(NO_3)_2{\cdot}6H_2O$ + ethanol + CTAB	150 °C for 48 h		Nanoplatelets	1282 mA h g^{-1}	620 mA h g^{-1} after 40 cycles			0.01 V–3.0 V	199
NaOH + (CH 2COOH)$_2$ + ethanol + DW	150 °C for 2 h	280 °C for 1 h	Flower-like porous spheres	1316.7 mA h g^{-1}	600 mA h g^{-1} after 10 cycles	72.5 m^2 g^{-1}	1 M $LiPF_6$ + EC + DMC		213
$Co(NO_3)_2{\cdot}6H_2O$ + $CO(NH_2)_2$ + $(CH_2OH)_2$ + deionized water	90 °C for 12 h	400 °C for 3 h	Hierarchical mesoporous flower-like	1298 mA h g^{-1}		38.1 m^2 g^{-1}	1 M $LiPF_6$ + EC + DMC		214
$CoCl_2{\cdot}6H_2O$ + isopropyl alcohol (IPA) + Na_2CO_3 + DW	80 °C for 5 h	300 °C for 2 h	Microdisks	1032 mA h g^{-1}	749 mA h g^{-1} at 100 mA g^{-1} after 30 cycles	108.9 m^2 g^{-1}	1 M $LiPF_6$ + EC + DMC + DEC	0.01–3.00 V	215
Cobaltous chloride hexahydrate + NH_4F + ethanol + DI water + 1,2-ethanediol	140 °C for 12 h	400 °C for 2 h	Hexagonal plates	1895 mA h g^{-1}	500 mA h g^{-1} at 1A g^{-1} after 500 cycles		1 M $LiPF_6$ + EC + DMC + DEC	0.001 to 3 V	216

enhancement of the lithium and sodium storage properties of the developed electrode. To understand the mechanisms underlying the lithium storage properties of the surface and defect-tuned Co_3O_4 nanocubes, they constructed a slab interfacial model, comprising five layers of Co_3O_4-(004) planes covered by five layers of CoO-(002) planes (Fig. 25(e)). The interfacial region (negatively charged) and adjacent atomic layers (positively charged) result in the formation of electric fields on the interface; such powerful and opposite electric fields E_2 and E_3 strongly affect ion transportation (Fig. 25(f)) and enhance the electrochemical performance. The result showed that the as-synthesized Co_3O_4 nanocubes exhibited initial discharge capacities of 1611.1 mA h g^{-1} and 812.9 mA h g^{-1} for lithium and sodium storage, respectively. The as-synthesized electrode exhibited greatly improved lithium (CV and GCD profiles are shown in Fig. 25(g and h)) and sodium storage properties (Fig. 25(i and j)).[211] The statistical data of the battery-like behavior of Co_3O_4 synthesized *via* hydrothermal and solvothermal approaches are provided in Table 4.

Solvothermal synthesis of Co_3O_4

The phenomenon of oriented aggregation has attracted attention as a promising method that can control the microstructure along with particle size and provides more insight into defect formation during crystal growth. In 2004, this effect in the surfactant-assisted solvothermal approach was first time observed by He *et al*. They synthesized Co_3O_4 hollow nanospheres as the anode material for use in Li-ion cells. A slight decrease in the peak intensity after 150 cycles was noticed during the CV analysis, indicating the good cycling stability of this electrode. The results showed that solvent and water contents adversely affect the phases and morphologies of products.[219] The flower-like porous (pore size 4.6 nm) Co_3O_4 spheres (400–500 nm in size and 30–40 nm thick) comprising nanosheets have resulted from the use of cobalt hydroxide precursors. These unique structural features of the sphere comprising nanosheets and smaller particle size helped to shorten the path length for Li^+ during the electrochemical reaction and resulted in a high initial discharge capacity of 1316.7 mA h g^{-1}.[213]

Later, Liu *et al*. reported a self-template method based on inside-out Ostwald ripening, in which the first generated precursor acts as a template for subsequent hollowing. Ostwald ripening is a spontaneous process, in which energetic factors favour the growth of larger precipitates at the expense of smaller precipitates. The anisotropic non-spherical porous and hollow Co_3O_4 nanocapsules (1 μm in length and 400 nm in diameter) were synthesized by controlling the crystallization time under solvothermal conditions and using poly(vinyl pyrrolidone) (PVP) as the capping reagent. Fig. 26(a) depicts the SEM image of the synthesized monodispersed Co_3O_4 nanocapsules with uniform size. The inner core crystallites have high surface energy, so Ostwald ripening occurs at the core of these colloidal particles, resulting in hollow dumbbell-shaped solid colloids. After a long reaction time, the product was mainly composed of hollow column-shaped $CoCO_3$ colloids, and

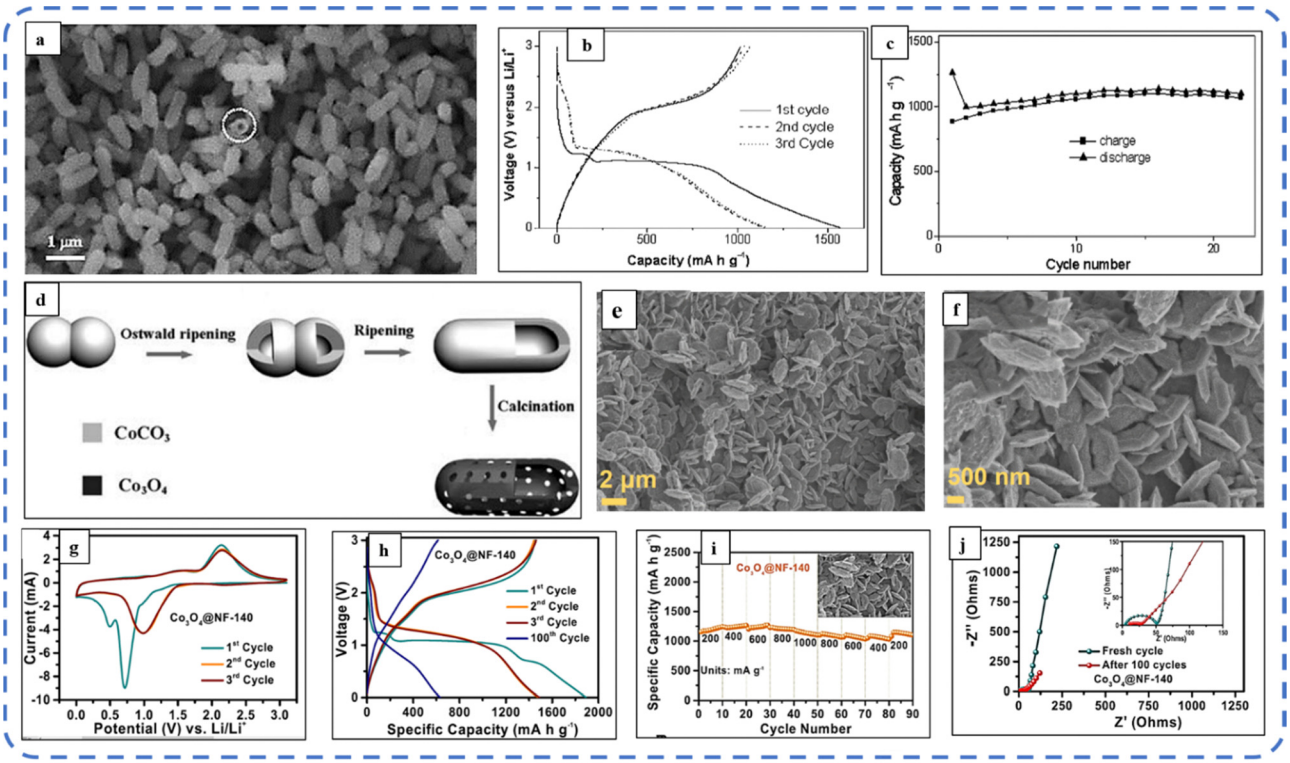

Fig. 26 (a) SEM image and (b) GCD curves at 110 mA g^{-1}. (c) CV curves at 130 mA h g^{-1} of Co_3O_4 porous nanocapsules. (d) Schematic illustration of the evolution process of anisotropic Co_3O_4 porous nanocapsules. Reproduced with permission from ref. 115. Copyright 2010 RSC publications. (e) Low- and (f) high-magnification FESEM images. (g) CV profiles, (h) GCD curves, (i) rate performance plots and (j) EIS plot (before and after cycling) of the as-synthesized Co_3O_4 @NF-140 sample. Reproduced with permission from ref. 216. Copyright 2021 Elsevier.

finally, after 400–600 °C the corresponding anisotropic Co_3O_4 porous nanocapsules were obtained. These porous Co_3O_4 nanocapsules achieved 1572 mA h g^{-1} initial discharge capacity at 130 mA g^{-1} current density and showed excellent Li-ion

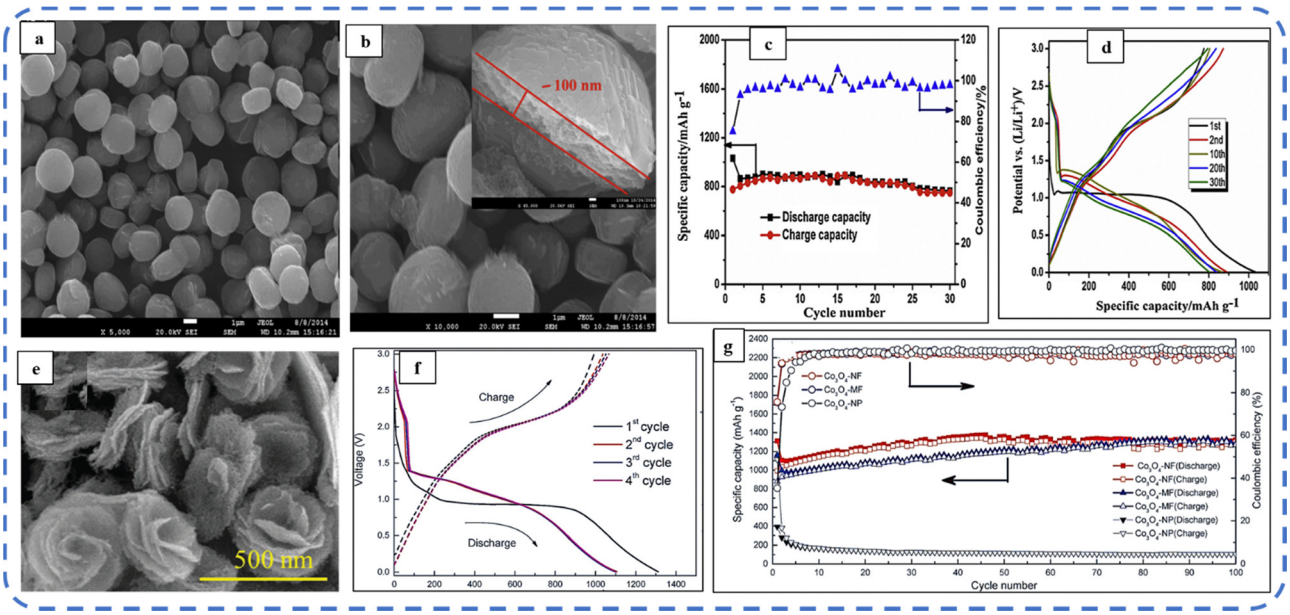

Fig. 27 (a) Low and (b) high magnification FESEM images of the Co_3O_4 mesoporous microdisk sample (the inset shows the cross-section). (c) Capacity retention and (d) GCD curves at different cycles of the as-synthesized Co_3O_4 mesoporous microdisks. Reproduced with permission from ref. 215. Copyright 2015 Elsevier publications. (e) SEM image and (f) charge–discharge profiles of Co_3O_4 nanoflowers. (g) Comparative cycling performance of as-synthesized Co_3O_4-NFs, Co_3O_4-MFs and Co_3O_4-NPs. Reproduced with permission from ref. 190. Copyright 2017 RSC publications.

Table 5 Comparative study of various symmetric and asymmetric devices using the Co_3O_4 electrode

Positive electrode	Negative electrode	Electrolyte	Specific power (kW Kg^{-1})	Specific energy (W h Kg^{-1})	Capacitance/capacity	Capacitance retention	Ref.
Co_3O_4	Co_3O_4	1 M $TEABF_4$.	1240 mW cm^{-3}	4.2 mW h cm^{-3}	4.8 mF cm^{-2} at 3-mA cm^{-2}	80% (10 000)	4
Co_3O_4	Co_3O_4	3 M KOH	1.558	11.26		Almost 82% (2000)	153
Co_3O_4	AC		200	44.99	236.7 F g^{-1} at 1 A g^{-1}		159
Co_3O_4	AC	KOH	1.111	134	108 F g^{-1} at 5-mA cm^{-2}	80% (800)	12
Co_3O_4	AC		1.140	61.60	88 F g^{-1} at 1 A g^{-1}	81.1% (5000)	175
Co_3O_4	N-rGO	6 M KOH	0.8	22.2	62.5 F g^{-1} at 1 A g^{-1}	93.3% (10 000)	171
Co_3O_4	AC	PVA/KOH	7.5	16.25	60 F g^{-1} at 1 A g^{-1}	98.5%. (2000)	173
Co_3O_4	AC	–	0.788	35.3	44.8 mA h g^{-1} at 1 A g^{-1}	82.6% (10 000)	177
Co_3O_4	AC	1 M KOH	1.963	34	108 F g^{-1} at 0.5 A g^{-1}		185
Co_3O_4	AC	6 M KOH	16.71	~31.70	~101 F g^{-1} at 0.5 A g^{-1}	~91.37% (350 000)	187
Co_3O_4	AC	3 M KOH	4.490	55.4	164 F g^{-1} at 0.9 A g^{-1}	90.4% (36 000 cycles)	189
Co_3O_4	AC	6 M KOH	0.224	33.8	162C g^{-1} at 0.2A g^{-1}	74% (10 000)	212

battery performance with good cycle life (maintained 1000 mA h g^{-1} after 20 cycles; refer to Fig. 26(b, c)). The excellent performance is attributed to the evolution process of anisotropic Co_3O_4 porous nanocapsules with Ostwald ripening and the subsequent calcination process, which is schematically illustrated in Fig. 26(d).[115]

More recently, Mule *et al.* successfully developed 3-D hierarchical hexagonal plate-like Co_3O_4 microstructure arrays on nickel foam using NH_4F as a template (Fig. 26(e and f)). The result showed that the porosity of the samples changed significantly by simply changing the growth temperature from 120 °C to 180 °C without affecting the morphology. Among these electrodes, Co_3O_4@NF-140 revealed a higher rate capability (Fig. 26(i)) and better cycling performance, attributed to the strongly linked vertically interconnected highly porous hexagonal plates. The electrochemical reactions involved during the insertion/extraction of lithium in Co_3O_4 can be summarized as follows:

$$Co_3O_4 + 8Li^+ + 8e^- \rightarrow 3Co + 4Li_2O$$

$$Co + Li_2O \rightarrow CoO + 2Li^+ + 2e^-$$

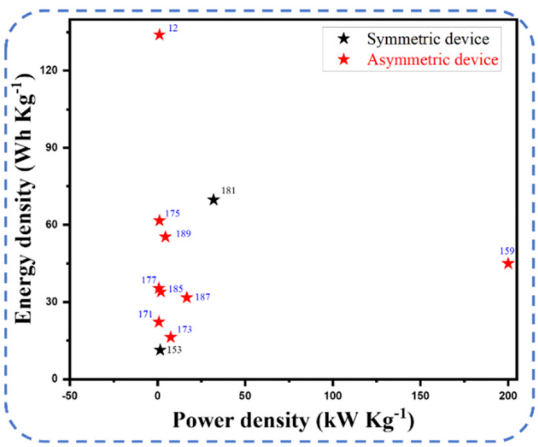

Fig. 28 Ragone plot indicating the performance of symmetric and asymmetric devices developed with Co_3O_4 as an active electrode.

Fig. 26(j) shows that the R_{ct} of the Co_3O_4@NF-140 sample decreases after cycling, leading to faster diffusion of Li ions through the electrode/electrolyte interface and thereby affecting the electrochemical performance. Therefore, the as-synthesized material is an excellent choice as an anode material for LIBs.[216] In contrast, without using any template, surfactant, or catalyst, and using a mixture of isopropyl alcohol (IPA) and water at a relatively low temperature, the synthesis of uniform Co_3O_4 mesoporous microdisks (Fig. 27(a and b)) was first successfully reported by Jin and co-workers. The Co_3O_4 mesoporous microdisk electrode as an anode material exhibited a stable specific charge capacity of 749 mA h g^{-1} after 30 cycles at a current density of 100 mA g^{-1} (Fig. 27(c)). Fig. 27(d) shows the charge–discharge profiles at various cycles and after the first discharge, the earlier flat plateau evolves into a sloping curve due to the heterogeneous reaction mechanism of lithium insertion/extraction. The synthesized electrodes first recorded discharge and charge capacities of about 1032 and 776 mA h g^{-1}, but then a large capacity loss was observed.[215]

Subsequently, an ammonia-assisted solvothermal strategy was employed by Wang *et al.* and it was demonstrated that the flower-like Co_3O_4 structure changes from nanoflowers (Co_3O_4-NFs) (Fig. 27(e) showing the SEM image) to micro-flowers (Co_3O_4-MFs) with increasing ammonia concentration. They used ammonia as a complexing reagent and depending on its concentration, it helps to control nanoscale or microscale dimensions. Co_3O_4-NFs with very high BET_{SSA} (103.9 m^2 g^{-1}) displayed a high reversible specific capacity (1323 mA h g^{-1}), which is much greater than that of Co_3O_4-MFs (1281 mA h g^{-1}).

Fig. 27(f) shows that the profiles remain the same as the cycle increases, but a gradual loss is detected. The cyclic performance shown in Fig. 27(g) reveals the excellent structural integrity of the Co_3O_4-NFs compared to other samples and demonstrates their potential as promising anode materials for LIB applications.[190] Recently, Xiong *et al.* developed Co_3O_4 with a 3D nanoflower structure *via* a two-step solvothermal approach, with many defect sites. These defect-type TMOs assisted in increasing the electrical conductivity and greatly improved the redox kinetics[220] by enhancing the contact between the electrode and the electrolyte.[221] By exhibiting very good electrochemical and electrocatalytic activities, these

defect-type electrodes have shown bi-functional application properties such as energy storage and conversion.[222]

Various symmetric and asymmetric devices were developed based on Co_3O_4 electrodes. The performance of these devices in terms of statistical data is given in Table 5 and the Ragone plot of the devices is highlighted in Fig. 28.

Conclusions and prospective

During the last few years, Co_3O_4 has been a widely explored promising material for various potential applications, including electrochromic devices, solar cells, energy conversion and storage, sensors, photocatalysts, water splitting, anticancer treatments, and numerous other applications. This review summarizes the study of Co_3O_4 active electrodes produced *via* simple hydrothermal and solvothermal methods for their EES applications. The dissimilarity of the solvent used in both of these methods played a very crucial role in enhancing the overall performance. In the hydrothermal/solvothermal synthesis approach, reaction temperature and time, annealing temperature, use of various additives (as precipitant agents, mineralizing agents, hydrolyzing agents, chelating agents, surface-directing agents, and so on), precursors and their concentrations, carefully chosen electrolytes, *etc*. play a very significant role in realizing the competent active Co_3O_4 electrode for EES application. Although great progress has been achieved, the specific capacitance observed for Co_3O_4 is still much lower than its theoretical value, and improving its specific capacitance as well as capacitance retention with rational design and fabrication remains challenging and essential.

Despite high theoretical capacity, Co_3O_4 as an electrode material suffers from low-rate performance and poor cycling stability. Its inherently poor electronic conductivity and severe volume expansion during repetitive lithium-ion exchange eventually lead to electrode failure, which affects its cycling capacity and greatly hinders its practical applications. Researchers have devoted considerable efforts to effectively improve the morphology, porosity, and stability of the Co_3O_4 electrode to enhance its capacity/capacitance, specific power, specific energy, and rate capability. The meticulous optimization of preparation conditions plays a vital role in controlling the morphology of the materials grown at high pressure. One can use a wide variety of substrates to grow materials with vivid morphologies. Substrates like nickel foam, carbon fiber, graphitized CF, *etc.* have been deployed for growing the materials with these techniques [hydrothermal and solvothermal].

Similarly, certain additives affect phase and surface morphology and contribute to desired outcomes by controlling the pH of the solution. Among all these nanostructures, 3D nanostructures are more beneficial over 1D and 2D morphologies in EES applications due to their interesting features such as providing large channels for electrolyte ions by acting as an ion buffering reservoir and offering structural mechanical stability. High specific capacitance with high mass loading signifies the high utilization efficiency and suitability of active electrodes for practical use in real applications. But often overstated specific capacitance is observed at very low mass loadings of the active material (<1 mg). Therefore, it is essential to report on the mass loading or areal capacitance and volumetric capacitance to evaluate the performance of electrode materials.

Improving the specific energy of supercapacitors without affecting their specific power is the most significant challenge, which can be accomplished with the help of subsequent strategies, such as exploring various approaches involving fast surface electrochemical reactions without phase transformation, and also developing networked, hierarchically porous electrodes with low diffusion and ohmic polarization, or an electrode containing a stacked thin energy storage layer and a conductive layer, which can also significantly overcome the diffusion limit and help to utilize the entire porous electrode efficiently. The operating voltages of the active electrode materials appear to be increased after using organic electrolytes instead of aqueous electrolytes. So, using appropriate electrolytes like ionic liquids or the addition of Co^{2+} cations into the electrolyte to stabilize the electrode material helps to achieve a wide potential window, and exploring new hybrid materials combining double-layer capacitance and pseudo-capacitance mechanisms would be very beneficial.

Author contributions

All authors contributed equally to this work.

Conflicts of interest

The authors declare no conflict of interest.

Acknowledgements

One of the authors Dr. D. S. Dalavi is thankful to the DST-SERB, New Delhi, India, for financial support through the Empowerment and Equity Opportunities for Excellence in Science (EMEQ) scheme (EEQ/2021/000984).

Notes and references

1 R. R. Salunkhe, Y. V. Kaneti, J. Kim, J. H. Kim and Y. Yamauchi, *Acc. Chem. Res.*, 2016, **49**, 2796–2806.
2 V. Aravindan, J. Gnanaraj, Y. S. Lee and S. Madhavi, *Chem. Rev.*, 2014, **114**, 11619–11635.
3 F. Shi, L. Li, X. L. Wang, C. D. Gu and J. P. Tu, *RSC Adv.*, 2014, **4**, 41910–41921.
4 N. Padmanathan, S. Selladurai and K. M. Razeeb, *RSC Adv.*, 2015, **5**, 12700–12709.
5 J. Xie, P. Yang, Y. Wang, T. Qi, Y. Lei and C. M. Li, *J. Power Sources*, 2018, **401**, 213–223.
6 T. Brousse, D. Bélanger, K. Chiba, M. Egashira, F. Favier, J. Long, J. R. Miller, M. Morita, K. Naoi, P. Simon and W. Sugimoto, *Springer Handbooks*, 2017, 495–561.

7 Z. Wu, L. Li, J. M. Yan and X. B. Zhang, *Adv. Sci.*, 2017, **4**(6), 1600382.
8 Y. Wang, Y. Song and Y. Xia, *Chem. Soc. Rev.*, 2016, **45**, 5925–5950.
9 A. L. M. Reddy, M. M. Shaijumon, S. R. Gowda and P. M. Ajayan, *Nano Lett.*, 2009, **9**, 1002–1006.
10 S. Gupta and S. B. Carrizosa, *Appl. Phys. Lett.*, 2016, **109**(24), 243903.
11 P. Forouzandeh, V. Kumaravel and S. C. Pillai, *Catalysts*, 2020, **10**, 1–73.
12 Q. Yang, Z. Lu, X. Sun and J. Liu, *Sci. Rep.*, 2013, **3**, 1–7.
13 B. Guo, C. Li and Z. Y. Yuan, *J. Phys. Chem. C*, 2010, **114**, 12805–12817.
14 S. Sun, X. Zhao, M. Yang, L. Wu, Z. Wen and X. Shen, *Sci. Rep.*, 2016, **6**, 1–10.
15 R. N. Singh, J. F. Koenig, G. Poillerat and P. Chartier, *J. Electrochem. Soc.*, 1990, **137**, 1408–1413.
16 V. R. Shinde, S. B. Mahadik, T. P. Gujar and C. D. Lokhande, *Appl. Surf. Sci.*, 2006, **252**, 7487–7492.
17 J. Mei, T. Liao, G. A. Ayoko, J. Bell and Z. Sun, *Prog. Mater. Sci.*, 2019, **103**, 596–677.
18 K. K. Lee, W. S. Chin and C. H. Sow, *J. Mater. Chem. A*, 2014, **2**, 17212–17248.
19 M. Hamdani, *Int. J. Electrochem. Sci.*, 2010, **5**, 556–577.
20 X. Hu, L. Wei, R. Chen, Q. Wu and J. Li, *ChemistrySelect*, 2020, **5**, 5268–5288.
21 X. Wang, A. Hu, C. Meng, C. Wu, S. Yang and X. Hong, *Molecules*, 2020, **25**(2), 269.
22 Y. Jiang and J. Liu, *Energy Environ. Mater.*, 2019, **2**, 30–37.
23 C. Choi, D. S. Ashby, D. M. Butts, R. H. DeBlock, Q. Wei, J. Lau and B. Dunn, *Nat. Rev. Mater.*, 2020, **5**, 5–19.
24 T. S. Mathis, N. Kurra, X. Wang, D. Pinto, P. Simon and Y. Gogotsi, *Adv. Energy Mater.*, 2019, **9**, 1902007.
25 D. S. Dalavi, R. S. Desai and P. S. Patil, *J. Mater. Chem. A*, 2022, **10**, 1179–1226.
26 T. Brousse, D. Bélanger and J. W. Long, *J. Electrochem. Soc.*, 2015, **162**, A5185–A5189.
27 P. M. S. Monk, S. L. Chester, D. S. Higham and R. D. Partridge, *Electrochim. Acta*, 1994, **39**, 2277–2284.
28 H. N. Ok and J. G. Mullen, *Phys. Rev.*, 1968, **168**, 550–562.
29 H. Kelmus, *Ind. Eng. Chem.*, 1914, **6**(2), 115.
30 C. Rajeevgandhi, K. Sathiyamurthy, L. Guganathan, S. Savithiri, S. Bharanidharan and K. Mohan, *J. Mater. Sci. Mater. Electron.*, 2020, **31**, 16769–16779.
31 M. Mandal and D. Chakraborty, *J. Polym. Res.*, 2021, **28**, 1–9.
32 M. Vyas, K. Pareek, R. Rohan and P. Kumar, *Ionics*, 2019, **25**, 5991–6005.
33 W. L. Smith and A. D. Hobson, *Acta Crystallogr. Sect. B Struct. Crystallogr. Cryst. Chem.*, 1973, **29**, 362–363.
34 T. Ocana and M. Guillen, *J. Cryst. Growth*, 1976, **34**, 103–108.
35 Y. Xie, F. Dong, S. Heinbuch, J. J. Rocca and E. R. Bernstein, *Phys. Chem. Chem. Phys.*, 2010, **12**, 947–959.
36 J. Chen, X. Wu and A. Selloni, *Phys. Rev. B - Condens. Matter Mater. Phys*, 2011, **83**, 1–24.
37 W. L. Roth, *J. Phys. Chem. Solids*, 1964, **25**, 1–10.
38 M. S. Wu, B. Xu and C. Y. Ouyang, *J. Mater. Sci.*, 2016, **51**, 4691–4696.
39 T. Takada and Y. Bando, *et al.*, *J. Appl. Phys.*, 1969, **8**, 619.
40 V. S. Zhandun and A. Nemtsev, *J. Magn. Magn. Mater.*, 2020, **499**, 166306.
41 H. Xia, D. Zhu, Z. Luo, Y. Yu, X. Shi, G. Yuan and J. Xie, *Sci. Rep.*, 2013, **3**, 1–8.
42 K. M. Shaju, F. Jiao, A. Débart and P. G. Bruce, *Phys. Chem. Chem. Phys.*, 2007, **9**, 1837–1842.
43 X. Meng, Y. Mi, D. Jia, N. Guo, Y. An and Y. Miao, *J. Mol. Liq.*, 2019, **285**, 416–423.
44 Z. Liu, R. Ma, M. Osada, K. Takada and T. Sasaki, *J. Am. Chem. Soc.*, 2005, **127**, 13869–13874.
45 Z. Huang, Y. Zhao, Y. Song, Y. Li, G. Wu, H. Tang and J. Zhao, *RSC Adv.*, 2016, **6**, 80059–80064.
46 Y. Jiang, Y. Wu, B. Xie, Y. Xie and Y. Qian, *Mater. Chem. Phys.*, 2002, **74**, 234–237.
47 Y. Wang, H. Wang and X. Wang, *Electrochim. Acta*, 2013, **92**, 298–303.
48 S. G. Kandalkar, J. L. Gunjakar and C. D. Lokhande, *Appl. Surf. Sci.*, 2008, **254**, 5540–5544.
49 H. Zhang, Y. Zhou, Y. Ma, J. Yao, X. Li, Y. Sun, Z. Xiong and D. Li, *J. Alloys Compd.*, 2018, **740**, 174–179.
50 T. Maruyama and T. Kanagawa, *J. Electrochem. Soc.*, 1996, **143**, 1675–1677.
51 G. Demazeau, *Rev. High Pressure Sci. Technol.*, 1998, **7**, 1034–1036.
52 S. Somiya, R. Roy and S. Komarneni, *Chemical Processing of Ceramics*, 2nd edn, 2005, vol. 23, pp. 3–20.
53 A. Rabenau, *Adv. Ceram. 3*, 1990, 163–179.
54 S. H. Feng and G. H. Li, *Hydrothermal and Solvothermal Syntheses*, 2017.
55 J. Wu, J. Li and Q. Wu, *Synthesis of Nanoparticles via Solvothermal and Hydrothermal Methods*, 2015.
56 R. C. M. Mambote, M. A. Reuter, P. Krijgsman and R. D. Schuiling, *Miner. Eng.*, 2000, **13**, 803–822.
57 R. Roy and O. F. Tuttle, *Phys. Chem. Earth*, 1956, **1**, 138–180.
58 T. Sugimoto and E. Matijevic, *J. Inorg. Nucl. Chem.*, 1979, **41**, 165–172.
59 R. P. Šimpraga, *J. Electroanal. Chem.*, 1993, **355**, 79–96.
60 M. A. Wheeler and M. Bettman, *J. Catal.*, 1975, **40**, 124–128.
61 T. Maruyama and S. Arai, *J. Electrochem. Soc.*, 1996, **143**, 1383–1386.
62 M. Ando and M. Group, *J. Mater. Chem*, 1997, 1779–1783.
63 P. Nkeng, J. F. Koenig, J. L. Gautier, P. Chartier and G. Poillerat, *J. Electroanal. Chem.*, 1996, **402**, 81–89.
64 Y. Ueda, N. Kikuchi, S. Ikeda and T. Houga, *J. Magn. Magn. Mater.*, 1999, **198**, 740–742.
65 A. J. Esswein, M. J. Mcmurdo, P. N. Ross, A. T. Bell and T. D. Tilley, *J. Phys. Chem. C*, 2009, **113**, 15068–15072.
66 A. Mehboob, S. R. Gilani, A. Anwar, A. Sadiqa, S. Akbar and J. Patujo, *J. Appl. Electrochem.*, 2021, **51**, 691–702.
67 D. K. Pathak, C. Rani, T. Ghosh, S. Kandpal, M. Tanwar and R. Kumar, *ACS Appl. Energy Mater.*, 2022, **5**, 12907–12915.

68 Z. Meng, B. Liu, J. Zheng, Q. Sheng and H. Zhang, *Microchim. Acta*, 2011, **175**, 251–257.
69 T. Zhe, M. Li, F. Li, R. Li, F. Bai, T. Bu, P. Jia and L. Wang, *Food Chem.*, 2022, **367**, 130666.
70 Z. M. Dong, T. Sun, P. Zhang, M. Q. Xu and G. C. Zhao, *Int. J. Electrochem. Sci.*, 2021, **16**, 1–12.
71 D. You, J. Lou, X. Li, Y. Zhou, X. Sun and X. Wang, *J. Power Sources*, 2021, **494**, 229775.
72 P. Aroonratsameruang, P. Chakthranont and P. Pattanasattayavong, *Mater. Chem. Phys.*, 2021, **270**, 124834.
73 C. Yuan, M. Li, M. Wang, Y. Dan, T. Lin, H. Cao, M. Zhang, P. Zhao and H. Yang, *Electrochim. Acta*, 2021, **370**, 137771.
74 A. Salimi, R. Hallaj, S. Soltanian and H. Mamkhezri, *Anal. Chim. Acta*, 2007, **594**, 24–31.
75 W. Feng, V. S. Avvaru, S. J. Hinder and V. Etacheri, *J. Energy Chem.*, 2022, **69**, 338–346.
76 S. Iravani and R. S. Varma, *Green Chem.*, 2020, **22**, 2643–2661.
77 J. S. Ajarem, S. N. Maodaa, A. A. Allam, M. M. Taher and M. Khalaf, *J. Clust. Sci.*, 2022, **33**, 717–728.
78 N. Sultana, S. D. Shawon, S. M. Abu Nayem, M. M. Hasan, T. Islam, S. S. Shah, M. M. Rabbani, M. A. Aziz and A. J. S. Ahammad, *Processes*, 2022, **10**, 390.
79 G. P. Kuppuswamy, K. Pushparaj, V. J. Surya, E. K. Varadharaj, S. Senthil Kumar, C. Di Natale and Y. Sivalingam, *J. Mater. Chem. C*, 2022, **10**, 5345–5355.
80 B. Kupfer, K. Majhi, D. A. Keller, Y. Bouhadana, S. Rühle, H. N. Barad, A. Y. Anderson and A. Zaban, *Adv. Energy Mater.*, 2015, **5**, 1401007.
81 S. Sagadevan, A. R. Marlinda, M. R. Johan, A. Umar, H. Fouad, O. Y. Alothman, U. Khaled, M. S. Akhtar and M. M. Shahid, *J. Colloid Interface Sci.*, 2019, **558**, 68–77.
82 L. Ma, S. Chen, Z. Pei, H. Li, Z. Wang, Z. Liu, Z. Tang, J. A. Zapien and C. Zhi, *ACS Nano*, 2018, **12**, 8597–8605.
83 L. Bai, H. Huang, S. Zhang, L. Hao, Z. Zhang, H. Li, L. Sun, L. Guo, H. Huang and Y. Zhang, *Adv. Sci.*, 2020, **7**, 2001939.
84 Y. Zhao, X. Wang, H. Li, B. Qian, Y. Zhang and Y. Wu, *Chem. Eng. J.*, 2022, **431**, 133981.
85 G. Dawut, Y. Lu, Q. Zhao, J. Liang, Z. L. Tao and J. Chen, *Wuli Huaxue Xuebao/Acta Phys. – Chim. Sin.*, 2016, **32**, 1593–1603.
86 N. R. Chodankar, H. D. Pham, A. K. Nanjundan, J. F. S. Fernando, K. Jayaramulu, D. Golberg, Y. K. Han and D. P. Dubal, *Small*, 2020, **16**, 1–35.
87 P. Zhang, Z. Wang, P. Wang, X. Hui, D. Zhao, Z. Zhang and L. Yin, *ACS Appl. Energy Mater.*, 2022, **5**, 3359–3368.
88 S. Li, Y. Wang, J. Sun, Y. Zhang, C. Xu and H. Chen, *J. Alloys Compd.*, 2020, **821**, 153507.
89 D. Yang, M. Xu, X. Liang, J. Wang, W. Fang, C. Zhu and F. Wang, *Electrochim. Acta*, 2022, **406**, 139815.
90 Y. Zhou, Y. Wang, J. Wang, L. Lin, X. Wu and D. He, *Mater. Lett.*, 2018, **216**, 248–251.
91 F. Ali and N. R. Khalid, *Ceram. Int.*, 2020, **46**, 24137–24146.
92 F. Ali, N. R. Khalid, M. B. Tahir, G. Nabi, K. Shahzad, A. M. Ali and M. R. Kabli, *Ceram. Int.*, 2021, **47**, 32210–32217.
93 F. Ali, N. R. Khalid, G. Nabi, A. Ul-Hamid and M. Ikram, *Int. J. Energy Res.*, 2021, **45**, 1999–2010.
94 M. Aadil, G. Nazik, S. Zulfiqar, I. Shakir, M. F. Aly Aboud, P. O. Agboola, S. Haider and M. F. Warsi, *Ceram. Int.*, 2021, **47**, 9225–9233.
95 E. Niknam, H. Naffakh-Moosavy, S. E. Moosavifard and M. G. Afshar, *J. Energy Storage*, 2021, **44**, 103508.
96 H. Zhang, S. Geng, M. Ouyang, M. Mao, F. Xie and D. J. Riley, *Small*, 2022, 18.
97 W. Li, X. Zhao, Q. Bi, Q. Ma, L. Han and K. Tao, *Dalt. Trans.*, 2021, **50**, 11701–11710.
98 J. Choi, T. Ingsel, D. Neupane, S. R. Mishra, A. Kumar and R. K. Gupta, *J. Energy Storage*, 2022, **50**, 104145.
99 I. S. Imaduddin, S. R. Majid, S. B. Aziz, I. Brevik, S. N. F. Yusuf, M. A. Brza, S. R. Saeed and M. F. Z. A. Kadir, *Mater*, 2021, **14**, 573.
100 C. Liu, A. Gao, F. Yi, D. Shu, H. Yi, X. Zhou, J. Hao, C. He and Z. Zhu, *Electrochim. Acta*, 2019, **326**, 134965.
101 H. Liu, X. Gou, Y. Wang, X. Du, C. Quan and T. Qi, *J. Nanomater.*, 2015, **2015**, 874245.
102 D. Guo, M. Zhang, Z. Chen and X. Liu, *Mater. Res. Bull.*, 2017, **96**, 463–470.
103 C. Yi, J. Zou, H. Yang and X. Leng, *New J. Chem.*, 2018, **42**, 7066–7072.
104 W. Hong, J. Wang, Z. Li and S. Yang, *J. Mater. Chem. A*, 2015, **3**, 2535–2540.
105 L. Jiang, Y. Li, D. Luo, Q. Zhang, F. Cai, G. Wan, L. Xiong and Z. Ren, *Energy Technol.*, 2018, **7**(3), 1800606.
106 D. Guo, M. Zhang, Z. Chen and X. X. Liu, *RSC Adv.*, 2018, **8**, 33374–33382.
107 V. Venkatachalam and R. Jayavel, *J. Electron. Mater.*, 2020, **49**, 3174–3181.
108 X. M. Yue, Z. J. Liu, C. C. Xiao, M. Ye, Z. P. Ge, C. Peng, Z. Y. Gu, J. S. Zhu and S. Q. Zhang, *Ionics*, 2021, **27**, 339–349.
109 K. Min, S. Kim, E. Lee, G. Yoo, H. C. Ham, S. E. Shim, D. Lim and S. H. Baeck, *J. Mater. Chem. A*, 2021, **9**, 17344–17352.
110 Y. Wang, J. Zhou, Z. Zhou, H. Lv, B. Gu, K. Wang, Z. Chen, X. Yan, J. Zhang, W. W. Liu and Y. L. Chueh, *Nanoscale*, 2021, **13**, 15431–15444.
111 H. Sun, J. Zhu, D. Baumann, L. Peng, Y. Xu, I. Shakir, Y. Huang and X. Duan, *Nat. Rev. Mater.*, 2019, **4**, 45–60.
112 X. W. Lou, D. Deng, J. Y. Lee and L. A. Archer, *J. Mater. Chem.*, 2008, **18**, 4397–4401.
113 X. W. Lou, D. Deng, J. Y. Lee, J. Feng and L. A. Archer, *Adv. Mater.*, 2008, **20**, 258–262.
114 X. Wang, L. Yu, X. L. Wu, F. Yuan, Y. G. Guo, Y. Ma and J. Yao, *J. Phys. Chem. C*, 2009, **113**, 15553–15558.
115 J. Liu, H. Xia, L. Lu and D. Xue, *J. Mater. Chem.*, 2010, **20**, 1506–1510.
116 H. Chen, S. Lu, F. Gong, H. Liu and F. Li, *Nanomaterials*, 2017, **7**, 3–14.
117 M. J. Deng, F. L. Huang, I. W. Sun, W. T. Tsai and J. K. Chang, *Nanotechnology*, 2009, **20**, 175602.
118 C. Lv, X. Zhang, Y. Liu, T. Zhang, H. Chen, J. Zang, B. Zheng and G. Zhao, *Chem. Soc. Rev.*, 2021, **50**, 3957–3989.

119 G. Wang, X. Shen, J. Horvat, B. Wang, H. Liu, D. Wexler and J. Yao, *J. Phys. Chem. C*, 2009, **113**, 4357–4361.
120 J. Liu, T. Yang, D. W. Wang, G. Q. Lu, D. Zhao and S. Z. Qiao, *Nat. Commun.*, 2013, **4**, 2798.
121 T. Hisatomi, M. Otani, K. Nakajima, K. Teramura, Y. Kako, D. Lu, T. Takata, J. N. Kondo and K. Domen, *Chem. Mater.*, 2010, **22**, 3854–3861.
122 M. Ghidiu, M. R. Lukatskaya, M. Q. Zhao, Y. Gogotsi and M. W. Barsoum, *Nature*, 2015, **516**, 78–81.
123 H. Deng, S. Grunder, K. E. Cordova, C. Valente, H. Furukawa, M. Hmadeh, F. Gándara, A. C. Whalley, Z. Liu, S. Asahina, H. Kazumori, M. O'Keeffe, O. Terasaki, J. F. Stoddart and O. M. Yaghi, *Science*, 2012, **336**, 1018–1023.
124 W. Li, J. Liu and D. Zhao, *Nat. Rev. Mater.*, 2016, **1**, 16023.
125 L. Cui, J. Li and X. G. Zhang, *J. Appl. Electrochem.*, 2009, **39**, 1871–1876.
126 L. Kunhikrishnan and R. Shanmugham, *Mater. Charact.*, 2021, **177**, 111160.
127 T. Lindner and H. Lechert, *Zeolites*, 1996, **16**, 196–206.
128 J. Yang, X. Li, J. Lang, L. Yang, M. Gao, X. Liu, M. Wei, Y. Liu and R. Wang, *J. Alloys Compd.*, 2011, **509**, 10025–10031.
129 Y. Fang, J. Wen, G. Zeng, F. Jia, S. Zhang, Z. Peng and H. Zhang, *Chem. Eng. J.*, 2018, **337**, 532–540.
130 X. Hu, H. Huang, J. Zhang, J. Shi, S. Zhu and N. Su, *RSC Adv.*, 2015, **5**, 99899–99906.
131 B. Wang, T. Zhu, H. Bin Wu, R. Xu, J. S. Chen and X. W. Lou, *Nanoscale*, 2012, **4**, 2145–2149.
132 M. Kang, H. Zhou, P. Wen and N. Zhao, *ACS Appl. Energy Mater.*, 2021, **4**, 1619–1627.
133 Z. Lu, Q. Yang, W. Zhu, Z. Chang, J. Liu, X. Sun, D. G. Evans and X. Duan, *Nano Res.*, 2012, **5**, 369–378.
134 Z. Yu, Z. Cheng, Z. Tai, X. Wang, C. M. Subramaniyam, C. Fang, S. Al-Rubaye, X. Wang and S. Dou, *RSC Adv.*, 2016, **6**, 45783–45790.
135 X. Xia, J. P. Tu, Y. J. Mai, X. L. Wang, C. D. Gu and X. B. Zhao, *J. Mater. Chem.*, 2011, **21**, 9319–9325.
136 C. Yuan, L. Yang, L. Hou, L. Shen, F. Zhang, D. Li and X. Zhang, *J. Mater. Chem.*, 2011, **21**, 18183–18185.
137 M. Yao, Z. Hu, Z. Xu and Y. Liu, *J. Alloys Compd.*, 2015, **644**, 721–728.
138 M. Liao, Y. Liu, Z. Hu and Q. Yu, *J. Alloys Compd.*, 2013, **562**, 106–110.
139 J. Wang and P. Zhao, *Mater. Lett.*, 2021, **282**, 128892.
140 X. H. Xia, J. P. Tu, Y. Q. Zhang, Y. J. Mai, X. L. Wang, C. D. Gu and X. B. Zhao, *RSC Adv.*, 2012, **2**, 1835–1841.
141 P. Howli, S. Das, S. Sarkar, M. Samanta, K. Panigrahi, N. S. Das and K. K. Chattopadhyay, *ACS Omega*, 2017, **2**, 4216–4226.
142 J. Yang, F. Wei, Y. Sui, J. Qi, Y. He, Q. Meng and S. Zhang, *RSC Adv.*, 2016, **6**, 61803–61808.
143 M. Aadil, S. Zulfiqar, M. F. Warsi, P. O. Agboola and I. Shakir, *J. Mater. Res. Technol.*, 2020, **9**, 12697–12706.
144 H. Adhikari, M. Ghimire, C. K. Ranaweera, S. Bhoyate, R. K. Gupta, J. Alam and S. R. Mishra, *J. Alloys Compd.*, 2017, **708**, 628–638.
145 A. Ali, M. Ammar, I. Hameed and M. Ashraf, *J. Electrochem. Soc.*, 2020, **167**, 100509.
146 D. P. Dubal, P. Gomez-Romero, B. R. Sankapal and R. Holze, *Nano Energy*, 2015, **11**, 377–399.
147 S. K. Meher and G. R. Rao, *J. Phys. Chem. C*, 2011, **115**, 15646–15654.
148 K. Qiu, Y. Lu, J. Cheng, H. Yan, X. Hou, D. Zhang, M. Lu, X. Liu and Y. Luo, *Electrochim. Acta*, 2015, **157**, 62–68.
149 K. Qiu, H. Yan, D. Zhang, Y. Lu, J. Cheng, W. Zhao, C. Wang, Y. Zhang, X. Liu, C. Cheng and Y. Luo, *Electrochim. Acta*, 2014, **141**, 248–254.
150 X. Wang, H. Xia, X. Wang, J. Gao, B. Shi and Y. Fang, *J. Alloys Compd.*, 2016, **686**, 969–975.
151 K. Ding, X. Zhang, P. Yang and X. Cheng, *CrystEngComm*, 2016, **18**, 8253–8261.
152 N. K. Yetim, *J. Mol. Struct.*, 2021, **1226**, 129414.
153 A. Umar, S. D. Raut, A. A. Ibrahim, H. Algadi, H. Albargi, M. A. Alsaiari, M. S. Akhtar, M. Qamar and S. Baskoutas, *Electrochim. Acta*, 2021, **389**, 138661.
154 H. Wang, L. Zhang, X. Tan, C. M. B. Holt, B. Zahiri, B. C. Olsen and D. Mitlin, *J. Phys. Chem. C*, 2011, **115**, 17599–17605.
155 E. Lester, G. Aksomaityte, J. Li, S. Gomez, J. Gonzalez-Gonzalez and M. Poliakoff, *Prog. Cryst. Growth Charact. Mater.*, 2012, **58**, 3–13.
156 G. Rajeshkhanna, E. Umeshbabu and G. Ranga Rao, *J. Colloid Interface Sci.*, 2017, **487**, 20–30.
157 G. Rajeshkhanna, E. Umeshbabu and G. R. Rao, *J. Chem. Sci.*, 2017, **129**, 157–166.
158 N. B. Velhal, T. H. Yun, J. Ahn, T. Kim, J. Kim and C. Yim, *Ceram. Int.*, 2023, **49**(3), 4889–4897.
159 H. Chen, C. Xue, Z. Hai, D. Cui, M. Liu, Y. Li and W. Zhang, *J. Alloys Compd.*, 2020, **819**, 152939.
160 T. Ouyang, K. Cheng, S. Kong, K. Ye, Y. Gao, D. Zhang, G. Wang and D. Cao, *RSC Adv.*, 2015, **5**, 36059–36065.
161 R. Samal, B. Dash, C. K. Sarangi, K. Sanjay, T. Subbaiah, G. Senanayake and M. Minakshi, *Nanomaterials*, 2017, 7(11), 356.
162 C. Feng, J. Zhang, Y. Deng, C. Zhong, L. Liu and W. Hu, *Mater. Sci. Eng. B Solid-State Mater. Adv. Technol.*, 2015, **199**, 15–21.
163 C. Feng, J. Zhang, Y. He, C. Zhong, W. Hu, L. Liu and Y. Deng, *ACS Nano*, 2015, **9**, 1730–1739.
164 C. Feng, J. Zhang, Y. Deng, C. Zhong, L. Liu and W. Hu, *RSC Adv.*, 2015, **5**, 42055–42062.
165 K. Zhou, J. Liu, P. Wen, Y. Hu and Z. Gui, *Mater. Res. Bull.*, 2015, **67**, 87–93.
166 J. H. Kwak, Y. W. Lee and J. H. Bang, *Mater. Lett.*, 2013, **110**, 237–240.
167 T. Jiang and S. Yang, *2D Mater.*, 2018, 0–23.
168 Q. Yang, Z. Lu, Z. Chang, W. Zhu, J. Sun, J. Liu, X. Sun and X. Duan, *RSC Adv.*, 2012, **2**, 1663–1668.
169 T. Y. Wei, C. H. Chen, H. C. Chien, S. Y. Lu and C. C. Hu, *Adv. Mater.*, 2010, **22**, 347–351.
170 Y. Yang, K. Huang, R. Liu, L. Wang, W. Zeng and P. Zhang, *Trans. Nonferrous Met. Soc.*, 2007, **17**, 1082–1086.

171 G. Wei, L. Yan, H. Huang, F. Yan, X. Liang, S. Xu, Z. Lan, W. Zhou and J. Guo, *Appl. Surf. Sci.*, 2021, **538**, 147932.
172 M. Chatterjee, S. Sain, A. Roy, S. Das and S. K. Pradhan, *J. Phys. Chem. Solids*, 2021, **148**, 109733.
173 J. Chen, Z. Xu, H. Zhu, R. Liu, X. Song, Q. Song, J. Wu, C. Zhang, L. Ding, J. Dong and H. Cui, *Vacuum*, 2020, **174**, 109219.
174 R. Xie, H. Huang, X. Qi and G. Wei, *J. Energy Storage*, 2021, **35**, 102258.
175 X. Wang, K. Song, R. Yang, J. Li, X. Jing and J. Wang, *Ionics*, 2019, **25**, 3875–3883.
176 G. S. Jang, S. Ameen, M. S. Akhtar and H. S. Shin, *Ceram. Int.*, 2018, **44**, 588–595.
177 W. Guo, X. Lian, Y. Tian, T. Yang and S. Wang, *J. Energy Storage*, 2021, **38**, 102586.
178 W. Yang, Z. Gao, J. Ma, J. Wang, B. Wang and L. Liu, *Electrochim. Acta*, 2013, **112**, 378–385.
179 M. Pal, R. Rakshit, A. K. Singh and K. Mandal, *Energy*, 2016, **103**, 481–486.
180 X. Qing, S. Liu, K. Huang, K. Lv, Y. Yang, Z. Lu, D. Fang and X. Liang, *Electrochim. Acta*, 2011, **56**, 4985–4991.
181 R. B. Rakhi, W. Chen, D. Cha and H. N. Alshareef, *Nano Lett.*, 2012, **12**, 2559–2567.
182 K. Deori, S. K. Ujjain, R. K. Sharma and S. Deka, *ACS Appl. Mater. Interfaces*, 2013, **5**, 10665–10672.
183 L. Bin Kong, X. M. Li, M. C. Liu, X. J. Ma, Y. C. Luo and L. Kang, *Appl. Mech. Mater.*, 2013, **291–294**, 786–790.
184 Y. Cao, F. Yuan, M. Yao, J. H. Bang and J. H. Lee, *CrystEngComm*, 2014, **16**, 826–833.
185 Y. Wang, S. Huang, Y. Lu, S. Cui, W. Chen and L. Mi, *RSC Adv.*, 2017, **7**, 3752–3759.
186 Y. Xu, Q. Ding, L. Li, Z. Xie and G. Jiang, *New J. Chem.*, 2018, **42**, 20069–20073.
187 P. Sivakumar, M. Jana, M. Kota, M. G. Jung, A. Gedanken and H. S. Park, *J. Power Sources*, 2018, **402**, 147–156.
188 A. UmaSudharshini, M. Bououdina, M. Venkateshwarlu, C. Manoharan and P. Dhamodharan, *Surfaces and Interfaces*, 2020, **19**, 100535.
189 X. Pan, F. Ji, Q. Xia, X. Chen, H. Pan, S. N. Khisro, S. Luo, M. Chen and Y. Zhang, *Electrochim. Acta*, 2018, **282**, 905–912.
190 B. Wang, X. Y. Lu, K. Y. Wong and Y. Tang, *Mater. Chem. Front.*, 2017, **1**, 468–476.
191 P. Poizot, S. Laruelle, S. Grugeon, L. Dupont and J. M. Tarascon, *Nature*, 2000, **407**, 496–499.
192 D. Su, S. Dou and G. Wang, *Sci. Rep.*, 2014, **4**, 5767.
193 L. Zhang, X. Zhao, W. Ma, M. Wu, N. Qian and W. Lu, *CrystEngComm*, 2013, **15**, 1389–1396.
194 Y. M. Lee, J. Y. Lee, H.-T. Shim, J. K. Lee and J.-K. Park, *J. Electrochem. Soc.*, 2007, **154**, A515.
195 Y. Liu, C. Mi, L. Su and X. Zhang, *Electrochim. Acta*, 2008, **53**, 2507–2513.
196 X. Wang, X. L. Wu, Y. G. Guo, Y. Zhong, X. Cao, Y. Ma and J. Yao, *Adv. Funct. Mater.*, 2010, **20**, 1680–1686.
197 S. Sun, X. Zhao, M. Yang, L. Ma and X. Shen, *Nanomaterials*, 2015, **5**, 2335–2347.
198 W. Gou, X. Zhou, J. Li and Y. Ma, *Mater. Lett.*, 2016, **180**, 207–211.
199 M. A. Dar, S. H. Nam, H. S. Abdo, A. A. Almajid, D. W. Kim, A. Qurashi and W. B. Kim, *J. Alloys Compd.*, 2017, **695**, 329–336.
200 D. Xin, J. Dai, J. Liu, Q. Wang and W. Li, *Mater. Lett.*, 2017, **209**, 388–391.
201 B. Wang, X. Y. Lu, C. W. Tsang, Y. Wang, W. K. Au, H. Guo and Y. Tang, *Chem. Eng. J.*, 2018, **338**, 278–286.
202 D. Liu, X. Wang, X. Wang, W. Tian, Y. Bando and D. Golberg, *Sci. Rep.*, 2013, **3**, 1–6.
203 R. Gao, J. Zhu, X. Xiao, Z. Hu, J. Liu and X. Liu, *J. Phys. Chem. C*, 2015, **119**, 4516–4523.
204 Y. Tan, Q. Gao, Z. Li, W. Tian, W. Qian, C. Yang and H. Zhang, *Sci. Rep.*, 2016, **6**, 1–8.
205 H. Huang, W. Zhu, X. Tao, Y. Xia, Z. Yu, J. Fang, Y. Gan and W. Zhang, *ACS Appl. Mater. Interfaces*, 2012, **4**, 5974–5980.
206 R. Zhou, Y. Chen, Y. Song and L. Wang, *et al.*, *Appl. Surf. Sci.*, 2017, **414**, 398–404.
207 F. Wang, Z. B. Liu, K. X. Wang, X. D. Zhu, X. H. Fan, J. Gao, Y. J. Feng, K. N. Sun and Y. T. Liu, *Chem. Commun.*, 2018, **54**, 5138–5141.
208 L. Jin, X. Li, H. Ming, H. Wang, Z. Jia, Y. Fu, J. Adkins, Q. Zhou and J. Zheng, *RSC Adv.*, 2014, **4**, 6083–6089.
209 Y. X. Yu, X. Y. Liu, X. H. Xia, Q. Q. Xiong, X. L. Wang, C. D. Gu and J. P. Tu, *Mater. Res. Bull.*, 2014, **51**, 112–118.
210 J. Liu, Z. Li, X. Huo and J. Li, *J. Power Sources*, 2019, **422**, 49–56.
211 Y. Liu, H. Wan, H. Zhang, J. Chen, F. Fang, N. Jiang, W. Zhang, F. Zhou, H. Arandiyan, Y. Wang, G. Liu, Z. Wang, S. Luo, X. Chen and H. Sun, *ACS Appl. Nano Mater.*, 2020, **3**, 3892–3903.
212 C. Guo, M. Yin, C. Wu, J. Li, C. Sun, C. Jia, T. Li, L. Hou and Y. Wei, *Front. Chem.*, 2018, **6**, 1–10.
213 J. Zheng, J. Liu, D. Lv, Q. Kuang, Z. Jiang, Z. Xie, R. Huang and L. Zheng, *J. Solid State Chem.*, 2010, **183**, 600–605.
214 P. Liu, Q. Hao, X. Xia, L. Lu, W. Lei and X. Wang, *J. Phys. Chem. C*, 2015, **119**, 8537–8546.
215 Y. Jin, L. Wang, Y. Shang, J. Gao, J. Li and X. He, *Electrochim. Acta*, 2015, **151**, 109–117.
216 A. R. Mule, D. Narsimulu, A. K. Kakarla and J. S. Yu, *Appl. Surf. Sci.*, 2021, **551**, 148942.
217 R. Lu, Y. Tan, C. Yang, Y. Fan, X. Liang, H. Yuan and Y. Wang, *Colloids Surfaces A Physicochem. Eng. Asp.*, 2022, **652**, 129786.
218 M. V. Reddy, G. Prithvi, K. P. Loh and B. V. R. Chowdari, *ACS Appl. Mater. Interfaces*, 2014, **6**, 680–690.
219 T. He, D. Chen, X. Jiao, Y. Xu and Y. Gu, *Langmuir*, 2004, **20**, 8404–8408.
220 W. Lu, L. Yan, W. Ye, J. Ning, Y. Zhong and Y. Hu, *J. Mater. Chem. A*, 2022, **10**, 15267–15296.
221 Y. Wu, Y. Wang, P. Zhu, X. Ye, R. Liu and W. Cai, *Appl. Surf. Sci.*, 2022, **606**, 154863.
222 S. Xiong, M. Lin, L. Wang, S. Liu, S. Weng, S. Jiang, Y. Xu, Y. Jiao and J. Chen, *Appl. Surf. Sci.*, 2021, **546**, 149064.